INVESTIGATION OF FERROELECTRICITY AND PIEZOELECTRICITY IN FERROELECTRIC THIN FILM CAPACITORS USING SYNCHROTRON X-RAY MICRODIFFRACTION

by

Dal-Hyun Do

A dissertation submitted in partial fulfillment of

the requirements for the degree of

Doctor of Philosophy

(Metallurgical Engineering)

at the

UNIVERSITY OF WISCONSIN-MADISON

2006

ABSTRACT

Ferroelectric materials have a wide range of applications in nonvolatile memory devices, sensors, and actuators due to their properties such as remnant polarization and piezoelectricity. It is necessary to investigate those properties to understand physical phenomena in ferroelectric materials and to have better device performance. Since ferroelectricity and piezoelectricity are directly related to structure at the scale of a single unit cell, we have investigated those properties in $Pb(Zr,Ti)O_3$ (PZT) thin films using synchrotron x-ray microdiffraction, a structural probe.

In order to understand the mechanisms of polarization switching and polarization fatigue, images of polarization domains were made by mapping the intensity of the x-ray reflections of a ferroelectric thin film as a function of position. We found that the degree of polarization switching observed using x-ray measurements agreed with the total switched polarization measured electrically. X-ray microdiffraction experiments also revealed that polarization fatigue in the PZT thin films occurred differently in two regimes depending on the magnitude of the applied electric fields.

Piezoelectricity in PZT thin films was investigated by measuring the changes in the lattice constant under an electric field. Because x-ray diffraction is directly sensitive to the change in lattice constant, it is possible to perform precise measurements of piezoelectric coefficients. We found that the longitudinal piezoelectric coefficient (d_{33}) in $Pb(Zr_{0.45}Ti_{0.55})O_3$ thin film capacitors was 53 pm V^{-1}. However the values of d_{33} measured

using bipolar electric field pulses were different in the two opposite electric field directions. The difference in d_{33} values can be explained using a model based on the coexistence of switchable and nonswitchable polarization domains. This effect leads to a reduction in the piezoelectric coefficient and a broadening of the x-ray reflections of the PZT thin film. The transverse piezoelectric coefficient (d_{31}) was measured to study the clamping effect induced by a substrate. We found that these films did not show the clamping effect and d_{31} was -17 pm V^{-1}.

ACKNOWLEDGEMENTS

I would like to thank all the people who have contributed to this work. I am most grateful to my advisor, Professor Paul G. Evans, for giving me the opportunity to work on an exciting project and for his encouragement and scientific guidance throughout my Ph.D. program. I would like to express my appreciation to Professor Chang-Beom Eom for the PZT thin films used in this work. At the same time, I also thank all other committee members, Professors Donald Stone, Dane Morgan, and Roxann Engelstad, for their invaluable comments and suggestions.

I would like to acknowledge the contribution of people who are working at the Advanced Photon Source. Special thanks to Dr. Eric M. Dufresne and Dr. Zhonghou Cai for their great help during the beam times. I would also like to thank all the lab members, Byoungnam, Soonjoo, Alexei, and Rebecca, for their help over the years. A special thanks goes to Alexei for useful discussions and help in the work.

In particular, I would like to thank my parents and father-in-law for their unconditional love and patience. I am especially grateful to my wife, Kumju, for her patience, her enthusiastic support, and her continuous understanding, and son, Junyoung, who is my source of happiness.

TABLE OF CONTENTS

ABSTRACT ..... **i**

ACKNOWLEDGEMENTS ..... **iii**

TABLE OF CONTENTS ..... **iv**

Chapter 1 Introduction and Background **1**

1.1 Introduction 1

1.2 Background 3
1.2.1 Ferroelectricity 4
1.2.1.1 Ferroelectric domains and domain walls 5
1.2.1.2 Polarization switching and polarization-electric field hysteresis loops 6
1.2.1.3 Perovskite-type ferroelectric oxides and $Pb(Zr,Ti)O_3$ 8
1.2.1.4 Polarization fatigue 10
1.2.2 Piezoelectricity 15
1.2.2.1 Piezoelectric coefficients and electromechanical hysteresis loops 16
1.2.2.2 Measurement of piezoelectric coefficients 18
1.2.2.3 Extrinsic effects on piezoelectric properties 20
1.2.2.4 Piezoelectric response in ferroelectric thin films 21

1.3 Outline of the thesis 21

Chapter 2 Experimental Techniques **23**

2.1 Synchrotron radiation x-ray sources 24
2.1.1 X-ray brilliance 24
2.1.2 Construction of synchrotron radiation source and undulator radiation 25
2.1.2.1 Construction of synchrotron radiation source 25
2.1.2.2 Undulator radiation 26

2.2 Detectors 31
2.2.1 Ionization chambers 31
2.2.2 Scintillation detectors 31
2.2.3 Avalanche photodiode (APD) detectors 32

2.3 Fresnel zone plate x-ray focusing optics 34

2.4 Diffractometer alignment 37

2.5 X-ray diffraction 38

2.6 Electrical measurements 40

Chapter 3 Imaging Polarization Domains **43**
3.1 Introduction 43
3.2 Experimental details 46
3.3 Results and discussion 48
3.3.1 Images of polarization domains 48
3.3.2 Relating x-ray microdiffraction and electrical measurements of polarization switching 55
3.4 Conclusion 58

Chapter 4 Polarization Fatigue in PZT Thin Films **59**
4.1 Introduction 59
4.2 Experimental details 60
4.3 Results and discussion 62
4.3.1 Polarization fatigue in PZT thin films with Pt top electrodes 62
4.3.1.1 Low electric field 62
4.3.1.2 High electric field 69
4.3.2 Polarization fatigue in PZT thin films with SRO top electrodes 74
4.3.3 Discussion 77
4.4 Conclusion 78

Chapter 5 Piezoelectricity in PZT Thin Films **80**
5.1 Introduction 80
5.2 Experimental details 83
5.3 Results and discussion 85
5.3.1 Structure of PZT thin films 85
5.3.2 Precise measurements of the piezoelectric distortion 88
5.3.3 Polarization switching and piezoelectricity 92
5.3.4 Electric field dependence of the piezoelectric response 99
5.3.5 Variation of the piezoelectric response with position 103
5.3.6 Transverse piezoelectric coefficient in clamped PZT thin films 107
5.4 Conclusion 111

Chapter 6 Conclusions **113**

REFERENCES **115**

Chapter 1 Introduction and Background

1.1 Introduction

Perovskite-type oxide materials are important for electronic applications since they exhibit diverse physical properties such as superconductivity, dielectricity, ferroelectricity, piezoelectricity, and magnetism.[1] In particular, ferroelectric oxide thin films such as $BaTiO_3$ and $Pb(Zr,Ti)O_3$ (PZT) have attracted much attention due to their potential applications in nonvolatile memory devices, microsensors and microactuators.[2,3] Among them, the PZT exhibits a large remnant polarization, a low coercive electric field, a high piezoelectric coefficient, and a relatively low growth temperature.

Ferroelectric materials have a noncentrosymmetric unit cell and a spontaneous electrical polarization at room temperature. The direction of the spontaneous polarization can be switched by applying an external electric field. As a result, the central atom of the perovskite structure shifts from its original position. This phenomenon is reversible. The electrical polarization and lack of inversion symmetry in ferroelectric materials also lead to a coupling between mechanical and electrical properties. Applying a stress to a ferroelectric changes the electrical polarization, and applying an electric field deforms the material.

Ferroelectric thin film capacitors often exhibit a suppression of the switchable polarization after a number of switching cycles called polarization fatigue.[4,5] This is one of

several important failure mechanisms in memory device applications of ferroelectric thin films. Fatigue is directly related to the motion of domain walls during polarization switching. Therefore, imaging polarization domains and observing domain wall motion in an electric field can aid in understanding polarization switching and polarization fatigue.

A thin film is free to distort in the direction along its surface-normal under an electric field. However, when a thin film is constrained by a rigid substrate, there is no strain parallel to the surface of the substrate due to the clamping effect induced by the substrate. This effect in turn can limit the distortion along the surface-normal direction. The clamping effect can make piezoelectric coefficients much smaller in thin films than in the bulk.[6] Depending on the mechanical properties of the substrate, the piezoelectric response can also be easily affected by elastic deformation or bending of the substrate. In addition, the movement of domain walls and phase transitions under an applied electric field affect the piezoelectric response. Precise measurements of the piezoelectric response in the ferroelectric films and in the substrate are fundamentally useful in understanding piezoelectricity.

Synchrotron x-ray microdiffraction is a structural probe with submicron spatial resolution that provides a new way to study polarization switching and piezoelectricity in ferroelectric materials. The piezoelectric deformation of the ferroelectric unit cell, for example, shifts x-ray Bragg reflections in reciprocal space and the relative displacement of the noncentrosymmetric atoms affects the diffracted intensity.[7] This structural information is fundamentally useful in understanding piezoelectricity and polarization switching in

ferroelectric materials. The absorption length for hard x-rays in complex oxide ferroelectrics and in oxide electrodes such as $SrRuO_3$ is long compared to the film thicknesses. Ferroelectricity and piezoelectricity can be thus studied through the top electrode on a thin film capacitor. The use of continuous well-defined electrodes allows measurements under homogeneous electric field conditions.

For this work, synchrotron x-ray microdiffraction was used to study polarization switching, polarization fatigue, and piezoelectricity in epitaxial PZT thin film capacitors. Polarization domains can be visualized based on the change in the intensity of the PZT {002} Bragg reflections due to polarization switching. This effect allows us to study polarization switching and polarization fatigue in devices subjected to an external electric field. The measurement of electric-field-induced strain in PZT thin film capacitors provides fundamental piezoelectric quantities including precise values of piezoelectric coefficients, the effect of polarization switching on piezoelectric properties and an estimate of the effects of clamping in ferroelectric thin films.

1.2 Background

In this section, we review the basic concepts of ferroelectricity and piezoelectricity. In addition, we briefly describe polarization fatigue, and the role of clamping effect and other extrinsic effects such as domain wall motion in modifying the piezoelectric response of ferroelectric thin films.

1.2.1 Ferroelectricity

Ferroelectricity is characterized by a spontaneous polarization in the absence of an electric field. The spontaneous polarization can be switched by applying an external electric field. Ferroelectric materials undergo a structural phase transition from a paraelectric phase to a ferroelectric phase upon cooling through the Curie temperature, T_c,. Above T_c, the crystal has a centrosymmetric structure and has no spontaneous polarization. Below T_c, the crystal exhibits ferroelectricity and has a structure resulting from a change in the symmetry of the unit cell. As a perovskite ferroelectric is cooled below T_c, the central ion in the unit cell displaces from its equilibrium position to create a spontaneous polarization. Consequently, a perovskite ferroelectric material transforms from a paraelectric centrosymmetric structure into a ferroelectric noncentrosymmetric structure which is often tetragonal or rhombohedral. Below the phase transition temperature, there are at least two directions along which the spontaneous polarization can exist in a stable state. The spontaneous polarization in $Pb(Zr,Ti)O_3$, for example, lies along <100> directions in the tetragonal phase and <111> directions in the rhombohedral phase. Figure 1.1 shows a schematic diagram of the phase transition and the spontaneous polarization direction in ferroelectric phases.

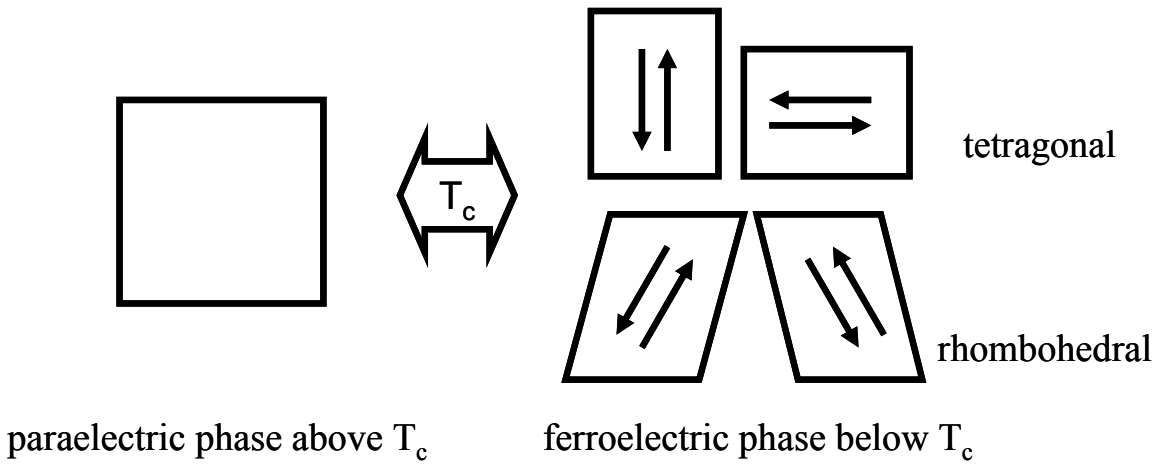

Figure 1.1 Schematic diagram of the phase transition in a ferroelectric material. T_c is the phase transition temperature. The arrow indicates the direction of spontaneous polarization in the ferroelectric phases.

1.2.1.1 Ferroelectric domains and domain walls

A ferroelectric domain is a region within a ferroelectric in which the spontaneous polarization is uniformly oriented. Figure 1.2 (a) shows, for example, the six possible directions of the spontaneous polarization in tetragonal PZT at room temperature. The six directions in the cubic cell are equivalent in the high temperature paraelectric phase, but can be distinguished in the low temperature ferroelectric phase. During the phase transition from the cubic to the tetragonal phase, the spontaneous polarization can arise along any of six directions.

The interface between two domains is called domain wall. In ferroelectric material, the width of domain walls is very small, the scale of a few nm or less.[8] In a tetragonal ferroelectric phase, the angles between two domains are either 90° or 180°, whereas they

are 71°, 109°, or 180° in a rhombohedral phase. The walls separated by oppositely oriented polarization are called *c* or 180° domain walls while *a* or 90° domain walls separate perpendicular domains. The 180° and 90° domain walls are schematically shown in Fig. 1.2 (b). 180° domains can be reversed with minimal structural strains. However, switching of 71°, 90°, 109° domains require a significant structural deformation.

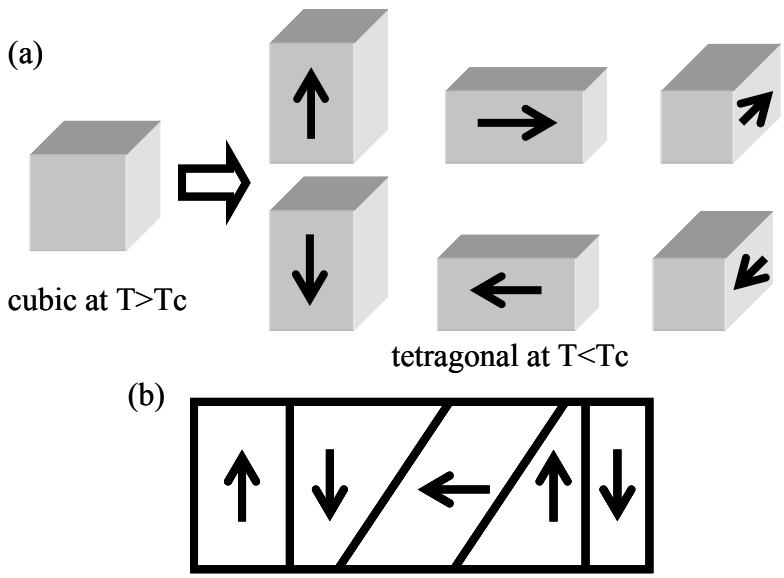

Figure 1.2 (a) Six possible directions of the ferroelectric polarization in tetragonal PZT at room temperature. (b) Schematic diagram of 90° and 180 ° domain walls. The arrows indicate the polarization direction.

1.2.1.2 Polarization switching and polarization-electric field hysteresis loops

When an external field is applied in a direction opposite to the polarization, the polarization can be reoriented in the direction of the electric field.[9] This process is reversible and is called polarization switching. When the polarization is parallel to an

applied electric field, the switching is done. However, it is not necessary that the polarization is exactly reoriented along the electric field direction.

The polarization switching can be observed by measuring the displacement current that flows while the applied electric field is scanned. The charge in the polarization of the ferroelectric as a function of the applied electric field can be calculated by integrating the displacement current. The polarization-electric field hysteresis loop obtained in this way is an important characteristic of a ferroelectric. Figure 1.3 shows a typical hysteresis loop from which the values of the remnant polarization and coercive electric field can be determined.

The net polarization of an initially unpolarized ferroelectric material is small. When an electric field is applied, there is a linear relationship between switchable polarization and the applied electric field. In this case, there is no polarization switching. As the electric field increases, however, domains in which the direction of spontaneous polarization is opposite to electric field begin to switch to a more energetically favorable direction. The switching process continues until all of the domains are aligned in the electric field direction. When the field returns to zero, the polarization does not return back to the initial value. The amount of switchable polarization after removal of an electric field is called the remnant polarization, P_r. The strength of the electric field to switch the opposite polarization domain is called the coercive electric field, E_c. This process can be repeated.

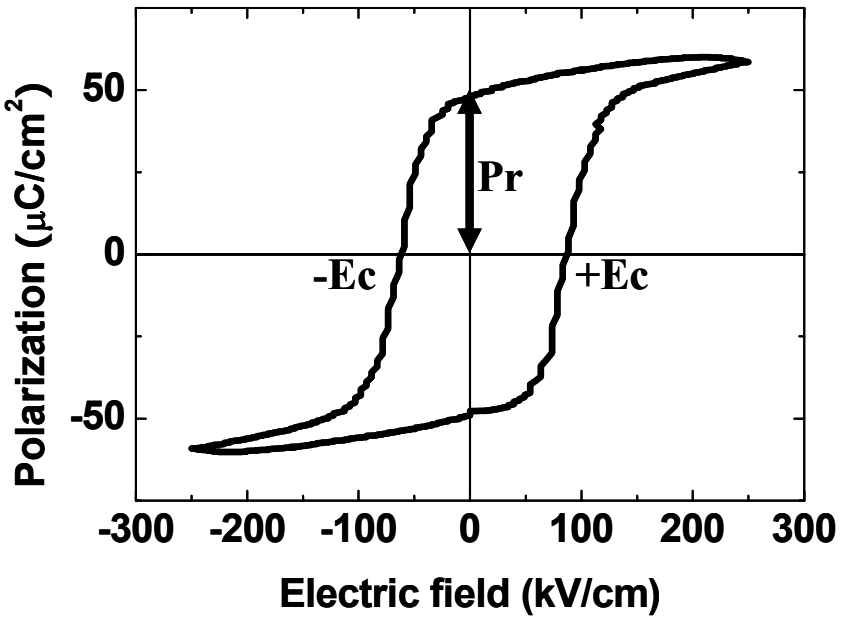

Figure 1.3 Typical polarization-electric field hysteresis loop measured in a ferroelectric material. P_r is the remnant polarization and E_c is the coercive electric field.

1.2.1.3 Perovskite-type ferroelectric oxides and $Pb(Zr,Ti)O_3$

Several ferroelectric materials have structures that are closely related to perovskite, which is the name of the mineral calcium titanate ($CaTiO_3$). The chemical formula of the perovskite family is ABO_3, where the A ions are located at the corners in a unit cell, the B ion is at the cubic center, and the O ions (oxygen ions) are at the face centers, as shown in Fig. 1.4. Several useful ferroelectric oxide materials such as barium titanate ($BaTiO_3$), lead titanate ($PbTiO_3$), lead zirconate titanate ($Pb(Zr,Ti)O_3$) and potassium niobate ($KNbO_3$) have the perovskite-type structure.

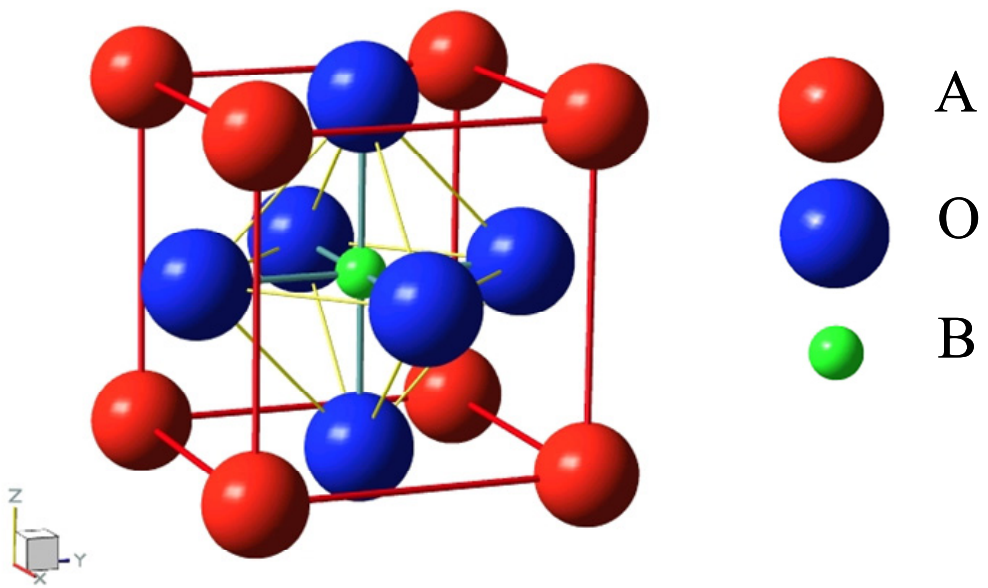

Figure 1.4 Schematic diagram of the ABO_3 perovskite structure.

Pb(Zr,Ti)O$_3$ (PZT)

Lead zirconate titanate is a solid solution of $PbZrO_3$ and $PbTiO_3$. At room temperature, $PbZrO_3$ is in an orthorhombic antiferroelectric phase in which the spontaneous polarization is antiparallel in neighboring unit cells. $PbTiO_3$ at room temperature is in a tetragonal ferroelectric phase in which the spontaneous polarization is parallel in neighboring unit cells. The $Pb(Zr,Ti)O_3$ has the ABO_3 type perovskite structure with Ti^{4+} ions and Zr^{4+} ions occupying B-sites randomly.

The phase diagram of PZT solid solution is shown in Fig. 1.5 (a). The structure of PZT, at high temperature, is a cubic paraelectric phase. Below T_c, PZT has the ferroelectric

or antiferroelectric phase. A tetragonal ferroelectric phase (the Ti rich region of the phase diagram) and a rhombohedral ferroelectric phase (the Zr rich region) are divided by the morphotropic phase boundary (MPB). The composition of Ti:Zr of the MPB is 52:48 at room temperature. Near the composition corresponding to the MPB, there is an abrupt change in lattice constants of PZT as shown in Fig. 1.5 (b). Since the tetragonal and the rhombohedral phases coexist at the MPB,[10] large piezoelectric coefficients, dielectric permittivity, and remnant polarization can be observed in this region.[11] The anomalous properties near the MPB can be explained by a phase transition between the tetragonal and rhombohedral phases.[12,13]

1.2.1.4 Polarization fatigue

Ferroelectric thin films have been extensively studied for applications in electronic devices such as nonvolatile ferroelectric random access memories (FeRAM) because thin films allow low driving voltages and fast read and write speeds.[2] The idea of memories using the switching of spontaneous polarization is simple and this simplicity is one of the motivations for research in ferroelectric materials.[14] Memory devices using ferroelectric materials are based on storing information in the two stable remnant polarization states. For the stable memory operation at low driving voltages, the ferroelectric materials should have a coercive voltage that is much lower than the driving voltage, and a high remnant polarization. High-density FeRAMs are commercially available.[14,15] A key feature in memory devices is that the endurance of large numbers of switching cycles is required. However there are concerns about the long term reliability such as polarization fatigue,

imprint, and retention loss in ferroelectric materials.[14] Imprint is defined as the preference of one polarization state over the other state.[16] Imprint leads to a shift of polarization-electric field hysteresis loop along electric field axis. Retention is the ability of maintaining one polarization state in the absence of an electric field.[17] Retention failure leads to a loss of remnant polarization.

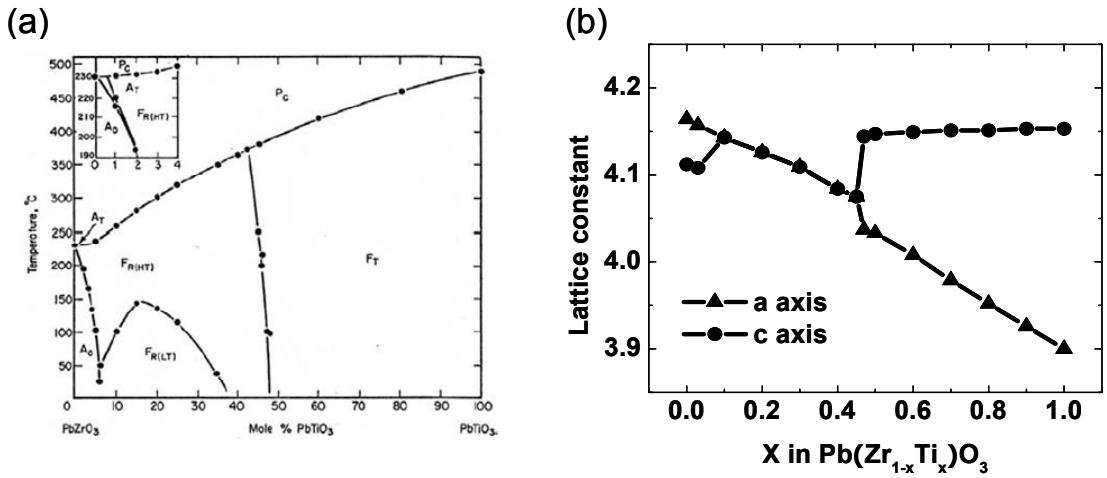

Figure 1.5 (a) Phase diagram[18] and (b) lattice constants of $Pb(Zr,Ti)O_3$ solid solution.[19] The tetragonal and rhombohedral structures are divided by the morphotropic phase boundary.

Polarization fatigue in ferroelectrics is the suppression of switchable polarization as a result of repeated bipolar electrical pulses.[5] Since fatigue creates a decrease in the polarization that can be switched electrically, it is of particular concern for applications such as memory devices. In general, fatigue is related to the number of switching cycles that have been applied to the device. Fatigue occurs between 10^2 and 10^7 switching cycles and modifies the hysteresis loop.[5,20,21] Figure 1.6 (a) shows the reduction of remnant

polarization as a function of the number of switching cycles in a PZT thin film capacitor with a Pt top electrode. There is no fatigue until 10^2 switching cycles. After that, a rapid decrease in remnant polarization occurs. The evolution of hysteresis loop shown in Fig. 1.6 (b) illustrates this effect. The remnant polarization is reduced by 70% of the initial value after 5×10^4 switching cycles.

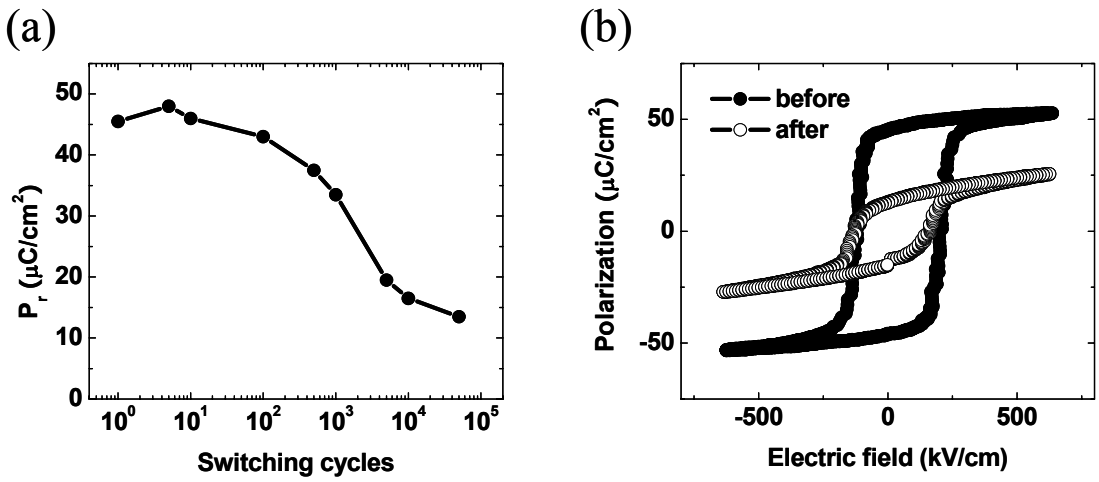

Figure 1.6 Changes in (a) the remnant polarization as a function of the switching cycles and (b) the polarization-electric field hysteresis loops before (10 switching cycles) and after (5×10^4 cycles) fatigue in PZT thin films.

Fatigue occurs in both thin film and bulk ferroelectrics with metal electrodes. It is particularly problematic in PZT capacitors.[5] Although extensive study of polarization fatigue has produced a large body of experimental data and lead to many theoretical models of the fatigue phenomenon,[5, 22] the mechanisms of polarization fatigue are not yet understood well.

Mechanisms of polarization fatigue

Several mechanisms have been proposed for the origin of polarization fatigue. The simplest is a reduction of the effective area of the electrodes of the capacitors.[23] A decrease in the effective size of the capacitor can contribute to a decrease in the total switchable polarization due to delamination of the electrode after a number of switching cycles. If this mechanism is the origin of the fatigue, remnant and switchable polarization, and capacitor area are reduced by the same factor. A second mechanism is a reduction of the effective electric field by the formation of a passive layer.[24] According to this mechanism, a non-switching layer with a low dielectric constant is formed near the interface of the electrodes and the ferroelectric. The effective electric field in the remainder of the ferroelectric is reduced due to the added capacitance in series with the switchable material. Both of these mechanisms, however, are commonly thought to be less important than two others we describe below.

The fatigue mechanisms that are conventionally considered most important are seed inhibition[25] and domain wall pinning.[26,27] The seed inhibition mechanism is shown in Fig. 1.7 (a). The interface between the electrode and the ferroelectric film supports a finite number of sites at which reversed polarization domains can nucleate. The nucleation sites can be defective regions in which the orientation of polarization has a preferred direction due to a built-in bias.[5] When nucleation is inhibited in the some of these defective regions, nonswitchable regions are formed. These regions have the same polarization direction regardless of the electric field and do not switch while other regions still continue to switch.

Thus polarization is completely switched in one direction but not the other when fatigue develops.[28]

In the domain wall pinning mechanism, mobile defects such as oxygen vacancies and electronic charge carriers are trapped at domain walls. The domain walls are pinned and domains surrounded by the pinned domain walls do not continue to switch. Figure 1.7 (b) is an illustration of the domain wall pinning mechanism. Warrant *et al*.[29] proposed this mechanism by observing polarization fatigue in PZT thin films. According to their study, electronic charge carriers generated by optical and thermal treatments were trapped at domain boundaries that have a polarization discontinuity. Accumulation of electronic charge carriers makes difficulty in polarization reorientation under an electric field.

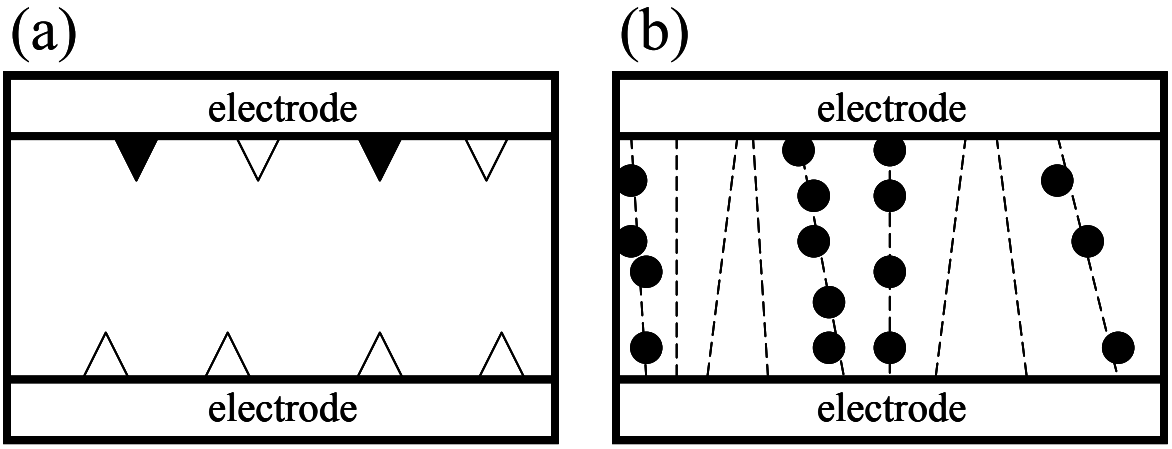

Figure 1.7 Schematic diagrams of fatigue mechanisms. (a) Seed inhibition and (b) domain wall pinning. Black triangles are the nucleation sites that do not contribute to polarization switching in (a) and dashed lines are domain walls and black circles are trapped defects in (b).

<u>The role of defects: oxygen vacancies</u>

The seed inhibition and domain wall pinning mechanisms involve changes in the number and location of defects such as oxygen vacancies. Polarization fatigue is often considered to be the result of either the redistribution of oxygen vacancies[30,31] or the injection of electrons and holes from the electrodes into the ferroelectric thin films.[32,33]. These defects can be trapped at the interface of ferroelectric and electrode or at domain walls.

The most commonly studied defect is oxygen vacancies.[31,34] Auger microprobe data showed that the concentration of oxygen near the electrode region was low in a PZT thin film with Pt electrodes.[30] This result implies a distribution of oxygen vacancies near the ferroelectric and electrode interface. The vacancies then migrate to bulk region under a switching electric field.[35] An improved polarization fatigue performance in PZT thin films can be achieved by using electrodes formed from conducting oxides rather than electrodes formed from metals. Films with conducting oxide electrodes such as RuO_2,[31,36] IrO_2,[37] $SrRuO_3$,[38] and YBCO[39] show no fatigue up to 10^{10} or more cycles. These results suggest a relation between oxygen vacancies and polarization fatigue.

1.2.2 Piezoelectricity

Ferroelectric materials such as $BaTiO_3$ and $Pb(Zr,Ti)O_3$ also exhibit piezoelectricity. Piezoelectrics can be polarized by applying a mechanical stress, and can change dimensions in response to an applied electric field. The piezoelectric effect is a linear coupling

between electrical and mechanical properties. Piezoelectricity is defined in terms of the direct and converse piezoelectric effects. When stress is applied to a piezoelectric material an electric polarization is induced. This is called the direct piezoelectric effect and can be written as $D_i = d_{i\alpha}T_\alpha$ (α=1,2,…,6 and i=1,2,3), where D is the stress-induced polarization (in unit of C cm^{-1}), d is the piezoelectric tensor, and T is the applied stress.[40] The units of the direct piezoelectric coefficient are μC N^{-1}.

In addition, the dimensions of a piezoelectric material change due to the expansion or contraction of lattice when an electric field is applied to the crystal. This is called the converse piezoelectric effect. The strain is $S_\alpha = d_{i\alpha}E_i$, where E is the applied electric field (V cm^{-1}).[40] The units of converse piezoelectric coefficient are pm V^{-1}.

1.2.2.1 Piezoelectric coefficients and electromechanical hysteresis loops

The longitudinal piezoelectric coefficient is the value of the piezoelectric coefficient that applies to the distortion measured in the same direction as the electric field. The value measured in the direction perpendicular to an electric field is called the transverse piezoelectric coefficient. In tetragonal materials, there is a third coefficient, the shear piezoelectric coefficient, which is the shear strain developed when an electric field is applied parallel to the plane of the surface. In ferroelectric thin films, piezoelectric coefficients in directions perpendicular (d_{33}) or normal (d_{31}) to the film surface are measured while an electric field is applied along the film thickness.

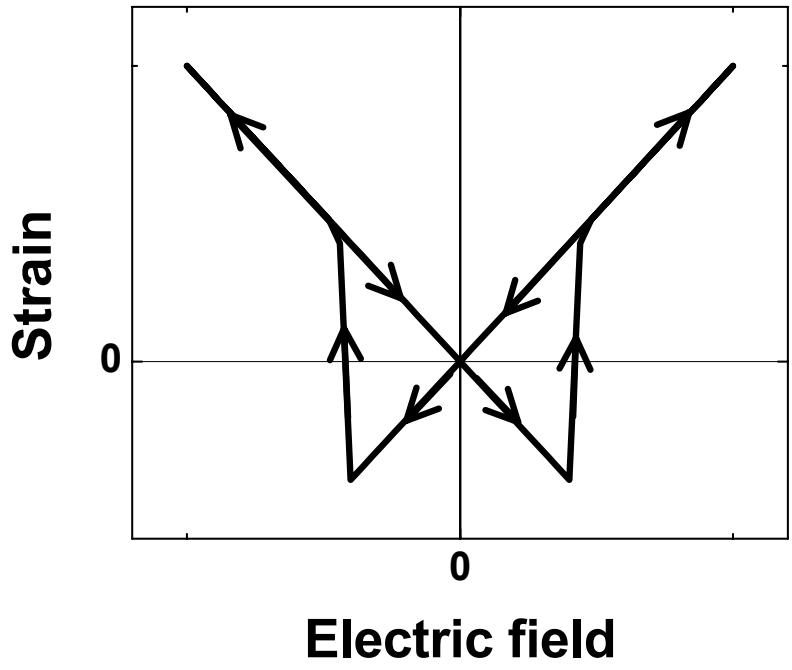

Figure 1.8 A typical electromechanical hysteresis loop. The piezoelectric coefficient is determined from the slope of the straight lines.

According to the converse piezoelectric effect, the strain is linearly proportional to the applied electric field when the piezoelectric coefficient is constant. When the electric field is parallel to the polarization, the strain increases as the electric field increases and the maximum strain occurs at the maximum electric field. However, polarization switching in a ferroelectric subjected to an electric field leads electromechanical hysteresis, as shown in Fig. 1.8. The loop clearly shows piezoelectric response as well as polarization switching under a bipolar electric field. The sign of strain depends on the relative directions of the polarization and the electric field. When the field and polarization are parallel, the lattice

expands and the strain is positive. When the field and polarization directions are antiparallel, the lattice contracts and the strain is negative. An abrupt change in the strain axis occurs due to polarization switching. The electromechanical response is in general reversible. The piezoelectric coefficients can be calculated from the slope of linear regions in the loop.

Information from electromechanical hysteresis loops complements values from polarization-electric field hysteresis loops and can in some case be more quantitative. In the polarization-electric field hysteresis loops, for example, the polarization axis is arbitrarily set because the zero polarization is taken from the average value. Unlike the polarization-electric field hysteresis loop, the electromechanical hysteresis loop shows that the zero strain is an absolute reference point. For this reason, the electromechanical hysteresis loop is used to characterize the ferroelectric properties such as polarization fatigue and imprint effect.[41,42]

1.2.2.2 Measurement of piezoelectric coefficients

Piezoelectric coefficients can be measured using either the direct or converse piezoelectric effects. The piezoelectric coefficients in the direct and converse piezoelectric effects are thermodynamically identical.[43] In order to measure the piezoelectric coefficients using the direct piezoelectric effect, a normal load is applied to a ferroelectric capacitor and the charge on the electrodes is measured. To measure the longitudinal piezoelectric coefficient, the electrical response is parallel to the applied stress. For the transverse

piezoelectric coefficient, a stress is applied in the plane of the material and the induced charge is measured. The direct piezoelectric effect can be measured using methods such as normal load and pneumatic pressure devices.[44] All of these techniques are variations on the basic idea of loading the crystal mechanically and observing the electrical response.

To measure the piezoelectric coefficients using the converse piezoelectric effect, an electric field is applied and the strain in the ferroelectric material is measured. A number of techniques have been used to measure piezoelectric coefficients through the converse piezoelectric effect. The techniques are the interferometer[45,46] and atomic force microscopy (AFM) methods.[47] These techniques measure the piezoelectric coefficients by detecting the displacement of the surface in ferroelectric thin films.

In the AFM technique, a conductive probe tip is used for the top electrode. The tip supplies voltage pulses to the sample. The piezoelectric response can be measured by detecting the bias-induced deformation of the whole sample. However, the value of the surface displacement is not an absolute value and is necessary to calibrate it with a reference material in which the piezoelectric coefficient is known.[48] Although AFM techniques have good spatial resolution, the interaction between the tip and ferroelectric surface is a major problem,[49] and the measurement of a piezoelectric response is static or quasistatic.

X-ray diffraction has been used for determination of the electric field induced structural deformations in ferroelectric materials.[50,51,52] This strain induced by an external

electric field is accompanied by small displacements of the atoms inside the unit cell. In x-ray diffraction experiments, the strain gives rise to a shift of the Bragg peak and a displacement of the atoms within the unit cell affects the diffracted intensity. Thus the piezoelectric coefficients can be measured by recording the location in reciprocal space of the Bragg reflection and their intensity.

1.2.2.3 Extrinsic effects on piezoelectric properties

In terms of the definitions commonly applied to ferroelectric materials, piezoelectric and dielectric properties are affected by both intrinsic and extrinsic contributions.[53] Intrinsic contributions are due to the pure piezoelectric effect within single domains, while extrinsic contributions arise from any other factor that may cause additional strain. Extrinsic effects can be due to 90° domain wall motion,[54] phase transitions,[55] and other sources.

The effect of the movement of 90° domain walls on piezoelectric response has been studied in ferroelectric thin films and ceramics. It was observed that the total piezoelectric response in PZT ceramics was affected by the reorientation of 90° domains.[56] In the case of thin films, the increased piezoelectric coefficients were calculated due to the effect of 90° domain wall motions.[57] Also increased piezoelectric coefficients were experimentally observed in island-shaped PZT thin film capacitors because the clamping effect induced by the substrate was removed.[58] Since these contributions are directly coupled to a change in

the structure of the ferroelectric materials, the investigation of the structural response subjected to an electric field is important to understand piezoelectricity.

1.2.2.4 Piezoelectric response in ferroelectric thin films

The piezoelectric coefficients of thin films are much less than what is expected in bulk. In the thin films, d_{33} is reduced by the substrate-induced clamping effects.[59] The effective piezoelectric coefficient of a thin film constrained by a rigid substrate is $d_{33}^{eff} = d_{33} - \frac{2d_{31}s_{13}^{E}}{s_{11}^{E} + s_{12}^{E}}$, where d_{33} and d_{31} are the longitudinal and transverse piezoelectric coefficients of bulk, s_{ij}^{E} are the elastic compliances of the film at constant electric field.[40] The equation above is valid under the condition that the film is completely constrained by the substrate so that the change in the strain in the plane of the surface caused by the electric field is zero. However the induced stress in the plane may lead to an elastic deformation and a bending of the substrate.[6]

1.3 Outline of the thesis

In this chapter, we have introduced the general concepts of ferroelectricity and piezoelectricity. The proposed mechanisms of polarization fatigue, measurements of piezoelectric coefficients, and the clamping effect on piezoelectric response were briefly described. Chapter 2 presents our experimental techniques including an introduction to synchrotron x-ray sources, Fresnel zone plate x-ray focusing optics, x-ray detectors, x-ray microdiffraction, and the electrical measurement apparatus used in the study.

In Chapter 3, we describe how to visualize polarization domains using x-ray microdiffraction, and electrical and x-ray microdiffraction observations of polarization switching are compared. Chapter 4 discusses polarization fatigue in PZT thin film capacitors based on x-ray images of polarization domain. The origin of polarization fatigue in PZT with a Pt electrode is discussed and compared to that in PZT with an SRO electrode.

Chapter 5 focuses on the local piezoelectric response in PZT thin film capacitors. We show precise measurements of the strain in the film, induced by an applied electric field, piezoelectric response affected by polarization switching, and measurements of clamping effect in the thin film. Finally, we conclude with a discussion of our results in Chapter 6.

Chapter 2 Experimental Techniques

X-rays are electromagnetic radiation with wavelengths of approximately 1 Å (10^{-10} m). The wave nature of x-rays has been studied since the first x-ray diffraction experiment in 1912.[60] Since then, x-ray diffraction has been an important method in understanding the internal structure of matter. In the 1970s, synchrotron radiation sources of x-rays were introduced. These sources are much brighter than conventional x-ray sources, and they allow x-ray studies that are not possible with laboratory based x-ray sources.

The Advanced Photon Source (APS) at Argonne National Laboratory is a third generation synchrotron x-ray source. The APS is a user facility that supports 34 experimental sectors, each of which can have up to two x-ray experiment beamlines. Our x-ray microdiffraction experiments were performed at two of these facilities: sectors 2 and 7. Sector 7 can be used for time-resolved x-ray scattering, microdiffraction, and ultrafast laser excitation experiments. Sector 2 is especially designed for x-ray microbeam studies. It is used for coherent x-ray scattering and x-ray fluorescence studies with 100 nm-scale beams.

In this chapter, we introduce the synchrotron x-ray microdiffraction techniques employed in this work. First, we review x-ray sources, detectors, Fresnel zone plate focusing optics, and x-ray diffraction. Then, we describe the experimental setups of synchrotron x-ray microdiffraction and our electrical measurements in detail.

2.1 Synchrotron radiation x-ray sources

2.1.1 X-ray brilliance

In a standard x-ray tube, x-rays are generated when energetic electrons strike a metal anode. The limitation of this process is efficiency with which the target can be cooled. Eventually, the heat load on the target due to the electron beam restricts the brightness of the x-ray beams. Synchrotron radiation is the electromagnetic radiation emitted when charged particles such as electrons or positrons, traveling at relativistic velocities, are accelerated by a magnetic field. Producing x-rays in this way eliminates the thermal issue concerned to the conventional x-ray tube and provides the increased brightness.

For experiments that require a highly collimated beam of monochromatic x-rays, it is important to quantify the degree which a source of x-rays has these qualities. The brilliance represents the degree of x-ray beam produced from different x-ray sources. It can be expressed as follows.[61]

$$Brilliance = \frac{(Number\ of\ Photons)/(second)}{(mrad)^2(mm)^2(0.1\%\ bandwidth)}.$$

The brilliance depends on several aspects of an x-ray source. First, there is the number of photons emitted per second. Next is the collimation of beam which describes how much the beam diverges as it propagates for the horizontal and the vertical directions. Another factor is the beam size measured in mm^2. The last is the spectral distribution of the

x-ray beam. Third generation synchrotron sources have brilliances that are a factor of approximately 10^{10} times higher than those of the laboratory x-ray sources based on x-ray tubes.

2.1.2 Construction of synchrotron radiation source and undulator radiation

2.1.2.1 Construction of synchrotron radiation source

The APS consists of a linear accelerator, a booster synchrotron, a storage ring, and experimental halls where the x-ray experiments take place (Fig. 2.1). At the APS, electrons emitted from an electron gun are accelerated by a high electric field through a linear accelerator. The electric field accelerates the electrons to an energy of 450 MeV. The linear accelerator transfers the electrons to a booster synchrotron, which, in turn, accelerates them to the full energy (7 GeV) of the electron storage ring. At the energy of the beam, the electrons are moving at nearly speed of light. The electrons are then injected into the storage ring. At the APS, the diameter of the storage ring is approximately 400 m and the storage ring has 40 straight sections connected to bending sections. X-rays are emitted either at bending magnets placed at circular arcs or at magnetic insertion devices such as wigglers or undulators in straight sections. The insertion devices used at the APS are almost all undulators. X-rays generated in such ways then go to experimental halls. The APS has 34 experimental sectors and each sector has the potential for two beamlines, one equipped with a bending magnet and the other with an insertion device.

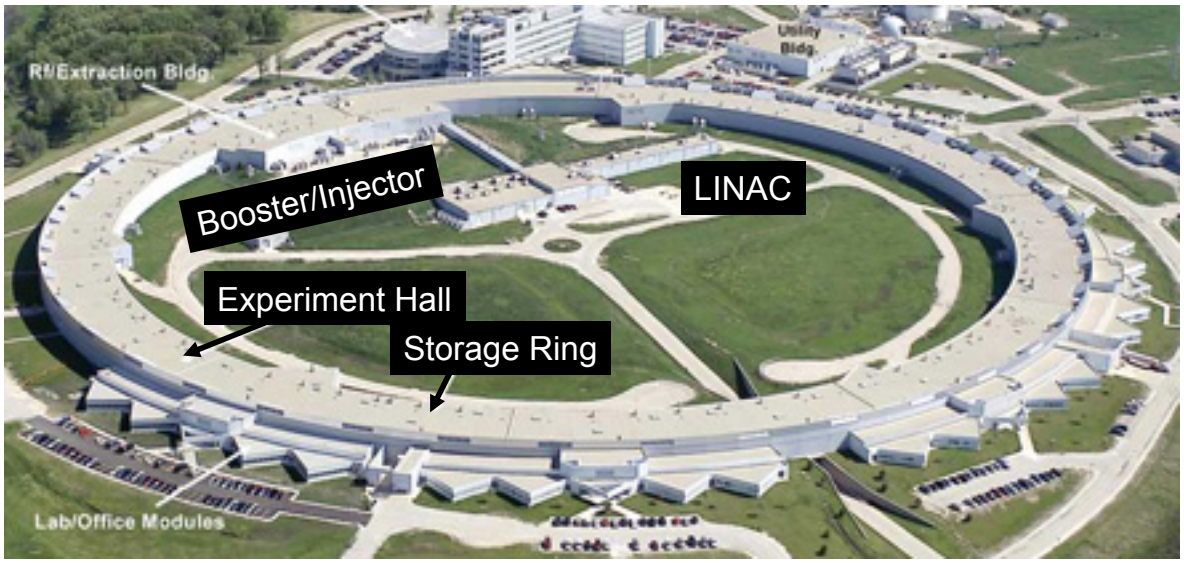

Figure 2.1 The Advanced Photon Source, a third generation synchrotron radiation source. The linear accelerator (LINAC), booster synchrotron, storage ring and experimental halls are labelled in the figure. (From www.aps.anl.gov).

Sector 7 is comprised six experimental hutches, two associated with a bending magnet beamline and four for an undulator beamline. The beamlines are shown in Fig. 2.2. We used the 7-ID-C hutch for our work.

2.1.2.2 Undulator radiation

There are two important ways to generate synchrotron radiation: bending magnets and insertion devices. Bending magnet radiation is emitted when electrons traveling at relativistic velocities are accelerated by a magnetic field. The x-rays are emitted in a direction tangential to the path of the electron. The divergence angle of bending magnet radiation is γ^{-1}, where γ is the Lorentz factor.[62] The Lorentz factor is

$\gamma = \frac{electron\ \ energy}{m_e c^2}$, where m_e is the mass of the electron (9.11×10^{-31} kg) and c is the velocity of the electron (3×10^{8} m/sec). At the APS, the divergence angle of bending magnet radiation is 0.07 mrad or 0.004˚. Bending magnet radiation has a broad spectrum.

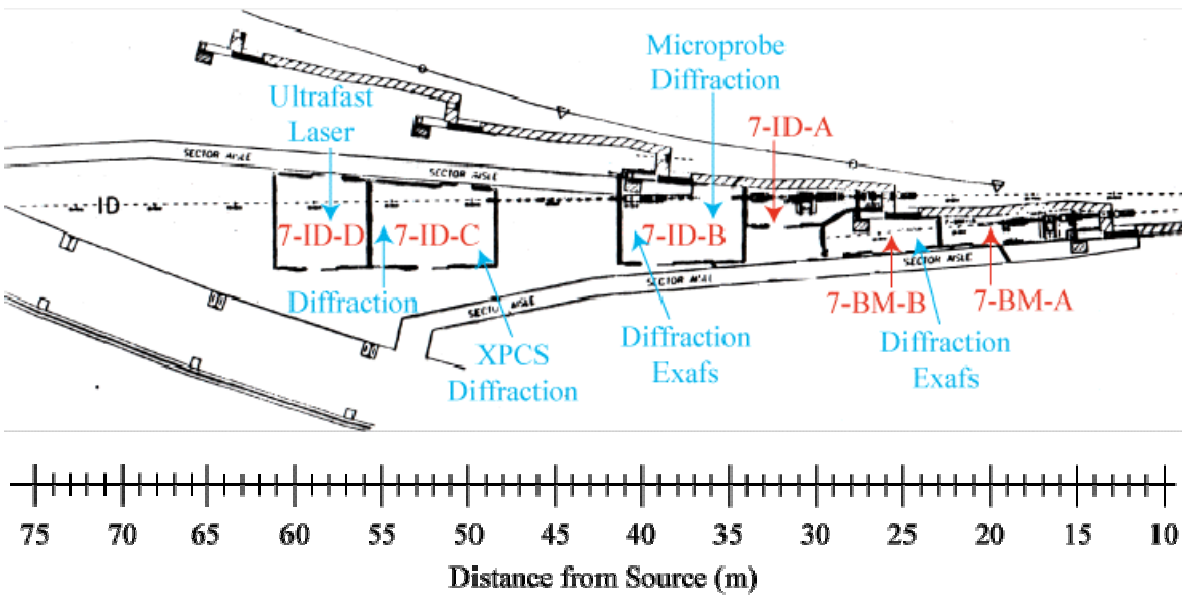

Figure 2.2 Schematic diagram of the beamlines at sector 7 at the APS. (From www.mhatt.aps.anl.gov).

Undulators are placed along straight sections in the storage ring and consist of an array of magnets separated with a periodic length (λ_u) as shown in Fig. 2.3. When electrons travel through these insertion devices, they are accelerated and periodically deflected by the magnetic field.

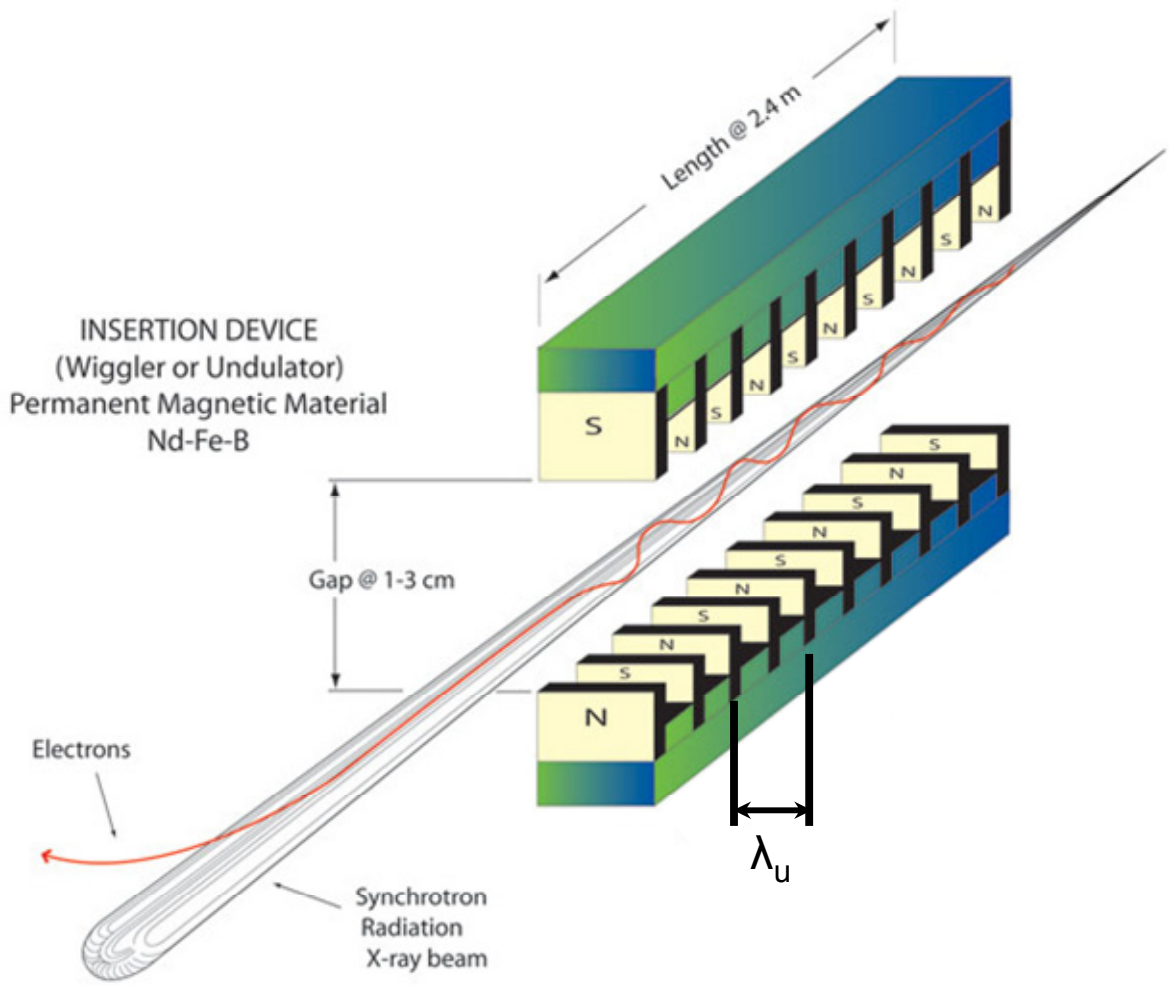

Figure 2.3 Schematic diagram of insertion device at the APS. The length of the insertion device is 2.4 m and one period of the magnetic array (λ_u) is 3.3 cm. (From www.aps.anl.gov).

Wiggler and undulator sources are parameterized by the deflection parameter, $K = 0.934\lambda_u[cm]B_0[T]$, where λ_u the magnetic period of the undulator and B_0 is the magnetic field.[63] When K>>1, the angular divergence is greater than γ^{-1}. In this case, radiation from each pair of magnet adds incoherently and has a broad spectrum, which is

the same as that of a bending magnet. This device with large K is referred to as a wiggler. In the undulator region ($K \leq 1$), the radiation generated from each pair of magnets exhibits strong interference because the divergence is smaller than γ^{-1}. The divergence angle of undulator radiation is $\frac{1}{\gamma\sqrt{N}}$, where N is the number of magnet periods.[62] At the APS, the divergence angle of undulator radiation is 0.0086 mrad or 0.0005˚. Undulator radiation produces very intense nearly monochromatic beams. An undulator radiation spectrum calculated using the XOP software package is shown in Fig. 2.4.[64]

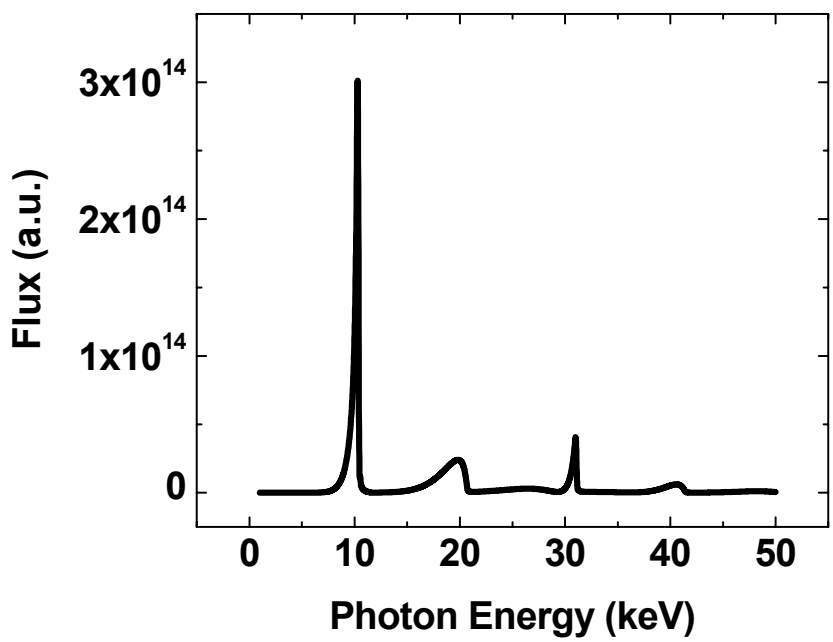

Figure 2.4 The spectrum of undulator radiation generated using XOP.[64] The 1st harmonic near 10 keV and higher harmonics are shown.

The wavelength of the nth harmonic in the undulator radiation is $\lambda_n = \frac{\lambda_u}{2n\gamma^2}(1+\frac{K^2}{2}+(\gamma\theta)^2)$, where θ is the angle between the undulator axis and the direction of the center of the beam.[62] The angle of central cone is $\theta = 1/\gamma\sqrt{N}$, where N is the number of magnet periods. When the electron energy and the number of magnet periods increase, the central cone angle decreases. The fundamental wavelength (n=1) at θ=0 is $\lambda_1 = \frac{\lambda_u}{2\gamma^2}(1+\frac{K^2}{2})$. Thus the wavelength can be chosen by changing the magnetic field. This is done by varying the gap between magnetic poles. The bandwidth of undulator radiation is $\frac{\Delta\lambda}{\lambda} = \frac{1}{nN}$.[62] In order to get high spectral brightness, the bandwidth should be narrow. Therefore, a large number of magnetic periods are required. At the APS, the bandwidth of the first harmonic in undulator radiation is approximately 1.4×10^{-2}.

Despite the highly peaked spectrum of x-rays emitted by undulator sources, the range of x-ray energies from these sources is too broad for high resolution diffraction experiments. For our experiments, a double crystal Si monochromator was used to define the energy of the x-ray beam, with an energy bandwidth $\Delta E/E$ of approximately 10^{-4}. In this monochromator, two (111)-oriented Si single crystals are rotated together to provide a tunable selection of a portion of the x-ray spectrum of the source. The beam diffracts from the first crystal and onto the second crystal which then diffracts the beam so that the beam propagation direction is parallel to the incident beam. For our work, the incoming x-ray energy of the beam was set to 10 keV. The beam energy was calibrated by measuring the

absorbing spectrum of Ta. The energy of the L_3 edge of a Ta is 9.881 keV,[63] which provides an accurate calibration of the beam energy.

2.2 Detectors

2.2.1 Ionization chambers

An ionization chamber detects x-rays by measuring the ionization of the atmosphere caused by an x-ray beam (Fig. 2.5 (a)).[61,63] It consists of two conducting metal plates, the cathode and anode, in a sealed or open chamber filled with a gas. When ionizing radiation such as x-rays passes through the chamber, the gas becomes ionized, separating positive ions and negative electrons. A high voltage of several kV applied between two plates sweeps the electrons to the anode and the positive ions to the cathode. The resulting ionization current is directly proportional to the intensity of the incident x-ray beams. This detector is simple and reliable, and, in practice, is often used to measure the intensity of the x-ray beam incident on the sample.

2.2.2 Scintillation detectors

A scintillation detector consists of a scintillation crystal and a photomultiplier tube as shown in Fig. 2.5 (b).[61,63] A pulse of visible light is generated when x-rays strike the scintillation material. This light then strikes the photocathode of the photomultiplier and electrons are emitted by the photoelectric effect. The electrons are swept to series of dynodes and the initially tiny pulse of current is amplified. The counting rate without

counting losses is calculated by $1/t_s$, where t_s is the minimum resolving time between two pulses.[61] Scintillation detectors have a time resolution of about 1 μs. Thus the counting rate is linearly proportional to the intensity of the incident x-ray beam for count rates up to approximately 10^6 counts per second.

2.2.3 Avalanche photodiode (APD) detectors

Some of the limitations of scintillation counters, particularly in terms of low count rates, can be overcome using solid state detectors such as Si avalanche photodiode (APD) detectors. APD detectors consist of a photodiode and an amplifier. When an incident x-ray photon is absorbed in depletion region of the photodiode, electron-hole pairs are created by the photoelectric effect (Fig. 2.5 (c)).[65] The electrons and holes are accelerated in the large electric field applied across the depletion region. Electrons with enough energy drift through the avalanche region and then scatter. Additional electron-hole pares are created, and the process is repeated. The APD thus has internal gain.

The time resolution of the APD detector is determined by the high electric field drift velocity in silicon. For Si, the velocity is 100 μm ns^{-1}. Thus a 100 μm-thick detector can be used for detecting photons arising from single electron bunches separated by 153 ns at the APS. Another advantage of APD detectors is a high maximum count rate. Due to the short pulse width, this detector can count up to 10^8 photons per second.[66]

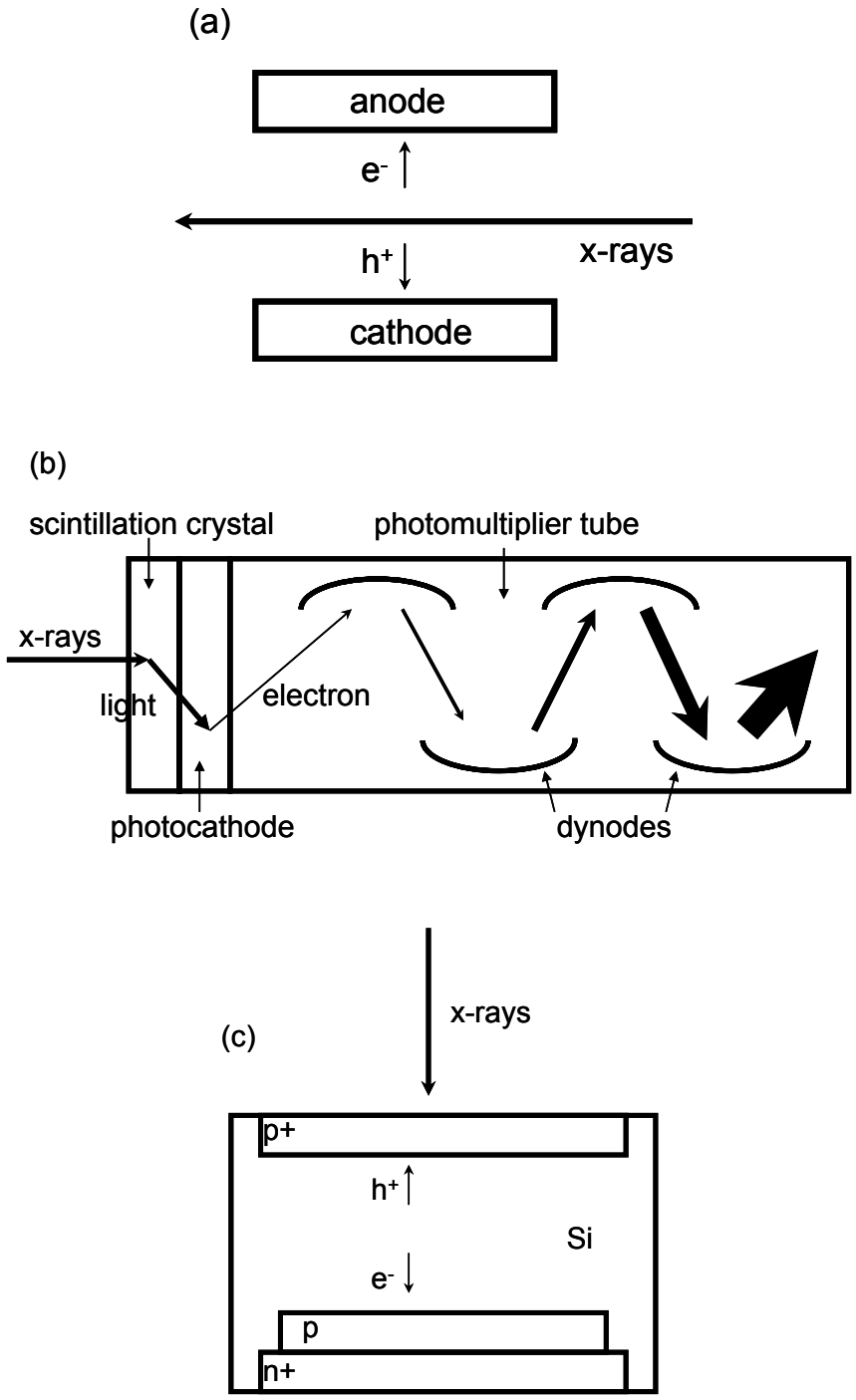

Figure 2.5 Schematic diagrams of (a) ionization chamber, (b) scintillation detector, and (c) avalanche photodiode detector.

2.3 Fresnel zone plate x-ray focusing optics

A Fresnel zone plate (FZP) was used to focus an incoming x-ray beam. The FZP is an optical element that uses diffraction of an incoming x-ray beam to focus x-rays to a small spot.[62,63] The FZP consists of a series of circular zones. Interference occurs when the path length between adjacent transparent zones in the zone plate and the focal spot differs by one wavelength of the incident x-rays. The path length at the nth zone is increased by $n\lambda/2$, where λ is the wavelength of x-rays. A center stop and an order sorting aperture (OSA) are used with the FZP so that only light from the first order of diffraction reaches to the focal spot (Fig. 2.6).

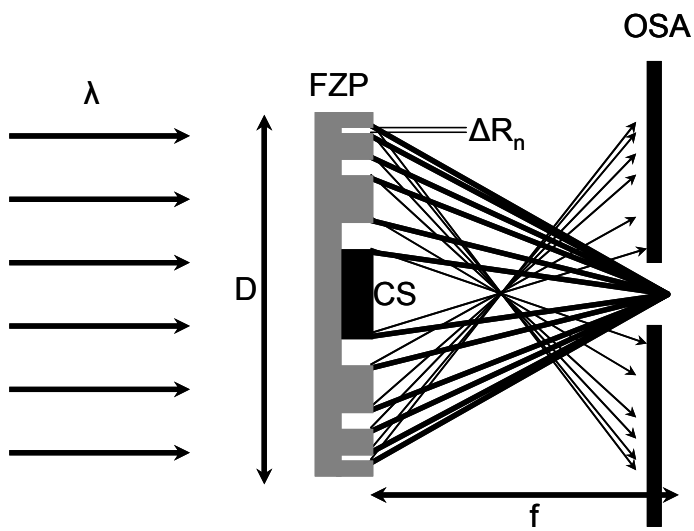

Figure 2.6 Schematic diagram of a FZP, and 1st and 2nd orders of focal spot. The zero order is blocked by a center stop (CS) and 2nd and above orders are blocked by a order sorting aperture (OSA).

The focal length of a FZP is $f = D\Delta R_n / \lambda$, where D is the diameter of the zone plate, ΔR_n is the width of the outmost zone, and λ is the wavelength of x-rays (Fig. 2.6).[62] The ultimate spatial resolution of a FZP is defined by the outmost zone width, ΔR_n. The focal spot has a width of $1.22\Delta R_n$ at the Airy edge of the first Airy dish.[62]

The FZP used in our experiments was manufactured by Xradis Inc. (Concord, CA). It had a diameter of 160 μm and an outmost zone width of 50 nm. Thus the focal length was 64.5 mm and a beam divergence is approximately 0.07°. The height of the zones is 700 nm, which gives a focusing efficiency of 10% at an x-ray energy of 10 keV.[67]

The synchrotron x-ray microdiffraction setup is shown in Fig. 2.7. In our experiments, the FZP was placed 64.5 mm from the sample in order to focus incoming x-rays using the first diffraction order. An OSA of 30 μm in diameter was placed 10 mm from the sample. Before focusing the beam, the FZP was aligned to the beam path while observing x-ray beam on a fluorescent crystal using a video microscope. The FZP was positioned in the x-ray beam by x-, y-, and z-axis mechanical translation stages. We measured actual size of the focused x-ray beam using the x-ray fluorescence of a Cr thin film knife-edge. By scanning the Cr knife-edge in the vertical direction across the beam, we were able to measure the width of the onset of the fluorescence and interpret it in terms of the width of the focused x-ray beam. The position of the zone plate was optimized by adjusting the distance between it and the Cr knife-edge. The best spatial resolution we achieved was approximately 100 nm (Fig. 2.8).

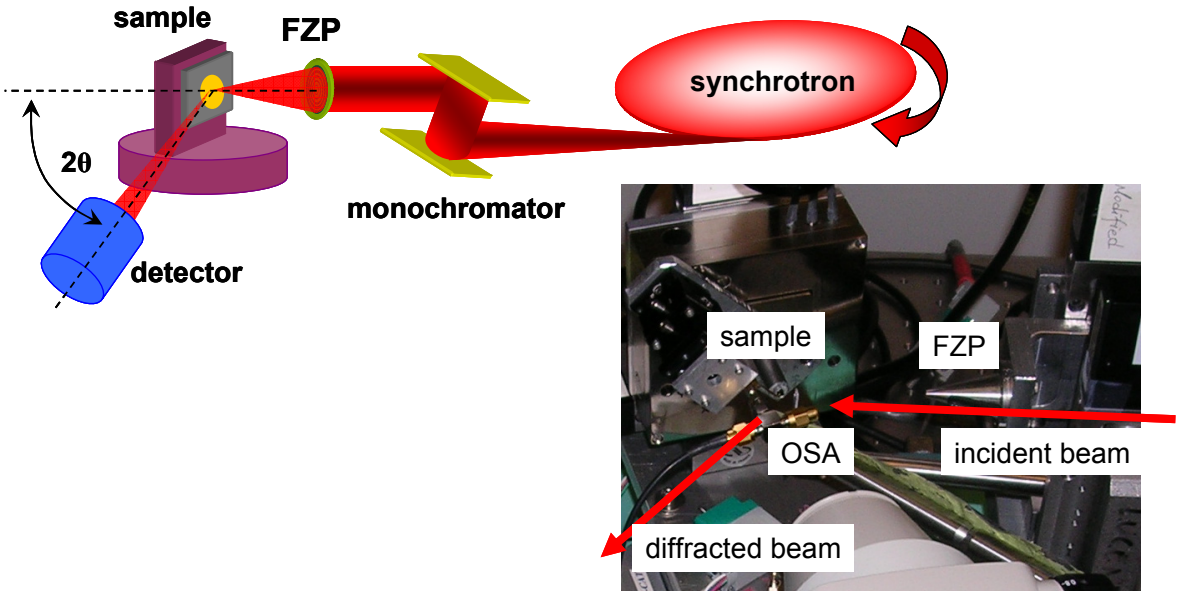

Figure 2.7 Schematic diagram and a photograph of the synchrotron x-ray microdiffraction setup at sector 7-ID-C hutch at the APS.

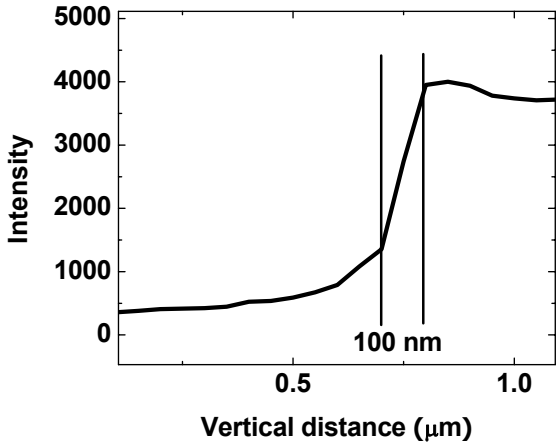

Figure 2.8 The fluorescence intensity as a function of distance during a Cr knife-edge scan. The beam size was determined to be 100 nm.

The theoretical spatial resolution which can be achieved from the FZP we used is 61 nm. The limitation to get the best performance was mainly due to the vibration of the microdiffraction apparatus.

2.4 Diffractometer alignment

In order to know the angles associated with the scattered x-ray beams, it is necessary to accurately place the sample on the point defined by the intersection of the axes of rotation of the diffractometer. We found the center of rotation using a pin and an optical microscope. The pin sat on a sample stage that is positioned by x-, y-, and z-axis mechanical translation stages and a piezoelectric fine motion xyz stage. While observing the tip of the pin using the microscope, the rotation stages were rotated in the directions normal and perpendicular to the beam direction. The tip position was aligned using the translation stages until the tip did not move when the stages were rotated. After finding the center of rotation, the tip of the pin was aligned to the x-ray beam path by observing the shadow of the tip on a fluorescence crystal using microscope and translating the entire diffractometer.

After aligning the focused beam with the center of rotation, the sample was mounted on the diffractometer and was aligned for diffraction in the Bragg geometry. On the detector arm, a slit was positioned immediately before the detector. This ensured that only diffracted x-ray beam at the desired Bragg angle reached the detector. The width of the slit was approximately 1×1 mm^2.

For the experiments in Chapters 3 and 4, involving imaging of polarization domains, the scintillation detector was used. The intensity of incident x-ray beam was recorded by an ion chamber in order to normalize the measurements of the intensity of the diffracted beam. For measurements of the piezoelectric response in Chapter 5, an APD detector was used in order to be able to measure higher count rates.

2.5 X-ray diffraction

An initially collimated x-ray beam is scattered into all directions by atoms. In a periodic structure, however, the intensity of the scattered x-rays in most directions is zero. Enhanced beams are scattered in some directions, which is called diffraction. X-ray diffraction in crystalline solids takes place because the wavelength of x-rays is approximately equal to the interatomic distance in crystals.

X-ray diffraction is a result of constructive or destructive interference due to the phase relationship between beams of elastically scattered x-rays. In Fig. 2.9, the path difference between the x-rays scattered from planes 1 and 2 is $\overline{OA}+\overline{OB}=d\sin\theta+d\sin\theta$. In order to have constructive interference of the scattered x-rays, the distance of $\overline{OA}+\overline{OB}$ must be equal to an integer number of wavelength (λ) of the x-ray radiation. Thus, $\overline{OA}+\overline{OB}=n\lambda$ (n=1,2,3,…). Since $\overline{OA}+\overline{OB}=d\sin\theta+d\sin\theta=n\lambda$, $2d\sin\theta=n\lambda$. This requirement is referred to as Bragg's Law and describes the angular position of the diffracted beam in terms of λ and d.

In more general terms, for example, in more complex crystals, it is possible to consider planes of unit cells rather than planes of atoms. X-rays are scattered by all atoms of each unit cell. The intensity and phase of the waves scattered by each unit cell can be expressed using the structure factor, which is the sum of scattered waves from all the atoms of the unit cell.

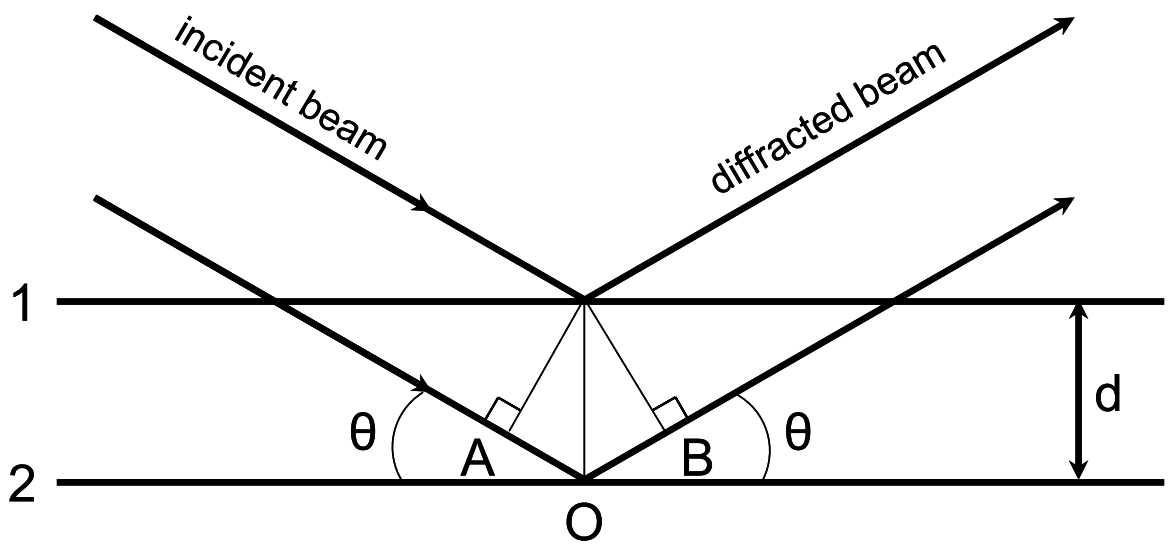

Figure 2.9 The geometry of x-ray reflection by planes of atoms in a crystal. Constructive interference occurs when the path length difference is equal to an integer multiple of the wavelength of the x-ray beam.

The structure factor is given by $F(hkl) = \sum_j f_j \exp[2\pi i(hu_j + kv_j + lw_j)]$, where f_j is the atomic scattering factors of atom j and (u_j, v_j, w_j) are the fractional coordinates of the jth atom in the unit cells.[7] The atomic scattering factor is $f_j = f_j^o + f_j^{'} + if_j^{''}$, where f_j^o

is the atomic form factor of atom j, $f_j^{'}$ and $f_j^{''}$ are the real part and the imaginary part of the anomalous dispersion of atom j.

The structure factor is sensitive to the distribution of atoms in a unit cell because it includes the amplitude and phase of the scattered wave. For example, when the positions of atoms within the body centered cubic lattice and face centered cubic lattice are used to compute F, we find that there is no (111) reflection from the body centered cubic but a strong (111) reflection from the face centered cubic lattice.

2.6 Electrical measurements

In order to study ferroelectricity in PZT thin film capacitors, we performed electrical measurements using the circuit shown in Fig. 2.10. Voltage pulses were generated from a function generator (model 33120A, Agilent) and the responding voltage was measured using an oscilloscope (model TDS1012, Tektronix). The output current then calculated from the responding voltage with the resistance of the resistor we used.

The voltage applied across the ferroelectric capacitor was a triangular wave in our measurements. The current that could be expected for a capacitor with a linear dielectric would be $I(t) = C\frac{dV}{dt}$. This current results in 0.03 mA of current solely due to the linear polarizability of the ferroelectric. In addition, there are large transient currents that flow when the applied voltage reaches the positive and negative coercive voltages. These large transient currents cease when the polarization switching is completed.

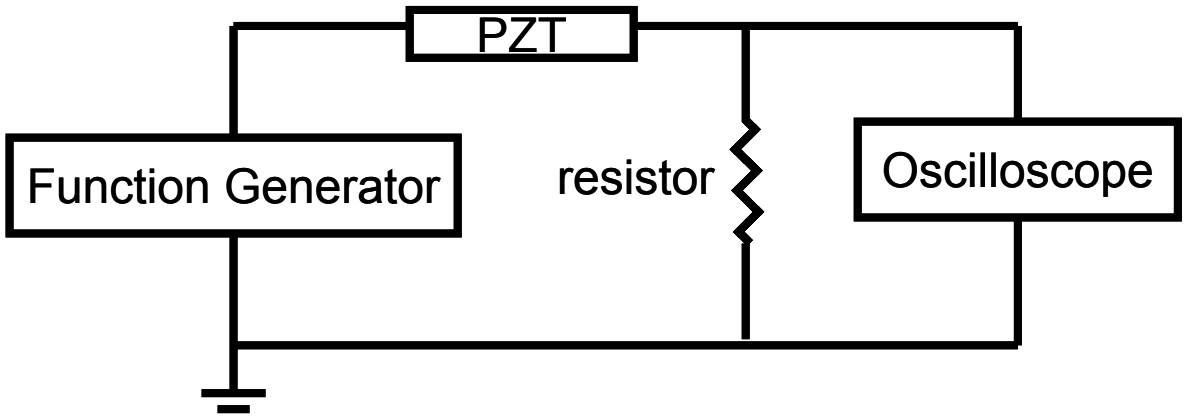

Figure 2.10 Schematic diagram of the electrical circuit used in the experiments. The resistance of the resistor in our experiments was 1 kΩ.

An example of this measurement is shown in Fig. 2.11 (a). The amount of polarization is $P = \frac{Q}{A} = \frac{\int I(t)dt}{A}$, where A is the area of a capacitor. A polarization-electric field hysteresis loop measured in the PZT thin film capacitor is shown in Fig. 2.11 (b). From the hysteresis loop, one can measure the value of coercive voltage and remnant polarization of a ferroelectric material. For the hysteresis loop in Fig. 2.11 (b), the value of remnant polarization is about 47 μC cm^{-1} and the values of positive and negative coercive voltages are 2.2 and -2.2 V, respectively.

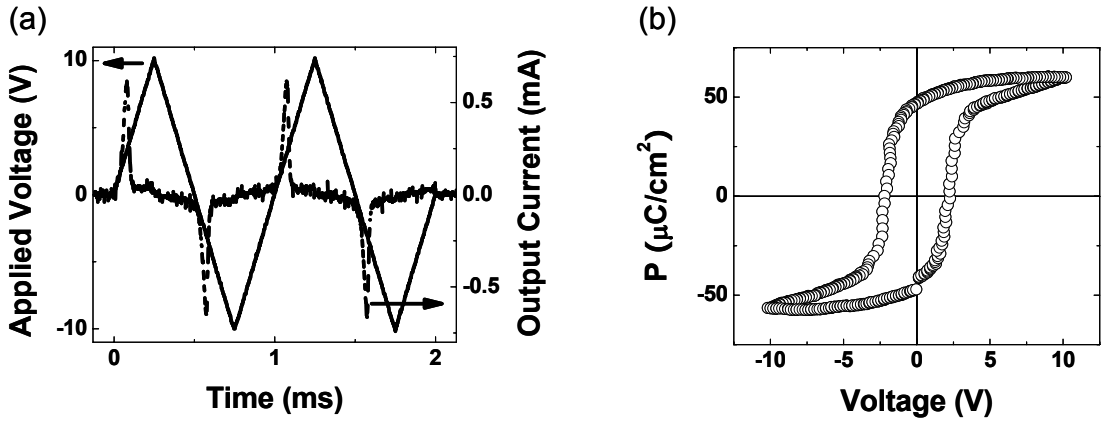

Figure 2.11 (a) Applied voltage and switching current as a function of time and (b) polarization-electric field hysteresis loop produced from (a). The hysteresis loop shown in (b) was measured in 800 Å thick PZT film capacitors. The size of the capacitor was ($\pi \times 100^2$) μm^2.

Chapter 3 Imaging Polarization Domains

3.1 Introduction

In ferroelectric materials, a poled state that often consists of a single domain can be obtained by applying an electric field larger than coercive electric field. A sufficiently large electric field leads to the reorientation of electric polarization to point along the electric field direction. This is known as polarization switching.[9] The polarization switching process is reversible. Since polarization switching is the defining property of ferroelectric materials, understanding how polarization switching occurs is important from both scientific and technological points of view.

In the simplest model of polarization switching, the starting and end points of the switching process are uniformly polarized states. In general, the transformation between uniform states occurs through a domain nucleation and domain growth process.[9] Polarization switching includes nucleation, forward growth through the thickness of the sample, and lateral propagation of opposite polarization domains (Fig. 3.1).[68] The kinetics of polarization switching have been extensively studied. However the dynamic response is still unclear because of the difficulty involved in real time observation of ferroelectric domain motion.

There have been numerous efforts to understand the mechanism of polarization switching and to relate it to the simplest model shown in Fig. 3.1. The polarization

switching process can be investigated entirely on the basis of electrical probes by examining the current that flows in response to a pulsed electric field. The basic principle of this method is the measurement of the transient current that flows during polarization switching.[69] In this case the applied electric field is homogeneous through the whole device. However, the interpretation of the current response is difficult and only average properties such as the integrals of the switchable polarization, the remnant polarization, and values of the coercive field are available.

Another way to study polarization switching is based on the visualization of polarization domains in ferroelectric capacitors.[70] In this way, one can study the evolution of polarization domains during the switching process. The most widely used domain imaging techniques for ferroelectric thin film capacitors are based on observing the piezoelectric response of the film using atomic force microscopy (AFM). Since the AFM tip is used as one of electrodes, the spatial resolution is about 10 nm which corresponds roughly to the radius of the AFM tip. Thus polarization switching can be investigated at small scales.[71] Imaging of the domain structure is based on the interaction between the tip and the top surface of a film.[72] While the tip is in contact with the surface, a voltage pulse is applied, and the electromechanical vibration of the ferroelectric materials is detected by the cantilever. The polarization direction can be determined based on the phase of piezoelectric response related to the applied voltage.

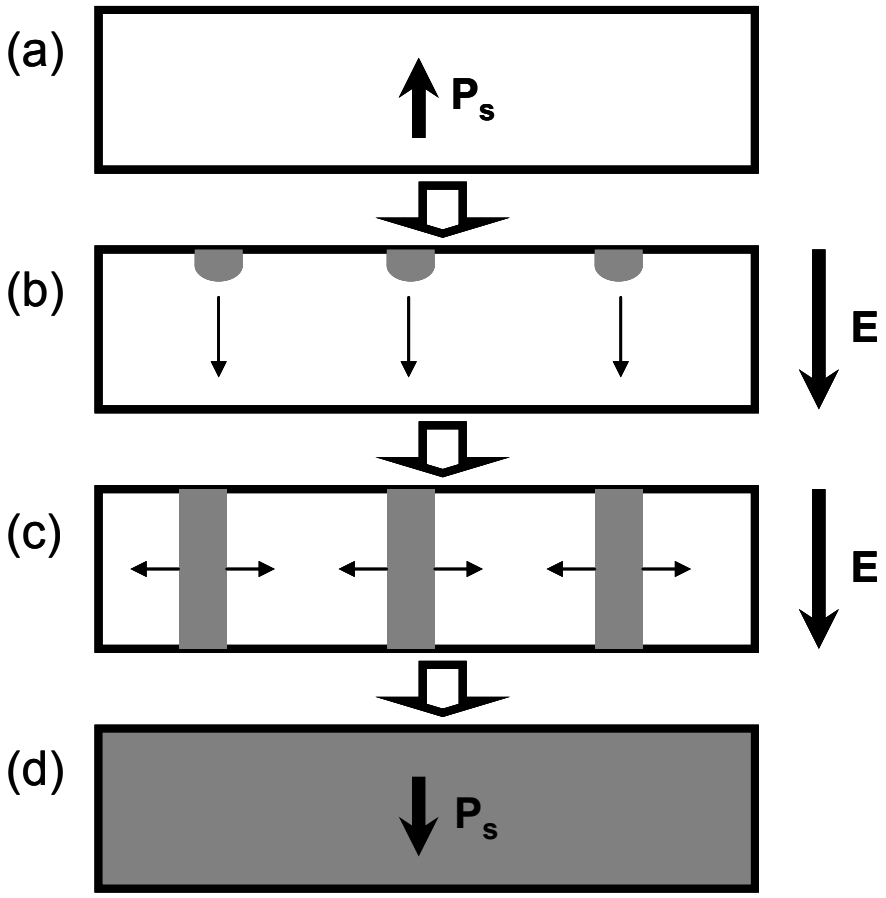

Figure 3.1 The polarization switching process. (a) The initial polarized state, (b) nucleation of domains with the opposite polarization in a large electric field, (c) forward growth of the domains through the thickness of the sample, and (d) complete switching after lateral propagation of the domain walls.

X-ray diffraction techniques have become an important tool for investigation of domain structures and domain wall motion in ferroelectric materials.[73,74] Ferroelectric domains can be visualized using x-ray diffraction due to the lack of inversion symmetry in the unit cell.[75,76]

In this chapter, we show that images of polarization domains in PZT thin film capacitors can be made using x-ray microdiffraction techniques. The contrast in these images is based on the difference in the intensities of the (002) and $(00\bar{2})$ x-ray reflections of PZT. X-ray microdiffraction observations and electrical measurements of polarization switching are easily related since both provide a quantitative probe of the polarization.

3.2 Experimental details

Epitaxial $Pb(Zr_{0.45}Ti_{0.55})O_3$ (PZT) thin films with thicknesses of 800 and 1600 Å were grown by our collaborators in the research group of Prof. Chang-Beom Eom. The substrate was a (100)-oriented 500 μm thick $SrTiO_3$ (STO) single crystal. The oxide thin films were deposited using off-axis radio-frequency magnetron sputtering.[38] In order to produce thin films that are in the tetragonal crystal phase at room temperature, the Zr:Ti ratio was selected to be 45:55. A $SrRuO_3$ (SRO) bottom electrode layer with a 1000 Å thickness was grown on the STO substrate followed by the PZT thin film layer. A Pt top electrode was sputter-deposited on the PZT layer using a 200 μm-diameter shadow mask, and then annealed under an oxygen atmosphere at 300 °C for 30 min. The structure of the PZT thin film capacitors is shown in Fig. 3.2(a).

We determined the crystallographic orientation of the PZT capacitors using laboratory x-ray diffraction studies. Cu $k\alpha_1$ x-rays with a wavelength of 1.5406 Å were used for the measurement. The results of the diffraction measurements of the PZT films are shown in Fig. 3.2(b). The θ-2θ scan measures the spectrum of out-of-plane lattice constants

in the part of reciprocal space near the PZT (002) Bragg reflection. The majority of the PZT was oriented with the tetragonal c-axis along the surface normal. The small peak near the SRO (220) indicated that there is a small amount of PZT in the thinner film that has its tetragonal a–axis along the surface normal. The direction of the majority of the spontaneous polarization is thus normal to the surface of the sample. The peak marked with * between PZT and SRO came from the aluminum sample holder we used. Electrical measurements of the switchable polarization of this sample are shown in Fig. 2.11, and were discussed in Chapter 2.

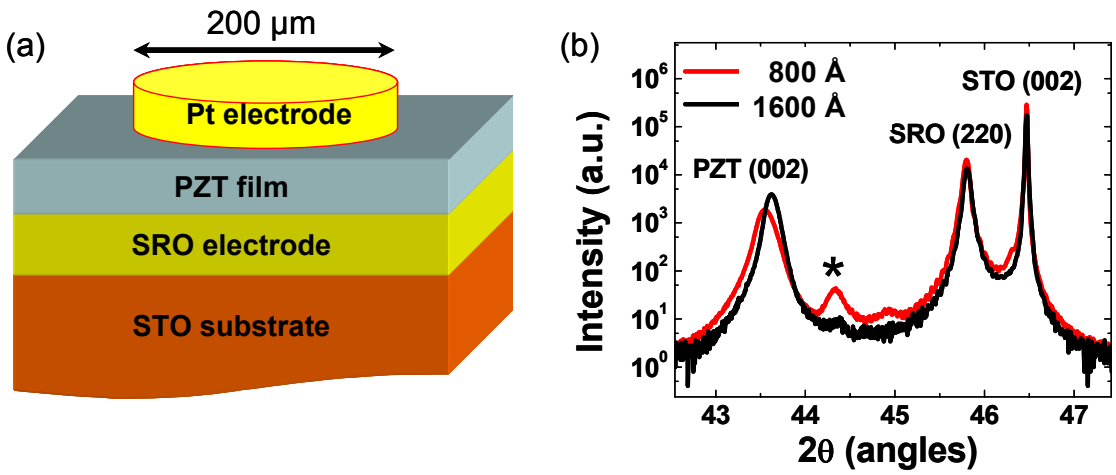

Figure 3.2 (a) Schematic diagram of the structure of an epitaxial PZT thin film capacitor and (b) x-ray diffraction results of the θ-2θ scan of 800 and 1600 Å thick PZT films. The peak marked with "*" between the PZT (002) and the SRO (220) reflections comes from an aluminum sample holder.

The 800 Å thick PZT films were used to show that x-ray microdiffraction techniques can be used to image ferroelectric polarization domains. The x-ray experiments

on these samples were performed without removing the sample from the diffractometer to apply external electric fields, which allowed measurements at identical reflection angles and sample position for each electrical polarization. Electrical contact to the top electrode was maintained during the diffraction experiments using a 25 μm-diameter Pt wire spring which allowed diffraction experiments to be made on the majority of the area of the capacitor device. Polarization domains were imaged by scanning the sample in the focused x-ray beam while the intensity of PZT (002) reflection is mapped. The diffracted x-ray beam was detected using scintillation detector. The measurements in this chapter were conducted with an early version of x-ray microdiffraction apparatus which had a spatial resolution of only 600 nm.

3.3 Results and discussion

3.3.1 Images of polarization domains

Images of the ferroelectric polarization within the PZT thin film capacitor were made by mapping the intensity of the PZT {002} reflections as a function of the position of the x-ray beam on the sample. The intensity of an x-ray reflection with miller indices (*hkl*) is proportional to $|F(hkl)|^2$. When atomic scattering factors are real, $|F(hkl)|^2$ is equal to $|F(\bar{h}\bar{k}\bar{l})|^2$. This effect is known as Friedel's law. It is not true, however, when the atomic scattering factors have a non-zero complex part. This effect can be applied to ferroelectric materials. For example, (002) and $(00\bar{2})$ reflections from the PZT occur at the same

Bragg angle but have different intensities due to the noncentrosymmetric structure of PZT. The atomic scattering factors for each atom in PZT are given in Table 3.1, based on tabulated values.

Table 3.1 f^o, $f^o + f'$, and f'' of Pb^{2+}, Ti^{4+}, Zr^{4+}, and O^{2-} ions in electrons. The parameters were taken from XOP.[64]

	f^o	$f^o + f'$	f''
Pb^{2+}	66.2470	77.2931	6.3669
Ti^{4+}	14.8331	22.3895	1.2752
Zr^{4+}	29.5633	39.4830	1.5610
O^{2-}	4.9520	8.0358	0.0211

Our PZT thin film has two possible polarization states along the surface normal direction since the PZT has a c-axis oriented tetragonal structure along the surface normal. Figure 3.3 shows the schematic diagrams of atomic positions in PZT unit cell in two stable polarization states. The fractional atomic positions of Pb, Ti, Zr, and O atoms are given in Table 3.2. The atomic positions in Table 3.2 are derived from powder diffraction studies of bulk tetragonal PZT with a composition of Zr:Ti of 52:48. These specific values are likely accurate for PZT films in which it is difficult to study enough x-ray reflections to accurately refine the structure. Applying an electric field greater than the coercive field

switches the polarization by displacing Ti atoms along the c-axis with respect to the Pb atoms. When a positive voltage pulse is applied to the bottom electrode of the thin film, the Ti atom switches so that it is displaced toward the surface of the thin film. In terms of the picture in Fig. 3.3 (a), the Ti atom is above the middle of the unit cell and the polarization direction points up. The Ti atom moves below the middle of the unit cell and the polarization direction points down after a negative voltage pulse is applied to the bottom electrode (Fig. 3.3 (b)). In the two remnant polarization states, thus the relative atomic positions are different but the lattice constant of PZT is the same. In the x-ray diffraction, the diffracted intensity is sensitive to the atomic positions in noncentrosymmetric crystal structures.

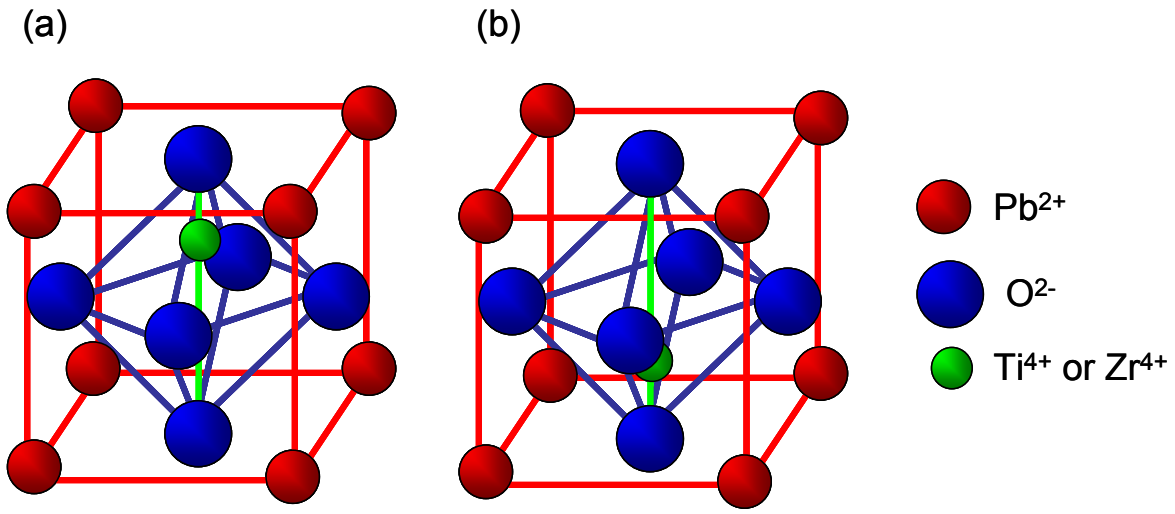

Figure 3.3 Perovskite $Pb(Zr,Ti)O_3$ structure illustrating two polarization states with a Ti (Zr) atom shifted (a) up and (b) down. The lattice constant is the same in two polarization states.

Based on the values of the atomic scattering factors in Table 3.1 and the fraction of atomic positions in Table 3.2, the contrast between two reflections related by inverting the polarization can be estimated. The structure factor of the (*hkl*) x-ray reflection is $F(hkl) = \sum_j \{(f_j^o + f_j^{'} + if_j^{''}) \exp[2\pi i(hu_j + kv_j + lw_j)]\}$. The calculated ratio of the intensities of the PZT (002) and $(00\bar{2})$ reflections is $R = \frac{|F(00\bar{2})|^2}{|F(002)|^2} = 0.932$. The result indicates that difference between the intensities of the PZT (002) and $(00\bar{2})$ reflections should be (1-*R*)=7%. Note that the PZT (002) reflection has higher intensity than that of the PZT $(00\bar{2})$ reflection according to this prediction.

Table 3.2 Fractional atomic positions of Pb, Ti, Zr, O atoms in the unit cell of tetragonal PZT.[77]

	Atomic position		
	u	*v*	*w*
Pb	0	0	0
Ti or Zr	0.5	0.5	0.4517
O(1)	0.5	0.5	-0.1027
O(2)	0.5	0	0.3785
O(3)	0	0.5	0.3785

In order to verify this prediction, θ-2θ scans were performed around the angles where reflections from PZT and SRO appear on samples in the two opposite polarization states. The two states were prepared by applying positive and negative 10 V triangular voltage pulses of 500 μs duration to the bottom electrode. According to electrical measurements (Fig. 2.11), applying 10 V pulses switches the spontaneous polarization completely. Figure 3.4 shows the results of θ-2θ scans in the two opposite polarization states. The SRO peaks in two scans were normalized to compare the intensity and peak position of PZT (002) and $(00\bar{2})$ reflections. The polarization state appearing after applying a negative 10 V pulse to the bottom electrode has higher intensity than a positive 10 V pulse. The difference in the intensities of the PZT (002) and $(00\bar{2})$ reflections was approximately 33%. The angles of the peaks belonging to the two reflections were the same. The result simple indicates that two opposite polarization states can be distinguished by comparing the difference in the intensities of the PZT {002} reflections.

In order to visualize polarization domains, area maps of the intensity of the surface-normal PZT {002} reflections in the two remnant polarization states were acquired. X-ray images acquired following positive and negative 10 V pulses are shown in Fig. 3.5. The images were taken in identical regions of the PZT capacitor. The area covers regions that are inside (below the arc) and outside (above the arc) the area covered by the top electrode. The images show the change in the intensity of x-ray reflection as a result of switching from one polarization state to the other. In each state, the area not covered by the top electrode has almost the same intensity, implying that spontaneous polarization is oriented

in the same direction. The two oppositely polarized domains can be clearly distinguished by comparing the intensity. The average intensity difference in two images is approximately 30%, far larger than the prediction based on the structure factor. There is no intensity difference outside the device in two images.

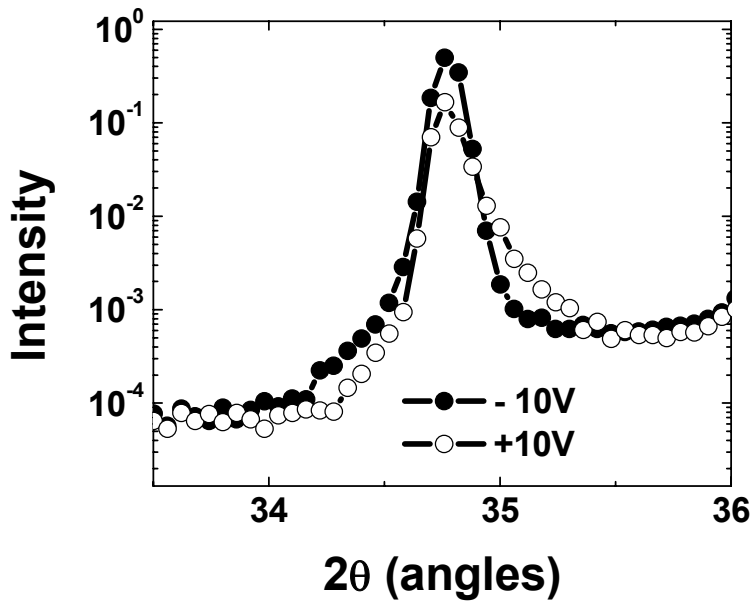

Figure 3.4 PZT {002} reflections after applying positive and negative 10 V pulses. The scans show the same peak angle but different intensity in the two opposite remnant polarization states.

These experiments are consistent with the prediction that the PZT (002) reflection has higher intensity than PZT $(00\bar{2})$ reflection. However, the intensity difference between PZT (002) and $(00\bar{2})$ reflections in our observation is much higher than the values we estimated. In order to interpret the origin of the difference between the observation and the

calculation, we considered the role of uncertainties in both the atomic positions and the atomic scattering factors. First, we suspect that the atomic positions in the unit cell of the PZT thin film could be different than for bulk PZT. We checked this hypothesis by computing *R* while adjusting the fractional atomic positions of each atom in the range of ± 0.005 with respect to their original positions. In this range, *R* was still 7% and no significant change in *R* was observed. Intensity differences of up to *R*=14% could be observed by changing Ti atomic position to 0.2517. This, however, is clearly not physically reasonable and we suspect that no reasonable change in the positions of the atoms within the unit cell could account for the observed *R*.

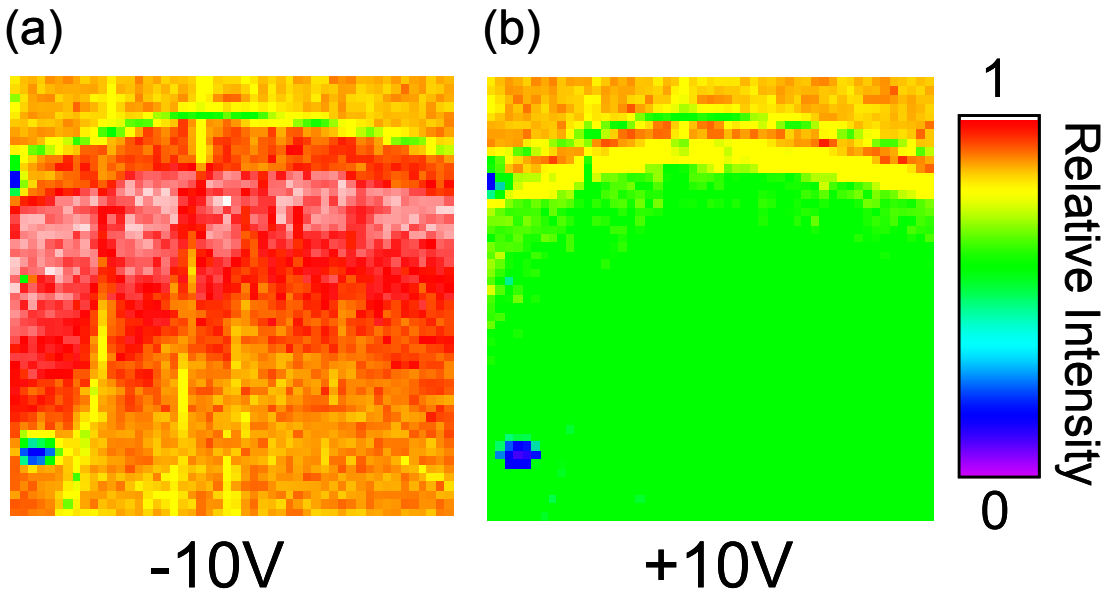

Figure 3.5 Images of the intensity of PZT {002} reflections in two polarization states. The region with low intensity (blue in images) is structurally defective. The area of each image is 100×100 μm^2.

The atomic scattering factors of each atom in the PZT thin film may be different than for the ions listed in Table 3.1. We could get intensity differences of only R=8% by changing the values of f^o in each atom. The results imply that atomic positions in the given ranges and atomic scattering factors do not give the significant intensity difference. Therefore there are other sources that make large intensity difference in x-ray measurements, possibly strain.

The experimental results indicate that x-ray microdiffraction can be used to study the polarization domains and polarization switching in operating devices, PZT thin films with top and bottom electrodes. Upon polarization switching, x-ray images show that the intensity of the x-ray reflection changes by 30% between two opposite polarization states. The changes in the intensity provide that polarization switching is a result of the relative displacement of the noncentrosymmetric atoms in PZT thin films.

3.3.2 Relating x-ray microdiffraction and electrical measurements of polarization switching

In order to understand what happens inside PZT thin films during the polarization switching process, the evolution of polarization domains was investigated by applying voltage pulses near the coercive voltage. Applying the voltage pulses lead to partial polarization switching in PZT capacitors. The results of x-ray microdiffraction observations were compared to those of electrical measurements.

Figure 3.6 (a) shows x-ray images of the evolution of polarization domains during the polarization switching process. Triangular voltage pulses of 500 μs total duration were applied to the bottom electrode with positive amplitudes of 0.8, 1.2, 1.6, 2.0, and 2.8 V. Before applying the each positive voltage, a negative 10 V pulse was applied to switch the capacior into the negative state. The negative 10 V magnitude of this reset pulse is larger than the negative coercive voltage, -2.2 V, measured using the hysteresis loop (Fig. 2.11). The positive voltage pulses near the coercive voltage were expected to result in a partial polarization switching in the capacitor.

Following each pulse, images of the intensity of the PZT {002} reflections were acquired. Applying a positive 10 V pulse provided complete polarization switching from one polarization state to another (Fig. 3.5). At voltages near the coercive voltage, however, the images showed the area of the region in which the intensity did not change. The area reduced with applying higher amplitude of voltage pulses. Eventually the device switches completely. The direction of polarization switching is from the center of device to the edge. Although the experiments were performed with a static process, they show that the role of lateral propagation of domain wall is important for polarization switching process.

Figure 3.6 (b) shows the relationship between x-ray microdiffraction observations and simultaneous electrical measurements of polarization switching. The fraction of switched area in the x-ray images at each applied voltage and corresponding remnant polarization measured electrically were calculated from these images. The switched area in the images was correlated with the value of the switched polarization. This result shows

that x-ray microdiffraction can be used to study local polarization switching in ferroelectric materials.

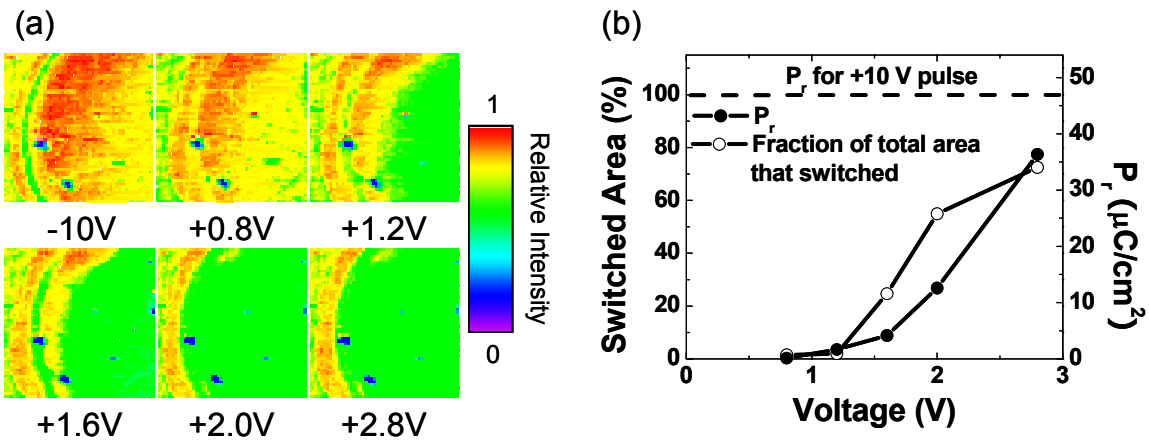

Figure 3.6 (a) Microdiffraction images of polarization reversal in a PZT sample with Pt electrodes and (b) the relationship between the switchable polarization measured electrically and the fraction of switched area obtained from the x-ray microdiffraction images. The area of each image is 100×100 μm^2.

In late work not described here, we have extended this technique to study the dynamics of polarization switching by imaging the motion of domain walls using time-resolved x-ray microdiffraction. The velocity of the domain walls can be investigated by comparing time of the change in intensity at different positions in the device. In order to measure the velocity, we used single x-ray bunches which provide time resolutions of 100 ps. The domain wall motion was visualized in area maps of the switching time and a domain wall velocity of 40 m s^{-1} was observed.[78]

3.4 Conclusion

Images of polarization domains can be formed by mapping the intensity of the x-ray reflections from PZT thin film capacitors using synchrotron x-ray microdiffraction. The x-ray images provide not only the difference in intensities in two opposite polarization states but also the displacement of the noncentrosymmetric atoms in PZT. In two oppositely polarized states, the intensity difference was 30% in the (001) oriented PZT thin film capacitor. The degree of polarization switching was observed by comparing intensity difference and the total switched polarization agreed well with electrical measurements. X-ray microdiffraction measurements hold promise as a new way to study polarization switching in ferroelectric devices at small length scales with quantitative structural specificity.

In next chapter we will show the x-ray images of the evolution of polarization domains during polarization fatigue and explain mechanisms of polarization fatigue in PZT thin film capacitors.

Chapter 4 Polarization Fatigue in PZT Thin Films

4.1 Introduction

There are several fundamental issues concerning the integration of ferroelectric thin films in nonvolatile memory. Polarization fatigue is the suppression of switchable polarization after a number of switching cycles.[4,5] Many experimental and theoretical studies have been attempted to understand the fatigue phenomenon. As a result, several mechanisms have been proposed to explain origin of polarization fatigue and a number of ways to improve fatigue resistance have been developed.

Polarization fatigue is closely linked to polarization switching and to the reorientation of polarization domains. Electrical measurements are the most common way to investigate polarization fatigue.[69,79] Changes in polarization hysteresis loops before and after fatigue can be linked to changes in the ferroelectric materials and to the microscopic origin of fatigue.

Imaging polarization domains in conjunction with the electrical measurements provides an opportunity to investigate the evolution of polarization domains during the fatigue process. Synchrotron x-ray microdiffraction is a structural probe with sub-micron spatial resolution that provides a new way to observe the real space evolution of polarization domains and the development of fatigue in ferroelectric devices. In this chapter we investigate the origin of the polarization fatigue based on images of polarization

domains using the x-ray microdiffraction technique. We investigated polarization fatigue in PZT thin film capacitors with Pt top electrodes at low and high electric fields. In order to understand the effects associated with the chemical composition of the electrode, we studied PZT films with SRO electrodes. The origin of polarization fatigue is discussed based on the results of x-ray microdiffraction and electrical measurements.

4.2 Experimental details

Epitaxial $Pb(Zr_{0.45},Ti_{0.55})O_3$ (PZT) thin film capacitors with Pt and SRO top electrodes were prepared for the polarization fatigue experiments. The detailed sample preparation and synchrotron x-ray microdiffraction setup were described in Chapter 3.

The evolution of polarization domains during the development of fatigue over the course of many cycles of the applied electric field was investigated using synchrotron x-ray microdiffraction. After applying a series of electric field cycles, we acquired polarization-electric field hysteresis loops and images of polarization domains in the two remnant polarization states. We compared the remnant polarization and the intensity of images taken in the two opposite polarization states at the same number of switching cycles. The procedure is shown schematically in Fig. 4.1.

In order to induce fatigue, bipolar triangular voltage pulses were applied to the bottom electrode of the PZT capacitors. The hysteresis loops were measured using the same electric field wave forms used in the fatigue test. In order to ensure complete polarization switching during the electric field cycles used to induce fatigue, the amplitude

of the applied voltage pulses was chosen to be higher than coercive voltage, 2.2 and -2.2 V. The values of the remnant polarization and the coercive voltages were measured from the hysteresis loops and plotted as a function of the accumulated number of switching cycles applied to the device. The amplitude and frequency of the triangular wave pulses were different for each series of experiments. The specifics are given in the following text.

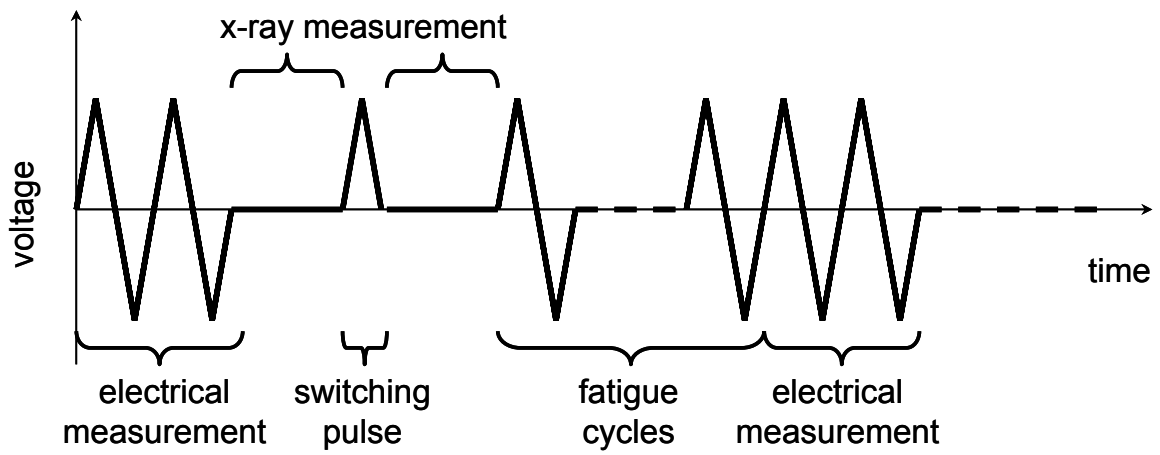

Figure 4.1 A series of applied electric pulses during the experiments.

Area maps of the intensity of the PZT (002) reflection in the two remnant polarization states were acquired after each pause in the fatigue process. The scans covered areas of 100×100 μm^2. The time required for each image was approximately 30 min. In order to compensate for long-term changes in the intensity of the incident x-ray beam, the diffracted intensity in the area maps was normalized to the flux of incoming x-rays measured by an ionization chamber detector. Area maps were then normalized with respect to each other using the average intensity in the region of the maps outside the top electrode.

We expected that there would be no change in the intensity of the PZT (002) reflection in the region outside the top electrode during the experiments.

4.3 Results and discussion

The x-ray microdiffraction measurements allowed us to study polarization fatigue in PZT thin film capacitors by comparing the difference in the intensity of the PZT (002) reflections in complementary pairs of images. We compared electrical measurements of the switchable polarization with our structural investigations.

4.3.1 Polarization fatigue in PZT thin films with Pt top electrodes

Polarization fatigue in the PZT film capacitors with the Pt top electrodes occurred differently in two regimes depending on the magnitude of the applied electric fields. We investigated polarization fatigue at electric fields of 625 kV cm^{-1} and 1.2 MV cm^{-1}. Since our devices had a complete capacitor structure consisting of ferroelectric thin films with top and bottom electrodes, it was possible to apply such high electric field uniformly through the devices and to study fatigue effect in operating devices.

4.3.1.1 Low electric field

The low electric field regime of the polarization fatigue phenomenon was investigated using electric fields of 625 kV cm^{-1}. Thin films with Pt top electrodes and PZT with thickness of 1600Å were used for these studies. The electrical pulses had a frequency of 1 kHz amplitudes of ±10 V. After 10, 10^3, 5×10^3, 10^4, and 5×10^4 switching

cycles, we made electrical measurements of the hysteresis loop and x-ray microdiffraction images of the polarization state.

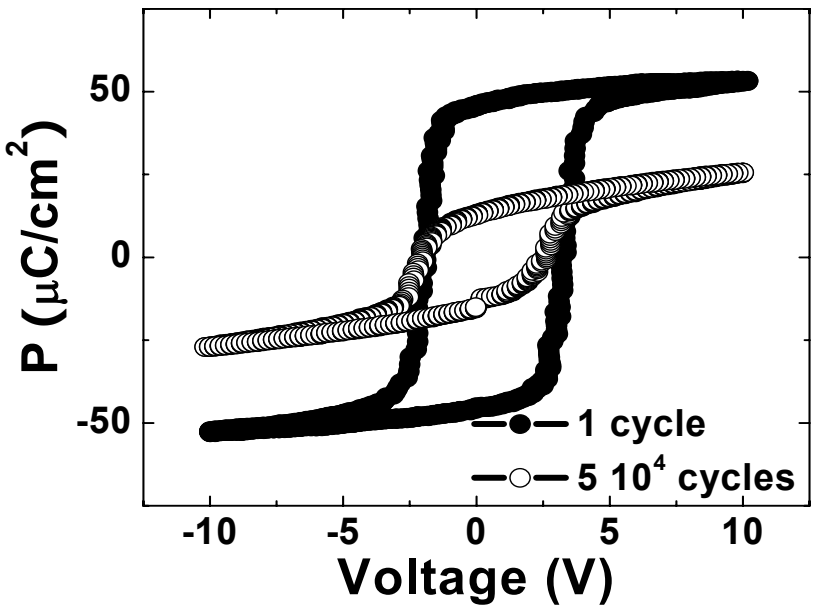

Figure 4.2 Polarization-electric field hysteresis loops acquired before and after fatigue in a PZT capacitor with Pt electrode. The magnitude of the applied electric field was 625 kV cm^{-1}.

Figure 4.2 shows polarization-electric field hysteresis loops measured after each set of polarization switching cycles. The initial value of remnant polarization was 46 μC cm^{-2}. The values of the coercive voltage were 3.2 and -1.9 V for positive and negative voltages, respectively. The remnant polarization of the PZT capacitor began to decease after 10^3 switching cycles, and the remnant polarization reached 13 μC cm^{-2} after 5×10^4 switching cycles. After 5×10^4 switching cycles, the coercive voltages were 2.6 and -2.0 V for

positive and negative voltages, respectively. The hysteresis loop measured at this switching cycles showed still sharp transition near the coercive voltages. Fatigue at these electric fields occurred without significant changes in coercive voltages and without leakage current.

Pairs of images were acquired using x-ray microdiffraction in the remnant polarization states following positive and negative 10 V pulses. Figure 4.3 shows the pairs of images of the intensity of the PZT (002) reflection following positive and negative voltage pulses at the same series of steps in the total number of switching cycles. The images were taken in identical regions of the PZT capacitor. The area covers the edge of the 200 μm-diameter top electrode and includes regions inside and outside the device. The edge of the device appears as an arc across the top of these images. The color scale in the images corresponds to the intensity of the diffracted x-ray beam. Red indicates higher intensity than green.

The difference in the average intensity of the PZT (002) x-ray reflection in the capacitor was measured at each number of switching cycles and compared to the remnant polarization measured electrically (Fig. 4.4). In order to calculate the average intensity in the images, we integrated the intensity in the region inside the device (50×50 μm^2), and normalized by dividing the area of the region. The intensity calculated in this way was compared between images in each pair of images. Electrical measurements showed that there was no polarization fatigue until 10^3 switching cycles. However, x-ray observation

showed that the difference in intensity between the two remnant polarization states at 10 cycles was 15% and increased to 20% at 10^3 cycles.

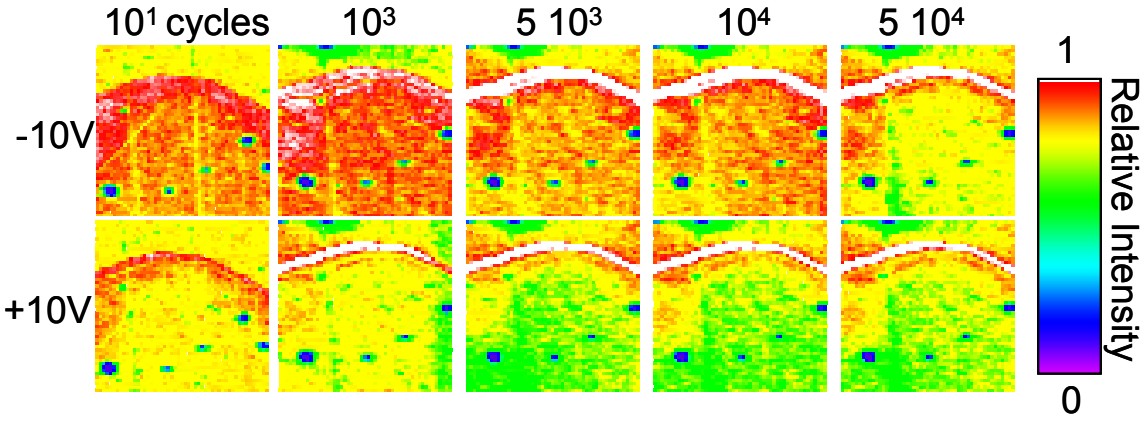

Figure 4.3 The evolution of x-ray microdiffraction images during the polarization fatigue process in a 1600 Å thick PZT film with Pt top electrodes. Each image was taken in the remnant polarization state after applying negative and positive 10 V pulses, respectively. The area of each image is 100×100 μm^2.

The observed intensity difference of 15% in the unfatigued stage is smaller than what we expected. In the previous chapter, we demonstrated that two opposite polarization states can be distinguished by comparing the intensities and showed that the difference in the intensities of the two polarization states was 30%. However, the intensity difference between two remnant polarization states from the first pair of images in Fig. 4.3 did not show 30% difference. The origin of the reduced intensity difference in the unfatigued stage is still unclear. As fatigue developed, the difference in intensity significantly decreased. Eventually the intensity difference was 6% after 5×10^4 switching cycles.

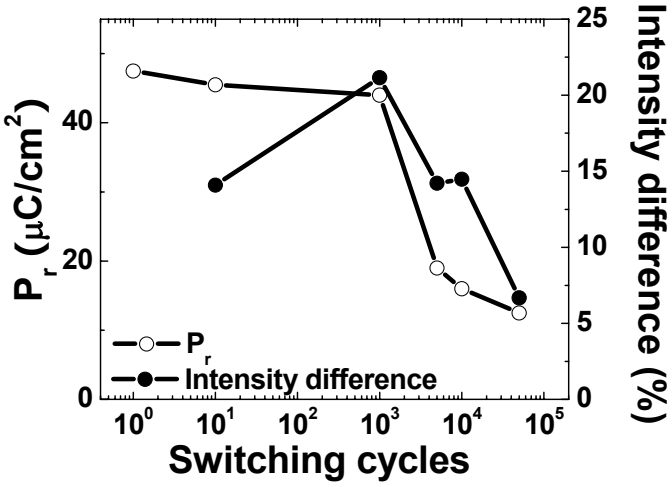

Figure 4.4 Remnant polarization and the normalized difference in the average intensity of images of the two polarization states of the PZT capacitor with Pt top electrodes as a function of the number of cycles of the applied electric field.

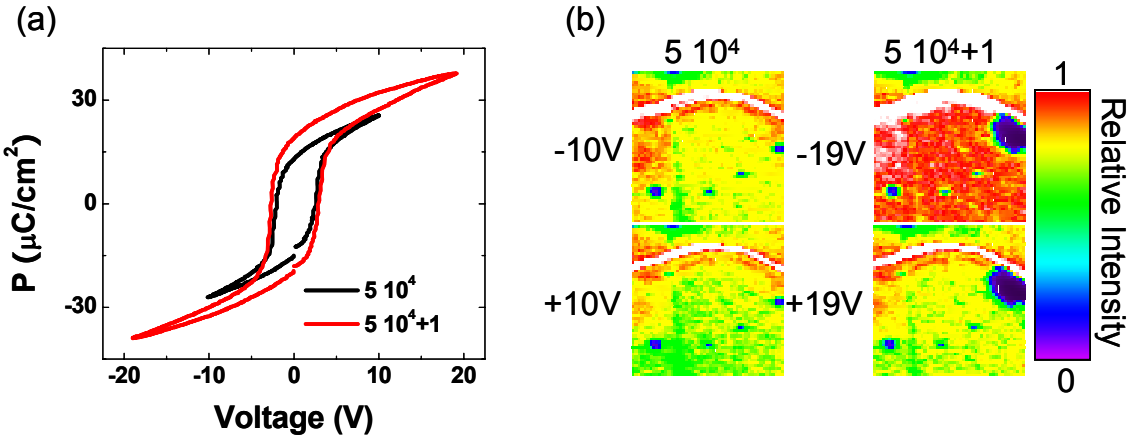

Figure 4.5 (a) Polarization-electric field hysteresis loops before and after applying a higher electric field and (b) corresponding x-ray microdiffraction images. The area of each image is 100×100 μm^2.

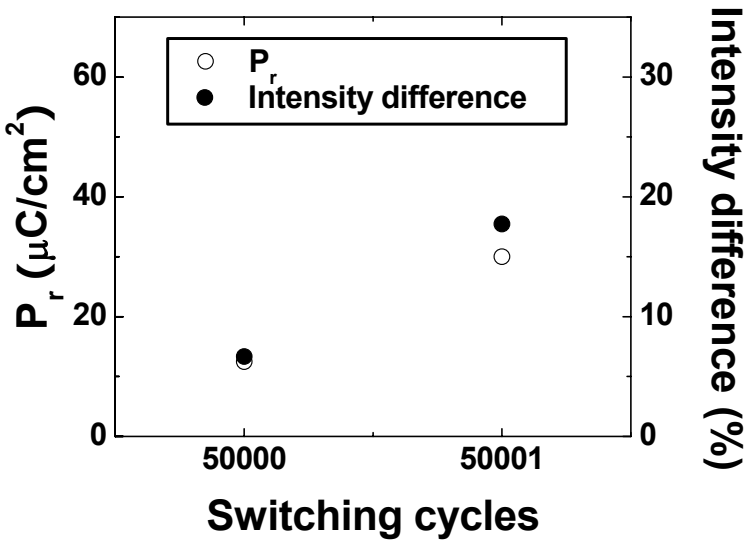

Figure 4.6 Remnant polarization and normalized intensity difference between the two polarization states before and after applying a higher electric field.

Applying an electric field higher than the electric field used in fatigue process restored the remnant polarization and the intensity difference. Higher electric field may lead to depinning effect in pinned domain walls or may overcome an internal bias field.[80,81] After 5×10^4 switching cycles, a higher electric field with the same frequency was applied to the fatigued device. The electric field was 1.1 MV cm^{-1}. Figure 4.5 (a) shows the hysteresis loop with the higher electric field and a comparison to the loop measured after 5×10^4 switching cycles. After applying the higher voltage pulse, the remnant polarization was 30 μC cm^{-2} which is higher than the values of 13 μC cm^{-2} observed after 5×10^4 switching cycles. The values of coercive voltage were 2.9 and -2.7 V for positive and negative voltages, respectively. The coercive voltages were approximately the same as

those at 5×10^4 cycles. Applying the higher electric field also produced a change in x-ray measurements (Fig. 4.5 (b)). The intensity difference was increased by applying the higher electric field. The remnant polarization and intensity difference were shown in Fig. 4.6. Some areas with a very low diffracted intensity appeared after applying the higher voltage pulses. This is the origin of fatigue at high electric field and is described in the next section.

The electrical measurements of our PZT thin film capacitors with Pt electrode showed that the polarization degradation was affected only by the number of switching cycles but not by the frequency (Fig. 4.7).

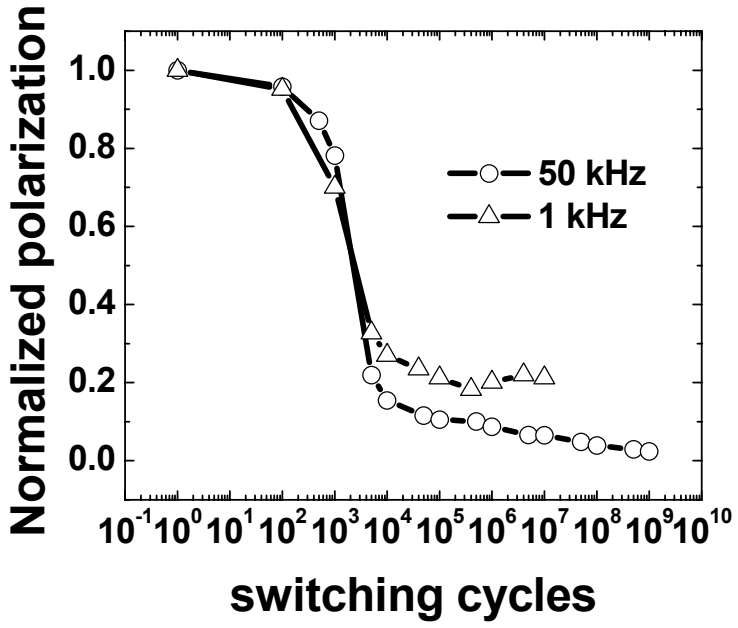

Figure 4.7 Normalized switchable polarization as a function of switching cycles in PZT capacitors at different frequencies of pulses.

4.3.1.2 High electric field

In order to study fatigue under the electric fields near the device breakdown field, we performed x-ray microdiffraction studies under a high electric field. Polarization fatigue experiments at high electric field were performed with an 800 Å thick PZT film with Pt top electrodes. In this case, the electrical pulses used were again ±10 V pulses with the frequency of 1 kHz. The amplitude of the applied electric field was 1.2 MV cm^{-1}. This field is just below the breakdown electric field in PZT. The breakdown electric field in ferroelectric materials depends on the thickness of the ferroelectric material, electrodes and other factors.[82]

Electrical measurements and x-ray microdiffraction observations were performed after 10, 5×10^4, 10^5, 2×10^5, and 3×10^5 switching cycles. Polarization-electric field hysteresis loops before and after fatigue are shown in Fig. 4.8 (a). Before the fatigue, the value of remnant polarization was 47 μC cm^{-1} and the values of positive and negative coercive voltages were 2.2 and -2.2 V, respectively. Fatigue occurred after 10^4 switching cycles. Unlike the fatigue at low electric field, the fatigue process at high fields was accompanied by the development of leakage currents. It was thus difficult to compare the coercive voltages before and after fatigue. In order to calculate the remnant polarization in the electrical hysteresis loops after fatigue, we subtracted an amount of leakage current from the current acquired from electrical measurements. A sharp signal associated with the switching current was obtained by subtracting the leakage current (Fig. 4.8 (b)). This

signal was used to calculate a polarization-electric field hysteresis loop, which was then used to measure the remnant polarization.

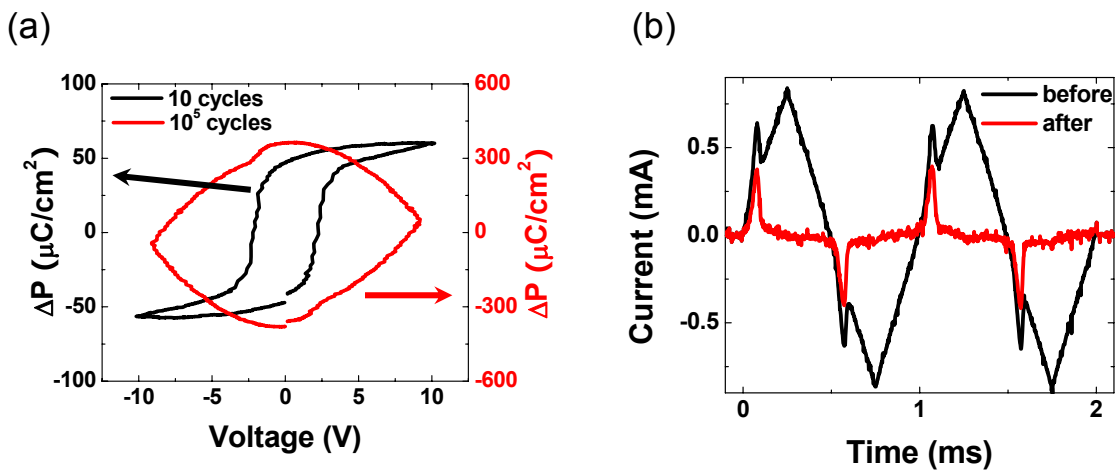

Figure 4.8 (a) Polarization-electric field hysteresis loops acquired before and after fatigue at high electric field and (b) switching current before and after subtracting leakage current.

Images of the evolution of the intensity of PZT (002) reflections during the polarization fatigue process at high electric fields are shown in Fig. 4.9. The images showed that until 10^5 switching cycles the intensity difference between two opposite polarization states only gradually decreased.

Figure 4.10 shows the high resolution x-ray images acquired after 10^5 switching cycles. The images show that there is coexistence of switchable (dashed circles in Fig. 4.10) and nonswitchable (solid circles in Fig. 4.10) domains. The nonswitchable domains are divided by two distinguished regions; one is the region with high intensity (shown in yellow in Fig. 4.10) and the other is the region with low intensity (shown in green in Fig.

4.10). These x-ray results suggest that the nonswitchable domains do not have a preferential polarization direction and distribute randomly through the device. Those regions do not respond to the external electric field, which leads the suppression of switchable polarization.

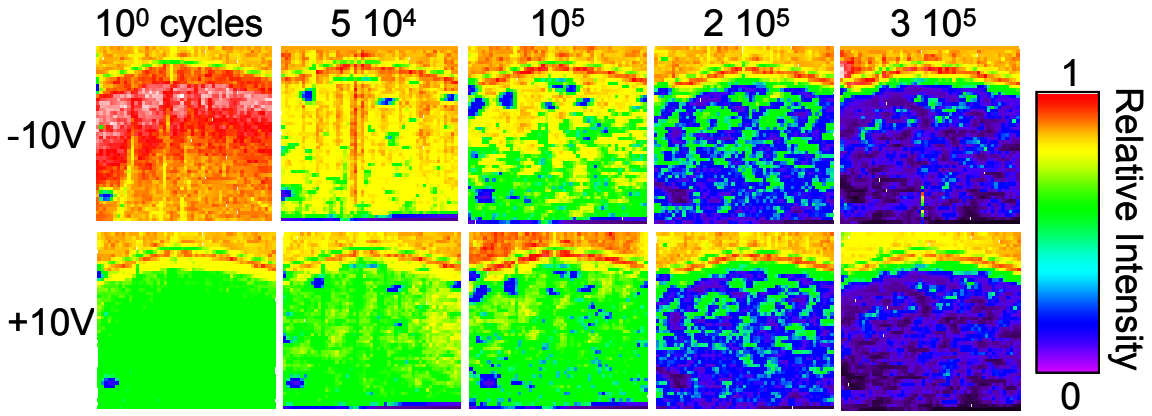

Figure 4.9 The evolution of x-ray microdiffraction images during the high-electric-field fatigue process in the 800 Å thick PZT film with the Pt top electrode. Each image was taken at the remnant polarization state after applying negative and positive 10 V pulses, respectively. The area of each image is 100×100 μm^2.

Applying switching cycles beyond 10^5 cycles produced large differences in the intensity maps compared to the low electric field case described in the previous section. Regions with very low intensities (shown in blue in Fig. 4.9) were formed in the device after 5×10^4 switching cycles. These regions began to merge after 10^5 cycles and eventually covered the whole device.

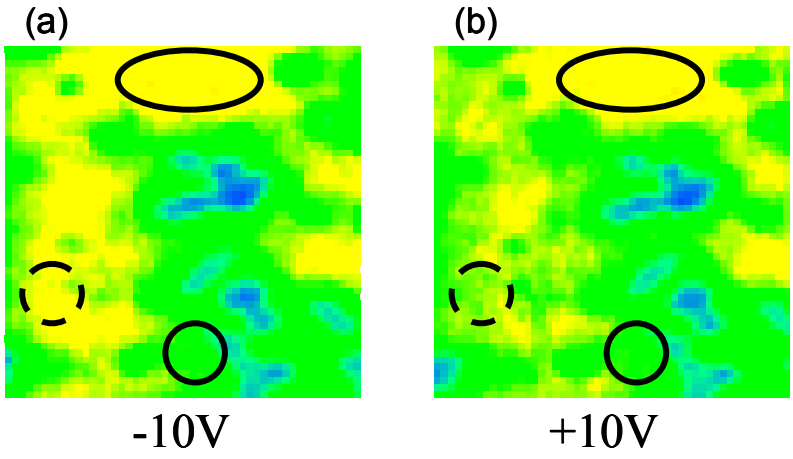

Figure 4.10 X-ray maps taken in two remnant polarization states after 10^5 switching cycles: (a) after applying negative 10 V to the bottom electrode and (b) applying positive 10 V to the bottom electrode. Switchable domains (dashed circles) and nonswitchable domains (solid circles) are shown in the maps. The area of each image is 20×20 μm^2.

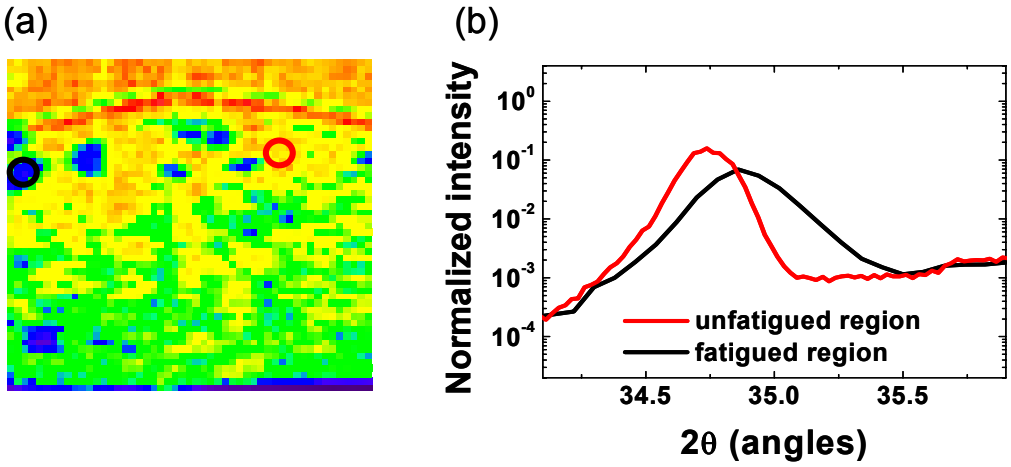

Figure 4.11 (a) An intensity map acquired after 10^5 switching cycles. (b) PZT (002) reflections taken in unfatigued (red circle) and fatigued (black circle) regions. In (b), the peak intensities of SRO reflection were normalized to compare the intensity and peak position of PZT (002) reflections. The area of each image is 100×100 μm^2.

The structure of the PZT thin film in the regions with low intensity was probed by making θ-2θ scans across the PZT (002) Bragg reflection. In these regions, the peak position of PZT (002) Bragg reflection was shifted to higher angle and the width of the reflection was broader (Fig. 4.11). The c-axis lattice constant of PZT was 4.167 Å before the fatigue. However, the low intensity regions were almost fully relaxed and had the lattice constant of 4.152 Å, close to the bulk value in PZT.

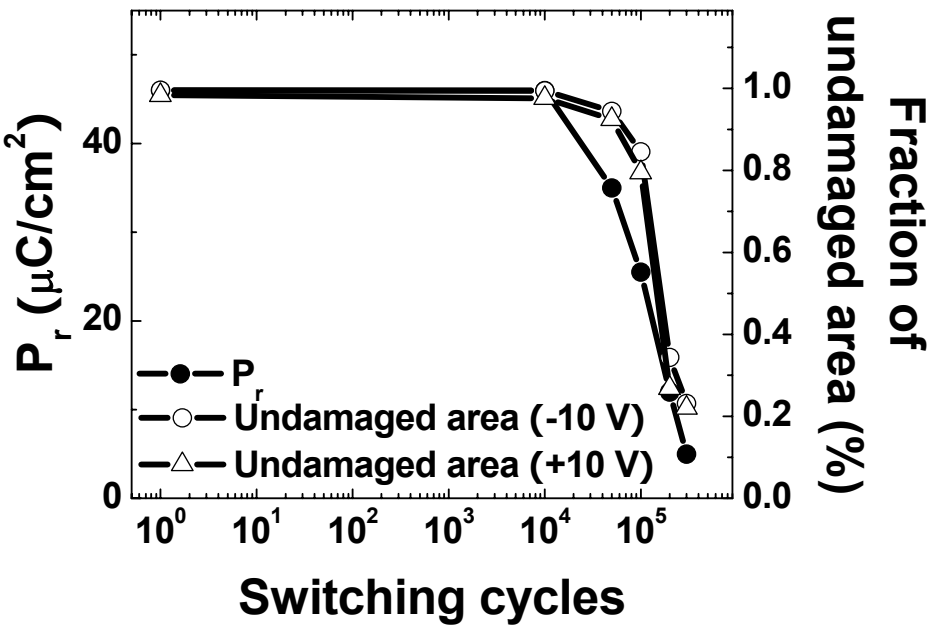

Figure 4.12 The remnant polarization and the undamaged fraction of the image in the two polarization states at high electric fields.

Figure 4.12 compares the remnant polarization and the fraction of areas with low intensity. The area fraction of the regions with low intensity in the images of Fig. 4.9 was

estimated by counting the number of pixels in the unfatigued regions and dividing by the total number of pixels for the whole device. As polarization fatigue develops, the fraction of the area that exhibits the decrease in intensity rapidly increases. The area fraction of the reduced diffracted intensity was almost the same in the two remnant polarization states at each number of switching cycles.

4.3.2 Polarization fatigue in PZT thin films with SRO top electrodes

Polarization fatigue in PZT thin films can be prevented by using conducting oxide electrodes rather than metal electrodes. In order to understand the effect of the chemical composition of the electrodes on the domain phenomena related to fatigue, we investigated the fatigue effect in PZT thin film capacitors with SRO top and bottom electrodes using x-ray microdiffraction.

Electrical measurements and x-ray microdiffraction observations were performed on a 1600 Å thick PZT film with SRO top and bottom electrodes. The electrical pulses had a frequency of 0.1 kHz and amplitude of ±5 V. After 10, 5×10^3, 10^4, 5×10^4, and 10^5 switching cycles, electrical and x-ray microdiffraction measurements were performed. Electrical experiments with larger numbers of switching cycles, up to 10^7 cycles, were performed after the x-ray study.

Figure 4.13 shows images of the intensity of the PZT (002) x-ray reflection at various numbers of switching cycles. Each pair of x-ray images was taken in the remnant polarization state reached after applying negative and positive 5 V pulses, respectively.

The difference in the average intensities of the pairs of x-ray images at the same number of switching cycles are plotted in Fig. 4.14. After 10 switching cycles, the intensity difference was 32%. After 10^5 switching cycles the intensity difference was 24%

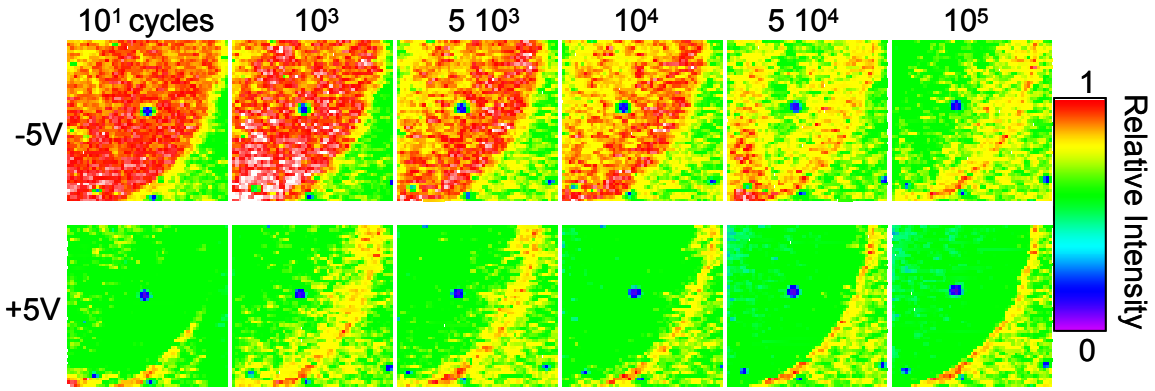

Figure 4.13 X-ray microdiffraction images of the 1600 Å thick PZT film with SRO top electrodes at up to 10^5 total cycles of the applied electric field. The area of each image is 100×100 μm^2.

In fresh devices, the values of switchable remnant polarization and the normalized difference in the intensity of the ±5 V x-ray microdiffraction images were 54 $\mu C\ cm^{-2}$ and 32%, respectively. These values did not change significantly during the entire course of the experiment. After 10^5 switching cycles, the values were 47 $\mu C\ cm^{-2}$ and 24%. Even for these small changes in the electrical behavior of the thin film, the x-ray microdiffraction images reflected the polarization state of the capacitor. The difference in the intensity of the two remnant polarization states at each number of switching cycles was nearly proportional to remnant polarization measured electrically (Fig. 4.14).

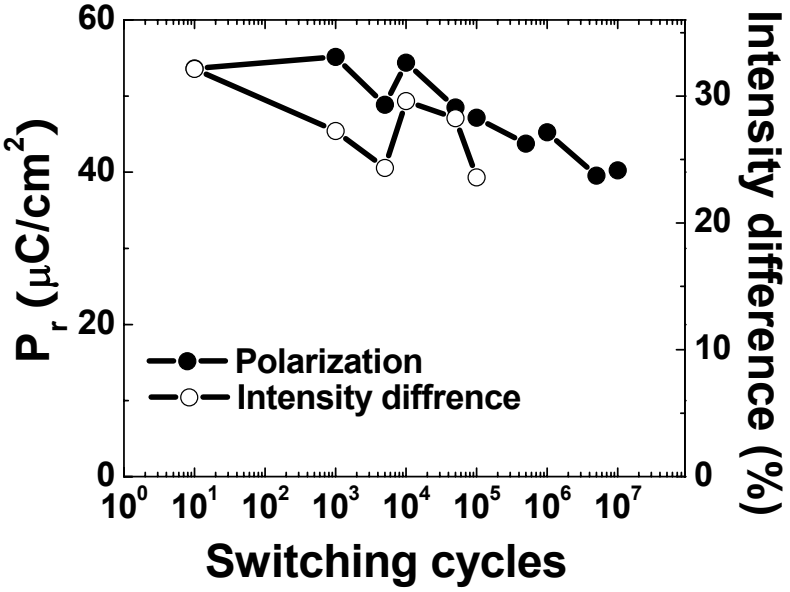

Figure 4.14 Switchable polarization and the average difference in intensity between the two polarization states of an SRO/PZT/SRO thin film capacitor as a function of the number of cycles of the applied electric field.

A slight degradation of the remnant polarization in the electrical measurement and intensity difference in the x-ray measurement began after 10^4 switching cycles. The eventual reduction in remnant polarization is due to the degradation of the SRO top electrode. Optical microscopy and scanning electron microscopy images showed that in some regions the PZT layer was visible in the device after 10^7 switching cycles, and that the SRO electrode had delaminated in these areas. We thus consider that the weak SRO top electrode was partially destroyed after 10^4 cycles, at a scale smaller than the x-ray beam. The decrease of the average remnant polarization and intensity difference might be due to a reduction of the effective area of the device.

Beyond this slight change in the electrodes, PZT thin film capacitors with SRO electrodes showed no significant fatigue effect in up to 10^7 switching cycles and we could distinguish two opposite polarization states by comparing the intensities of the images.

4.3.3 Discussion

In PZT thin film capacitors with Pt electrodes, the degradation of switchable polarization depends on the number of switching cycles. Under various conditions, fatigue occurs between 10^2 and 10^7 switching cycles.[5,20,21]

As briefly discussed in Chapter 1, polarization fatigue is commonly thought to occur by two major mechanisms. In the first, fatigue is due to the inhibition of the nucleation of opposite polarization domains at the interface between the electrodes and the film.[28] In the second, fatigue is considered to be a process of domain wall pinning by defects such as oxygen vacancies.[29] Our fatigued devices consisted of PZT with SRO bottom electrodes and Pt top electrodes. If the nucleation inhibition mechanism is the origin of fatigue, then the interface between PZT film layers and Pt electrode layers is particularly important. During the fatigue process, the nucleation and growth of opposite polarization domains under bipolar voltage pulses are inhibited at the interface of film and electrodes.[28] The PZT/Pt interface causes the fatigue effect while PZT/SRO interface does not. Our x-ray microdiffraction results at low electric fields (Fig. 4.3) showed that, as fatigue developed, the polarization state with lower intensity was more stable than the polarization state with high intensity. Consequently, under the fatigue cycles, the

polarization domains were gradually pinned in the polarization state appearing after applying positive voltage pulses to the SRO bottom electrode.

The structural effects associated with fatigue induced by applying electric fields near the breakdown field suggests that the origin of the fatigue at high field is different compared to that at low field. The first step of fatigue mechanism is similar to the low field case. Nonswitchable domains lead to the suppression of switchable polarization. With further cycles, however, the x-ray study revealed that fatigue occurred with the structural modification in the PZT film. In fatigued regions, strained PZT films are fully relaxed and have a lattice constant that is the same as bulk.

By replacing the Pt top electrodes with the SRO electrodes in the PZT thin film capacitors, polarization fatigue was not observed up to 10^7 switching cycles. This result agrees with previous observations that oxygen vacancies are important in fatigue mechanisms.[5]

4.4 Conclusion

We investigated polarization switching and the development of polarization fatigue in epitaxial PZT thin film capacitors with Pt and SRO top electrodes using x-ray microdiffraction. We compared the microdiffraction observation to results of electrical measurements. Both x-ray and electrical observations show that there is rapid degradation after comparatively few switching cycles in the capacitors with the Pt top electrodes, while the capacitor with the SRO electrodes exhibits minimal degradation in the switching.

In the PZT films with the Pt electrodes, the origin of fatigue is mainly due to the formation of the nonswitchable domains caused by either the domain wall pinning or the nucleation inhibition. In this case, the switching polarization can be restored by applying the higher electric field than that for the fatigue test. Applying the high field leads to the structural change in the PZT film capacitor which is another origin of a fatigue mechanism.

X-ray microdifraction is a useful tool to investigate properties of ferroelectric capacitors, including polarization switching and polarization. Also piezoelectric response in ferroelectric thin films can be measured precisely. In next chapter we will discuss the piezoelectric effect in PZT thin film capacitors.

Chapter 5 Piezoelectricity in PZT Thin Films

5.1 Introduction

All ferroelectric materials are piezoelectric. Piezoelectricity is the coupling between the mechanical and electrical properties of a material. When a stress is applied to piezoelectric materials, an electrical polarization is induced.[40] This is called the direct piezoelectric effect and it is reversible. When an electric field is applied, a structural deformation called converse piezoelectric effect occurs.[40] The piezoelectric response in ferroelectric materials can be thought of as having contributions from both intrinsic and extrinsic sources. The intrinsic contribution originates from the lattice expansion and contraction in individual unit cells. The extrinsic contribution is mainly due to domain wall motion or phase transitions. The total piezoelectric response is the sum of the two contributions.

The extrinsic contribution to the piezoelectric response has been intensively studied since it can lead to a dramatic increase in the piezoelectric response of a sample containing a large number of domains. In tetragonal PZT thin films, for example, the movement of 90° domain walls in an electric field has been observed.[58,83] This domain wall movement, consequently, leads to a high piezoelectric coefficient.[54,58] Similarly, in relaxor-based ferroelectric single crystals, an electric field can alter the structure of crystals between tetragonal and rhombohedral phase, resulting in a large enhancement of the piezoelectric coefficient.[55] Since these contributions are linked to a change in the structure of the

ferroelectric material, the investigation of the structural response to an external electric field is fundamentally useful in understanding piezoelectricity.

Ferroelectric thin films are conventionally deposited on a rigid thick single crystal substrate. Since the in-plane lattice parameters of the thin films are constrained by the substrate, the piezoelectric coefficients in films are much less than those observed in bulk materials.[59] The effective longitudinal piezoelectric coefficient of these clamped piezoelectric thin films is $d_{33}^{eff} = d_{33} - \frac{2d_{31}s_{13}^{F}}{s_{11}^{F} + s_{12}^{F}}$, where d_{33} and d_{31} are the longitudinal and transverse piezoelectric coefficients of the bulk material, and s_{ij}^{F} are the elastic compliances of the films at constant electric field.[40] The equation above is correct when there is no elastic deformation in the substrate, implying no change in the strain parallel to the surface direction. The measured piezoelectric coefficient only depends on the elastic properties of the film in this case.

If a substrate is not perfectly rigid, one should consider the contribution of the elastic deformation and bending of the substrate to the piezoelectric response. It has been shown that piezoelectric coefficients in thin films depend on the elastic properties of the substrate.[84,85] With the contribution due to the deformation of the substrate, the effective piezoelectric coefficient is $d_{33}^{eff} = d_{33} - \frac{2d_{31}s_{13}^{F}}{s_{11}^{F} + s_{12}^{F}} + \frac{2d_{31}s_{13}^{S}}{s_{11}^{S} + s_{12}^{S}}$, where the last term is the contribution due to the elastic deformation of the substrate.[6] The clamping effect is

compensated and the effective piezoelectric coefficient is the same as bulk if the elastic compliances of the film and the substrate are the same.

The bending of the substrate also leads to a deflection that contributes to the piezoelectric response of thin films.[85,86] In order to eliminate the artifacts due to the complicated bending and substrate deformation effects, it is useful to measure strains in the thin film and the substrate separately.

A variety of techniques have been developed and used to study the piezoelectricity of ferroelectric films. Most of the reported values of the piezoelectric coefficient for ferroelectric thin films have been found using the converse piezoelectric effect. Interferometry[46,87] and piezoelectric force microscopy (PFM)[49] measure the piezoelectric coefficient by measuring the changes in the thickness of the sample.

X-ray diffraction has been used to measure the piezoelectric response in ferroelectric ceramics and films.[51] In this approach, the piezoelectric coefficient can be determined by measuring the deformation of the ferroelectric unit cell, which leads to shifts of x-ray Bragg reflections in reciprocal space. This structural information is fundamentally useful in understanding piezoelectricity in ferroelectric materials. The use of continuous well-defined electrodes in x-ray studies allows measurements under homogeneous electric field conditions.

This chapter describes our study of piezoelectricity in PZT thin film capacitors using x-ray microdiffraction. We show precise measurements of the piezoelectric response

in the PZT film capacitors using time-resolved x-ray microdiffraction. We also discuss measurements of the transverse piezoelectric response in PZT thin films.

5.2 Experimental details

Our samples for the piezoelectric studies were epitaxial (001) $Pb(Zr_{0.45}Ti_{0.55})O_3$ films with the thicknesses of 3000 and 4000 Å. The PZT thin films were grown on a (001) $SrTiO_3$ single crystal. The detailed film preparation and the structure of the PZT thin film capacitor were discussed in Chapter 3. In order to avoid the polarization fatigue effect, $SrRuO_3$ bottom and top electrodes were used for these measurements.

The longitudinal and transverse piezoelectric coefficients in the PZT thin films were measured using time-resolved synchrotron x-ray microdiffraction at sectors 7 and 2 at the Advanced Photon Source. The experimental setup at the two beam lines was almost identical (see Chapter 2). In each case, a focused x-ray beam of 100 nm in a focused spot size was produced using a Fresnel zone plate x-ray focusing optics. Electrical contact to the top electrode was maintained during the diffraction experiments using a 25 μm-diameter Pt wire spring.

In order to measure the longitudinal piezoelectric coefficient, we made θ-2θ scans near the PZT (002) Bragg reflection using a 10 keV x-ray at sector 7. These scans measured the lattice constant of the PZT film in the direction along the surface normal. During the θ-2θ scans, 18 cycles of a triangular voltage pulse were applied at each angular

step. The c-axis lattice spacing of the PZT thin film was measured with a sensitivity of approximately $\Delta c/c \sim 10^{-5}$.

The diffracted x-rays were collected using an avalanche photodiode (APD) detector. The two polarization states were distinguished by measuring the change in the intensity of the Bragg reflection. In our case, there was a 30% difference in intensity between two polarization states as explained in Chapter 3.

The schematic timing diagram used in the experiments is shown in Fig. 5.1. A multichannel scaler (MCS) connected to the APD was used to record the intensity of diffracted beams as a function of time. The MCS accumulates counts into a number of counting channels. We chose the dwell time per channel to be 10 or 20 μs, depending on the duration of the electrical pulse we applied to the sample. In order to achieve reasonable counting statistics, the intensity was measured during 18 cycles of the applied electric field pulses and the intensities at equal times relative to the beginning of each pulse were averaged. The reciprocal space position of peak intensity of the PZT (002) Bragg reflection was used to calculate the change in the lattice constant caused by the converse piezoelectric effect. The peak intensity was 1.7×10^{6} counts per second.

To measure the transverse piezoelectric coefficient, reciprocal space maps of PZT (103) reflection were acquired with an 11 keV x-ray beam at station 2ID. In this case, a dwell time of 200 μs per channel with an electrical pulse of 50 Hz was used. The APD detector and MCS were used in the same manner described above.

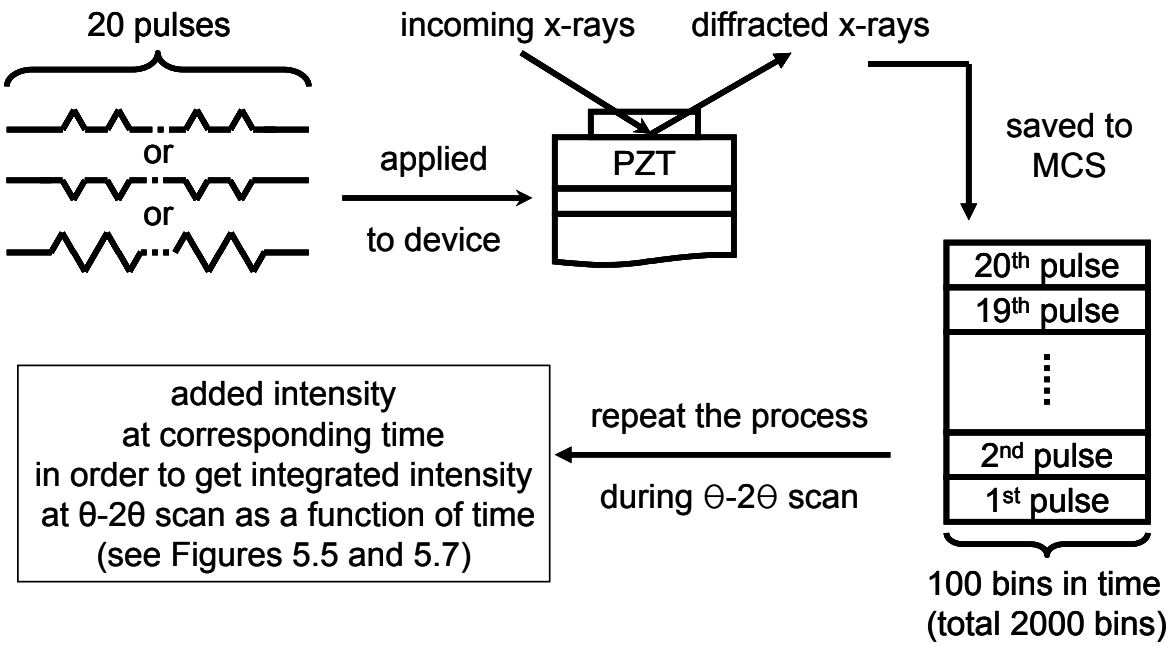

Figure 5.1 Procedure of measuring piezoelectric coefficients using x-ray microdiffraction.

5.3 Results and discussion

5.3.1 Structure of PZT thin films

In order to determine the crystal structure and lattice parameters of the PZT samples, reciprocal space maps of the intensity of the x-ray scattering were made by measuring the intensity of diffracted x-rays on mesh scans of PZT (114) reflections. The geometry of x-ray reflections is shown in Fig. 5.2.

In-plane and out-of plane lattice parameters can be calculated from the ω and 2θ angles at which the maximum intensity is found in reciprocal space maps.[88] In a tetragonal

structure, the a-axis lattice constant is $a = \frac{\sqrt{h^2 + k^2}}{Q_x}$ and the c-axis is $c = \frac{l}{Q_z}$. The reciprocal space vectors Q_x and Q_z can be calculated using the ω and 2θ angles in reciprocal space maps. $Q_x = \frac{\cos\omega - \cos(2\theta - \omega)}{\lambda}$ and $Q_z = \frac{\sin\omega + \sin(2\theta - \omega)}{\lambda}$, where λ is the wavelength of incident x-rays.[88]

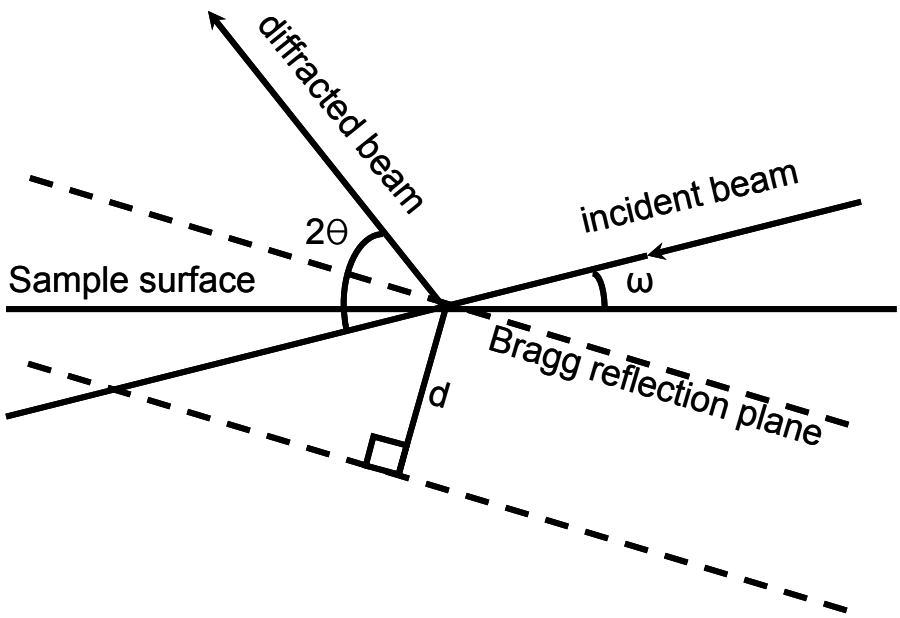

Figure 5.2 Schematic diagram showing the x-ray reflection geometry. ω is the angle between incident beam and sample surface, and 2θ is the angle between incident and diffracted beam.

Figure 5.3 shows reciprocal space maps of the PZT (114) reflection measured using a laboratory x-ray source (λ=1.5406 Å). The angles in the maps were corrected with respect to the STO substrate. Since the substrate was relatively thick (500 μm) and the

lattice parameter, 3.905 Å in the cubic phase, was well known, we used the peak position of the STO (114) reflection as a standard.

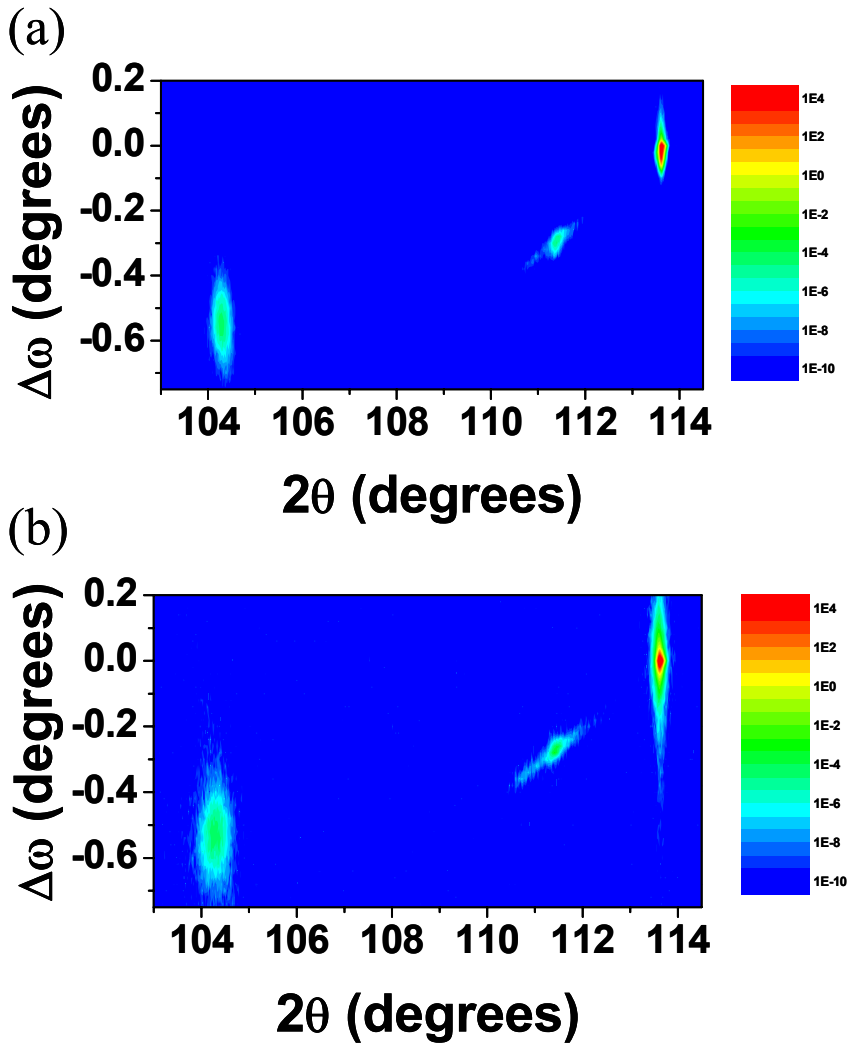

Figure 5.3 Reciprocal space maps of the (114) reflection of PZT films with thicknesses of (a) 3000 and (b) 4000 Å. The Δω is the difference in angles with respect to the ω angle of a STO substrate, 19.47˚.

The lattice constants of the samples are summarized in Table 5.1. The lattice constants of bulk PZT at the same nominal composition as our thin films are 4.021 and 4.148 Å for the a- and c-axis, respectively.[19] The differences in the constants of the bulk and the 4000 Å thick PZT film are 0.35 and 0.1% for a-axis and c-axis lattice constant, respectively, which indicates that the PZT films are nearly fully relaxed. The in-plane lattice constant of the SRO is 3.900 Å which is almost equal to the STO lattice constant. The SRO bottom electrode is thus coherently grown on the STO substrate.

Table 5.1 Lattice constants of PZT, SRO, and STO, based on the x-ray diffraction measurements shown in Fig. 5.3.

	$Pb(Zr_{0.45}Ti_{0.55})O_3$		SRO	STO
	3000 Å	4000 Å		
a-axis	4.032 Å	4.035 Å	3.900 Å	3.905 Å
c-axis	4.152 Å	4.152 Å	3.963 Å	3.905 Å

5.3.2 Precise measurements of the piezoelectric distortion

The piezoelectric response in the 4000 Å thick PZT thin films was measured using the converse piezoelectric effect. Applying an electric field to the PZT thin films produces a distortion of the lattice. Whether the lattice expands or contracts depends on the relative directions of the electric field and the spontaneous polarization. When the electric field is parallel to the polarization the unit cell expands. The unit cell contracts when the

polarization and electric field are antiparallel (Fig. 5.4). The piezoelectric distortion shifts the Bragg reflections of the PZT thin film in x-ray diffraction experiments. Lattice expansion leads to a shift of the PZT (002) Bragg reflection to a lower 2θ angle. A shift to higher angle occurs when the lattice contracts. The values of the shifts can be used to measure the longitudinal piezoelectric coefficient (d_{33}) using $d_{33} = \left(\frac{\partial S_3}{\partial E_3}\right)$, where S_3 is the strain and E_3 is the electric field along the surface normal.

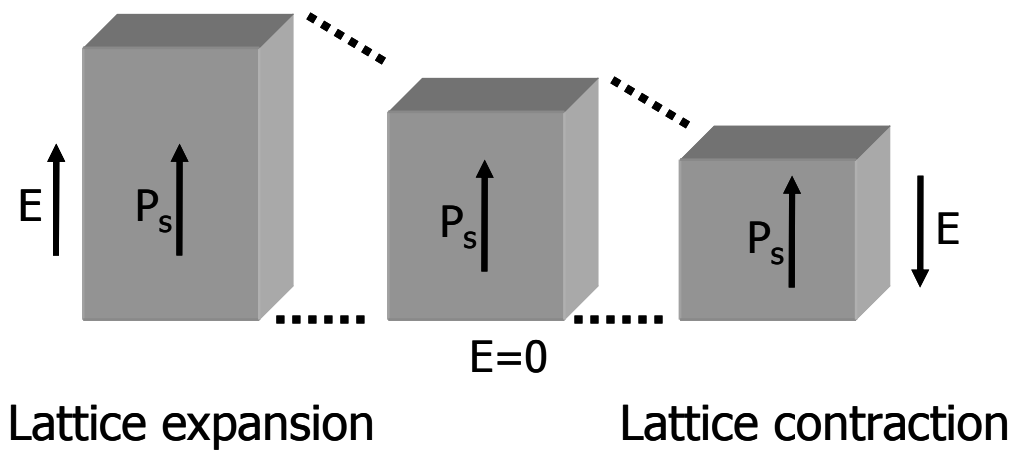

Figure 5.4 Schematic diagram of lattice distortion under an external electric field. The lattice expansion and contraction are determined by the relative directions of an electric field (E) and polarization (P_s).

The longitudinal piezoelectric distortion was measured using the PZT (002) Bragg reflection. In order to avoid a contribution to the piezoelectric response from polarization switching, we first measured the lattice constant change under electric fields of one sign. This configuration does not lead to polarization switching but rather to a pure lattice expansion. Before the measurements, the capacitor was poled by applying an electric field

pulse higher than the coercive field so that the direction of the polarization vector was parallel to the applied electric field.

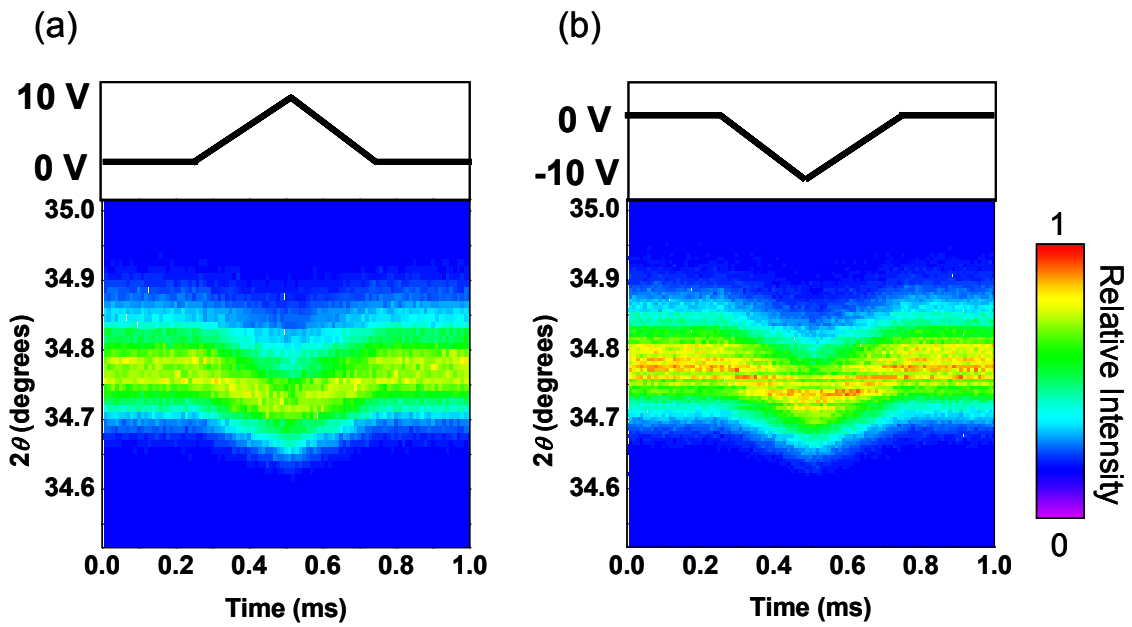

Figure 5.5 The intensity recorded in a θ-2θ scan around the PZT (002) Bragg reflection as a function of time during (a) positive 10 V pulses and (b) negative 10 V pulses. The amplitude and the shape of voltage pulses are shown above the intensity maps.

Figure 5.5 (a) and (b) show that the lattice constant changes during triangular positive and negative 10 V pulses, respectively. The shift of the PZT (002) Bragg reflection angle was measured while applying the unipolar pulses with 500 μs duration to the bottom electrode. As expected, lattice expansion was observed for both the positive and negative pulses. When the electric field was turned on, the Bragg peak shifted to lower angles, indicating that the lattice had expanded along the direction of the electric field. The largest change in peak position occurred at the maximum voltages, positive 10 and negative

10 V. After the maximum voltages, the lattice constant returned to the initial state. No variation in the lattice constant was observed when zero voltage was applied.

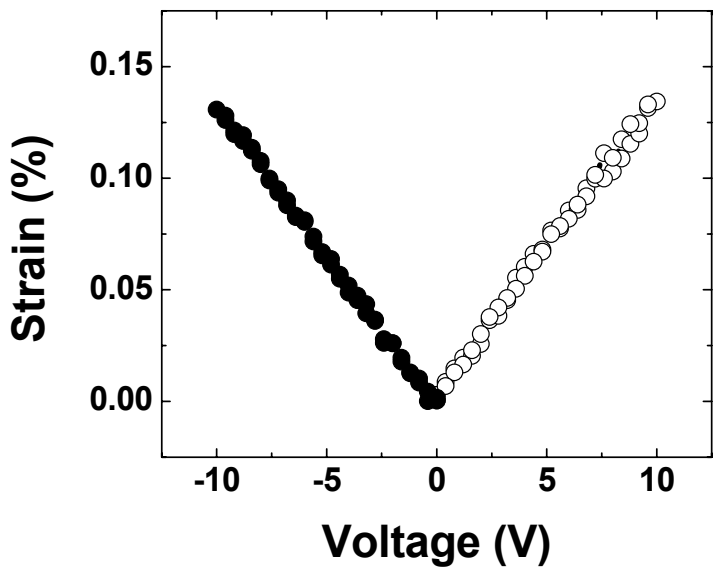

Figure 5.6 The strain as a function of the applied voltage in the PZT thin film capacitor under electric field pulses.

The strain was calculated from the change in the lattice constant as a function of the applied voltage (Fig. 5.6). The lattice constant was determined from the x-ray reflection angles. The strain was found to be proportional to the applied voltage. The maximum strain was 0.13% at both positive and negative 10 V. The longitudinal piezoelectric coefficients were 53 and 54 pm V^{-1} for the positive and negative unipolar pulses, respectively. The values of d_{33} in two opposite polarization states are thus nearly equal.

These results can be compared with what has been observed in previous experiments and with what has been predicted theoretically. Chen *et al*.[89] has calculated the longitudinal piezoelectric coefficients of (001)-oriented PZT thin films with varying compositions using a phenomenological thermodynamic approach. The values of d_{33} found using this approach were approximately 70 pm V^{-1} for $Pb(Zr_{0.5}Ti_{0.5})O_3$. The experimental results showed that the value of d_{33} was approximately 50 pm V^{-1} for $Pb(Zr_{0.49}Ti_{0.51})O_3$.[87] Although the compositions of PZT are slightly different to our PZT, the values of d_{33} are comparable to the d_{33}, 53 pm V^{-1}, we observed.

X-ray microdiffraction can also be used to measure the transverse piezoelectric coefficients, which lead to distortions in the plane perpendicular to the applied electric field, by observing the change in in-plane lattice parameter of the films.

5.3.3 Polarization switching and piezoelectricity

A bipolar electric field higher than the coercive field results in polarization switching. As described in Chapter 3, polarization switching process includes nucleation of opposite polarization domains and movement of the domain walls. Inhibition of the nucleation and domain wall movement leads to partial polarization switching and an anomalous piezoelectric response. In this section we describe our studies of the relationship between polarization switching and the piezoelectric response by analyzing structural information achieved from x-ray microdiffraction experiments.

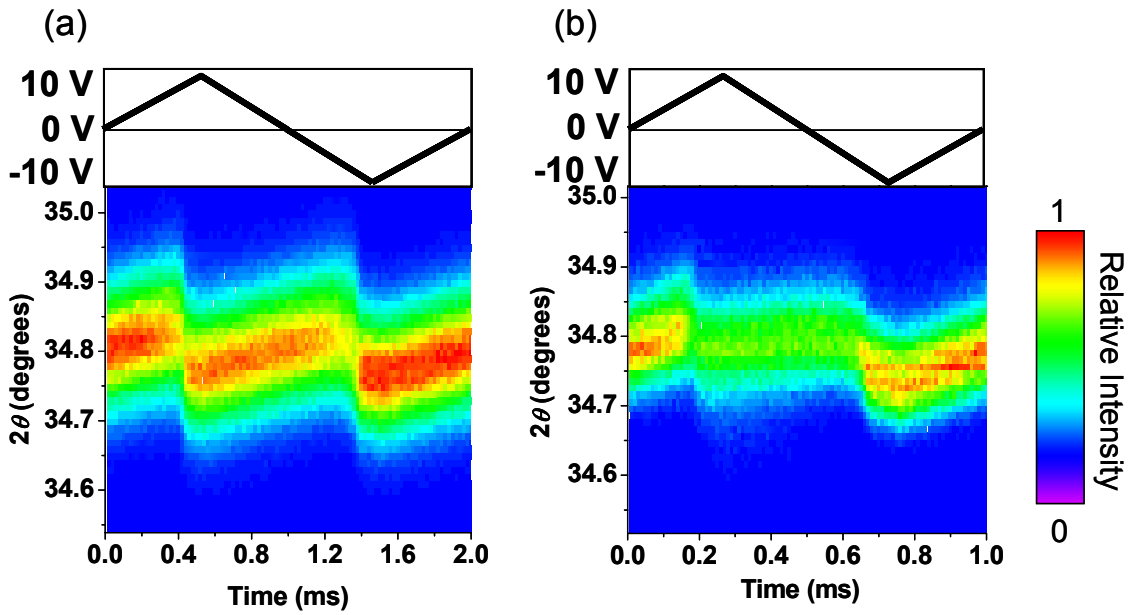

Figure 5.7 Plots of the intensity of the PZT (002) Bragg reflection as a function of θ-2θ and time during (a) 0.5 kHz and (b) 1 kHz bipolar electrical pulses. The amplitude and the shape of applied voltage pulses are shown above the intensity maps.

The 4000 Å thick PZT films were subjected to triangular ±10 V pulses. Figure 5.7 (a) and (b) show maps of the intensity of the PZT (002) Bragg reflection as a function of time under 0.5 and 1 kHz bipolar pulses. At the onset of the bipolar pulse, the direction of the polarization vector and the electric field are antiparallel. As the amplitude of the applied voltage pulse increases, the lattice constant shrinks. This causes a shift of the Bragg peak of PZT (002) reflection to a higher angle. At the positive coercive voltage, the spontaneous polarization switches to point along the electric field direction and reaches the opposite polarization state. During this time, a sudden lattice expansion occurs due to the reorientation of the spontaneous polarization. The maximum lattice expansion is observed

at positive 10 V. After the maximum voltage, the lattice constant contracts linearly to 0 V. The same phenomena including lattice contraction, polarization switching, lattice expansion, and then lattice contraction can be used to explain the following negative 10 V pulse.

Figure 5.8 (a) shows electromechanical hysteresis loop calculated from the x-ray reflections recorded during the 0.5 kHz bipolar voltage pulses. This hysteresis loop includes the piezoelectric lattice distortion and polarization switching. The hysteresis loop is almost symmetric with respect to V=0. The longitudinal piezoelectric coefficients in the linear regions were 42 and 45 pm V^{-1} for the positively and negatively poled states, respectively.

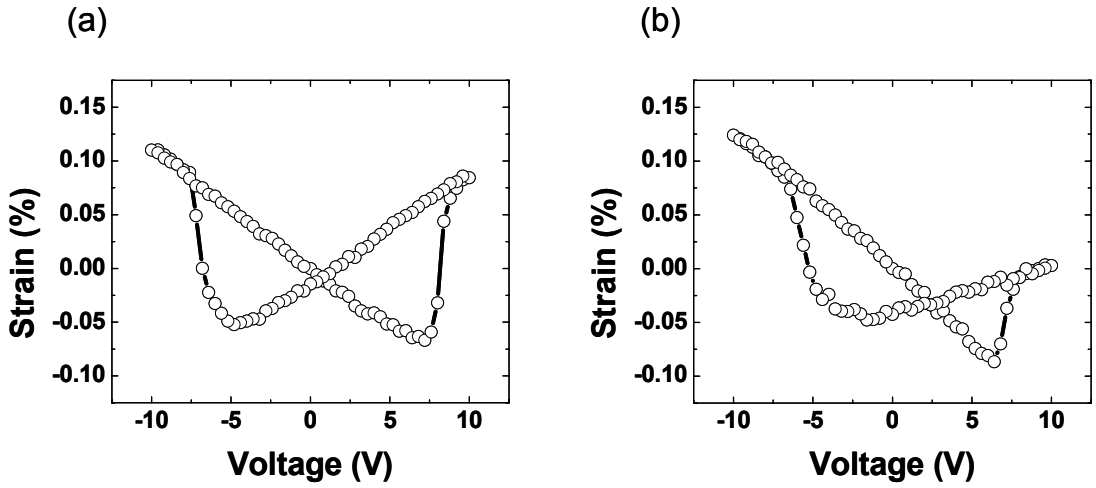

Figure 5.8 Electromechanical hysteresis loops for electric fields at frequencies of (a) 0.5 kHz and (b) 1 kHz.

With electrical pulses at a frequency of 1 kHz, however, the hysteresis loop is asymmetric with respect to V=0 (Fig. 5.8 (b)). The piezoelectric coefficients are remarkably different for two opposite polarization states, 17 and 53 pm V^{-1}.

In order to interpret the contribution of the polarization switching to the piezoelectric response we have developed a model illustrated in Fig. 5.9. We begin with the hypothesis that all polarization domains completely switch under the application of the 0.5 kHz electrical pulse. If domains are completely switched, except for voltages near the coercive field while the film is switching there is only a single domain in which polarization is parallel to the electric field (Fig. 5.9 (a)). This case, the same piezoelectric response in two polarization states is expected. As a result, the electromechanical hysteresis loop shown in Fig. 5.8 (a) can be observed. This model, however, cannot explain the hysteresis loop shown in Fig. 5.8 (b).

With the 1 kHz pulses, we hypothesize that there is partial polarization switching. There is thus a mixture of domains having opposite polarization directions. The d_{33} in this mixed state is lower than the d_{33} in the polarization state switched completely. This suggests that there are domains that do not switch under the positive voltage pulses. The electromechanical hysteresis loop shown in Fig. 5.8 (b) can be explained using this model based on the coexistence of switchable and nonswitchable domains (Fig. 5.9 (b)). In one polarization state, all domains have the same polarization direction parallel to the electric field, while in the opposite polarization state domains have different polarization directions due to nonswitchable domains. In the mixed state, the sign of piezoelectric coefficient in

each domain depends on the direction of polarization in each domain with respect to the electric field.

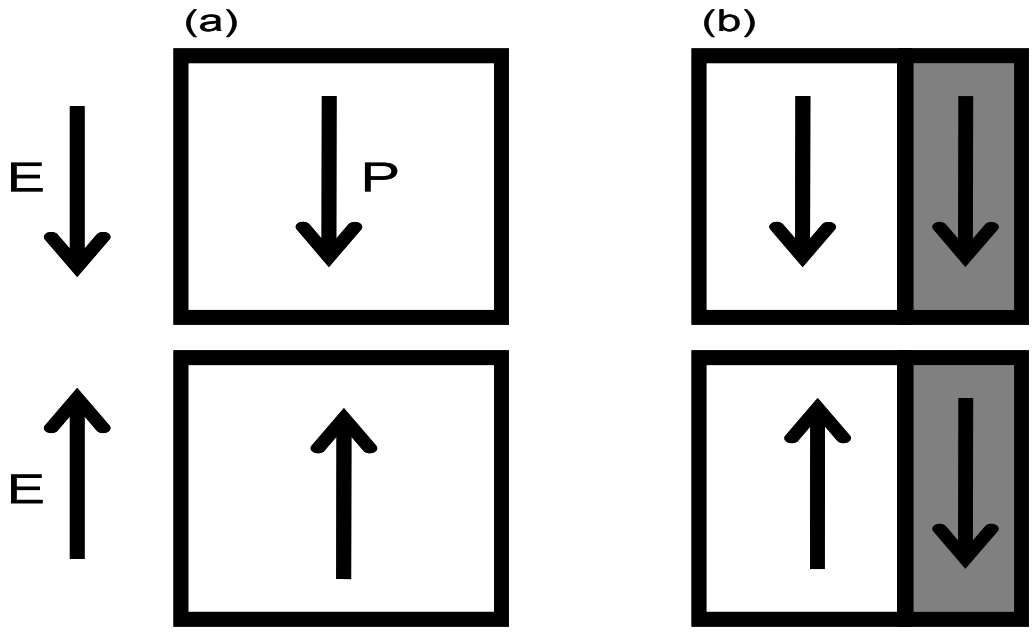

Figure 5.9 Schematic diagram of (a) complete polarization switching and (b) partial polarization switching. The white and grey regions indicate the switchable and nonswitchable domains, respectively. The arrow indicates the direction of electric field and polarization.

The average piezoelectric coefficient is reduced by the nonswitchable domains. Based on our hypothesis, the average piezoelectric coefficient (d^{ave}) can be calculated by using $d^{ave} = d \times (1-2x)$, where d is the piezoelectric coefficient at the polarization state with complete switching and x is the volume fraction of nonswitchable domains. Assuming that the d is 53 pm V^{-1} and d^{ave} is 17 pm V^{-1}, the volume fraction of nonswitchable domains is 34%. The formation of nonswitchable domains also leads to a reduction in the

remnant polarization in polarization-electric field hysteresis loops (Fig. 5.10). The remnant polarization was 90 μC cm^{-2} in fresh device. The electrical hysteresis loop measured after the piezoelectric response experiments showed the remnant polarization of 60 μC cm^{-2} which was 67% of the initial value.

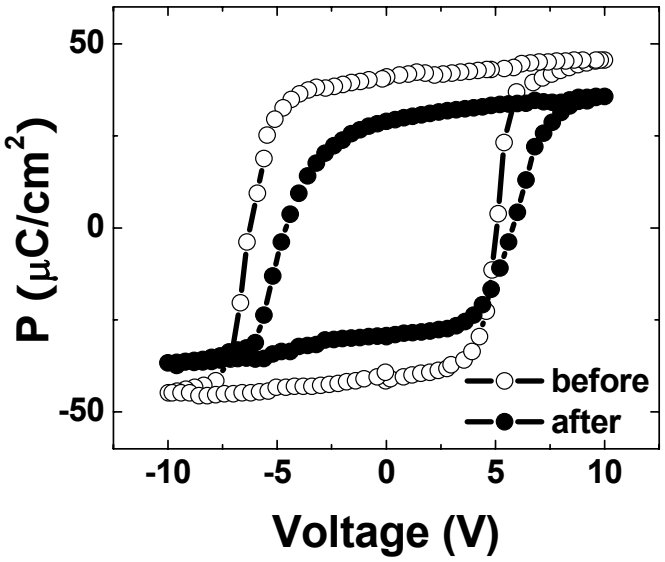

Figure 5.10 Polarization-electric field hysteresis loops measured before the piezoelectric experiments in fresh device and after the piezoelectric experiments.

The mixed state leads to broadening of the full width at half maximum (FWHM) of the x-ray reflection. The 2θ angle difference between the two Bragg reflections arising from the two domains under an applied voltage of the positive 10 V was 0.05°. Since the x-ray beam divergence was 0.068°, it was impossible to distinguish the Bragg reflections from the two states.

Figure 5.11 (a) shows the FWHM of the PZT (002) Bragg reflection as a function of time during the 0.5 kHz electric field pulses. The values of the FWHM and d_{33} are nearly the same in the two polarization states, which implies that polarization domain is completely switched under the electric field. The width is broader only during polarization switching near the coercive voltage.

The FWHM of the PZT (002) Bragg reflection measured with 1 kHz electric field pulses showed a different shape compared to the 0.5 kHz results (Fig. 5.11 (b)). The FWHM during polarization switching near the positive coercive voltage is broader than the negative coercive voltage. This is due to the incomplete polarization switching at the positive coercive voltage.

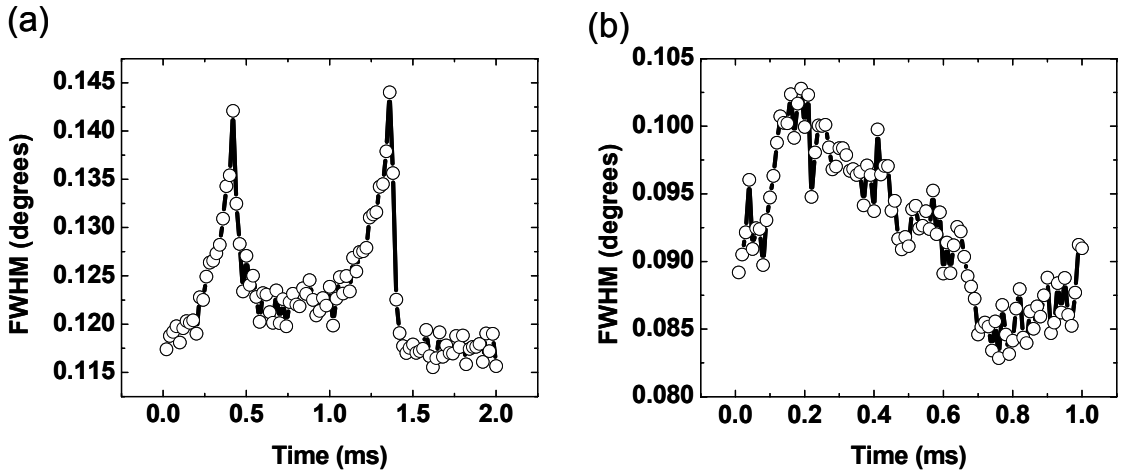

Figure 5.11 The full width at half maximum of the PZT (002) Bragg reflection as a function of time during (a) the 0.5 kHz and (b) the 1 kHz bipolar electrical pulses.

If the domain size had been bigger than our beam size, then the local piezoelectric coefficients would have been resolved in scans of the beam across the sample. In the experiments, however, the local values of d_{33} were the same across the entire device, implying that the size of the nonswitchable domains was smaller than that of the focused x-ray beam.

In this section, the measurement of piezoelectric response was based on the detecting structural changes. We interpreted the effect of partial polarization switching on total piezoelectric response by analyzing the shift and the width of the PZT (002) Bragg reflection. X-ray microdiffraction can provide us to study the contribution of domain wall motions and phase transitions to piezoelectric response.

5.3.4 Electric field dependence of the piezoelectric response

In the previous section, we discussed that applying an electric field near the coercive field leads to the partial polarization and the asymmetric piezoelectric response. Thus the piezoelectric response is closely linked to the magnitudes of an electric field. In order to understand the effect of different electric fields on piezoelectricity, we chose the electric fields near the coercive field and much higher than the coercive field. Applying an electric field higher than the coercive field would lead to polarization switching as well as the piezoelectric response. However, applying an electric field lower than the coercive field leads to no polarization switching and produces only the lattice distortion.

The piezoelectric response at four different electric fields was investigated with 4000 Å thick PZT thin film capacitors. The coercive voltages in the PZT thin film capacitor were approximately 7.2 and -5.5 V. Four electromechanical hysteresis loops measured with triangular ±6, ±7.5, ±10, and ±19 V electrical pulses of 1 kHz are shown in Fig. 5.12.

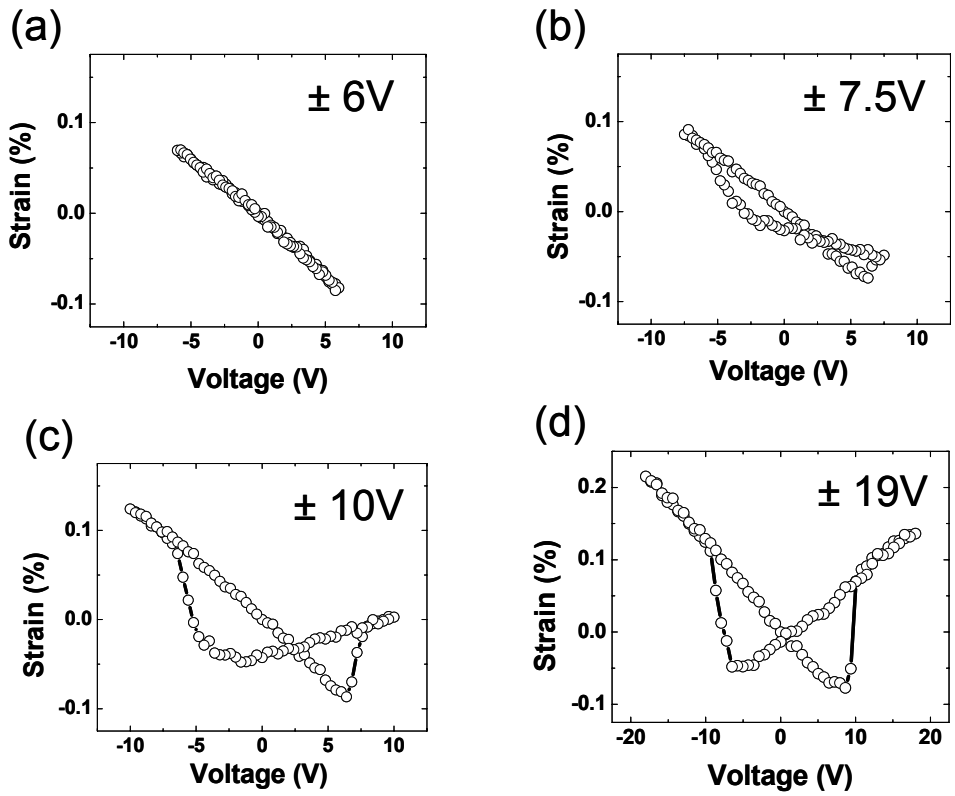

Figure 5.12 Electromechanical hysteresis loops for (a) ±6 V, (b) ±7.5 V, (c) ±10 V, and (d) ±19 V pulses.

Figure 5.12 (a) shows the piezoelectric response under an electric field of ±6 V, in which the positive voltage is lower than the positive coercive voltage. Under the ±6 V

electrical pulses, the application of positive 6 V did not lead to polarization switching. As expected, the polarization direction was parallel to the negative electric field direction, even at positive voltages. Applying positive voltages showed the lattice contraction without polarization switching. The expansion of the lattice occurred at negative electric fields since the polarization direction was parallel to the electric fields. There was no evidence of polarization switching in the electromechanical hysteresis loop. The strain was proportional to the applied voltage, as we previously observed for electric field pulses of a single sign in Fig. 5.6.

Partial polarization switching occurred under electric fields with magnitudes close to the coercive field. Figure 5.12 (b) shows the piezoelectric response to a voltage pulse of ±7.5 V, which is slightly higher than the coercive voltage. Even though there was some degree of polarization switching at positive voltages in this case, the electromechanical hysteresis loop was asymmetric and the values of d_{33} were different in the two polarization states. The piezoelectric coefficients were -17 and 48 pm V^{-1} for positive and negative pulses, respectively. In this case, there were domains that did not switch from the negative state to the positive state. The volume fraction of the nonswitchable domains polarized to the negative state was 68%. Since the volume fraction of nonswitchable domains was more than switchable domains, the piezoelectric coefficient in the positive state had a negative sign. Applying ±10 V pulses still induced partial polarization switching (Fig. 5.12 (c)). The volume fraction of nonswitchable domains was 34% which is much smaller than the fraction of ±7.5 V pulses. The reduced fraction of nonswitchable domains produced larger value of d_{33} in positive state than that of ±7.5 V pulses.

Almost complete polarization switching occurred when an electric field much higher than the coercive field was applied. As shown in Fig. 5.12 (d), applying ±19 V pulses produced a more symmetric loop. With these large pulses, values of d_{33} were 35 and 48 pm V^{-1} for the positive and negative states, respectively. The volume fraction of nonswitchable domains was only 10%.

It has been reported that illuminating ferroelectric capacitors with UV light or x-rays leads to a suppression of switchable polarization even in ferroelectric devices that are ordinarily free from fatigue.[29,90] A significant suppression of switchable polarization in PZT films with $(La,Sr)CoO_3$ electrodes was observed when an electric field near the coercive voltage was applied under UV illumination.[91] Under illumination, after 10^6 switching cycles, the switchable polarization was reduced by 60% of its initial value. Applying a high electric field after 10^8 cycles, however, showed only small amount of degradation, 20%. The reduced switchable polarization can be explained by pinning of domain walls by defects such as oxygen vacancies. In our case, degradation in the switchable polarization and a reduction in the piezoelectric coefficient under switching pulses may be due to x-ray radiation. These effects can be overcome either by applying an electric field much higher than the coercive electric field or by applying lower frequency voltage pulses.

5.3.5 Variation of the piezoelectric response with position

When a ferroelectric thin film capacitor is grown on a thick substrate, the lateral dimensions of the film are constrained by the substrate. The out-of-plane dimensions of the portion of the film near the edge of the capacitor are also constrained by the ferroelectric materials surrounding the capacitor. In this section, we investigate the effect of the edges of the capacitor on the piezoelectric response by observing the strain in the device under electric fields.

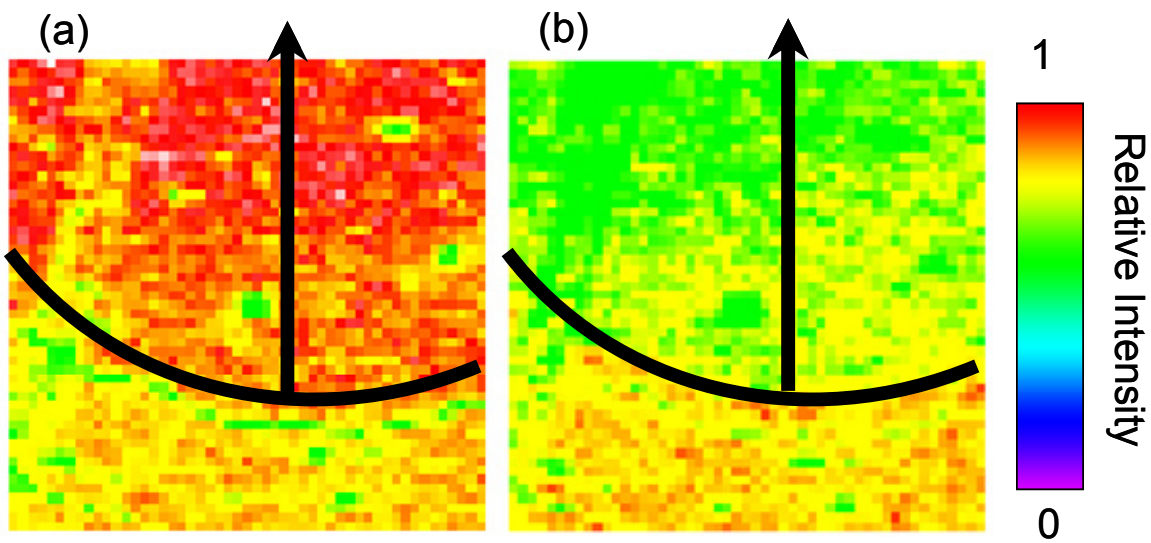

Figure 5.13 Area maps of intensity of the PZT (002) reflections in two polarization states: after applying for (a) negative and (b) positive pulses. The arrow indicates the scanning direction of the measurements of the local piezoelectric response. The arcs in the images indicate the edge of the device. The area of each image is 50×50 μm^2.

The piezoelectricity of the 4000 Å thick PZT thin film was investigated at different positions on the capacitor. Figure 5.13 shows x-ray intensity images of a part of the device.

The two images were normalized with respect to each other using the intensity in the region of the image outside the top electrode. The color scale in the images corresponds to the intensity of the PZT (002) reflections. The intensity at the negative state was higher than that at the positive state. The intensity difference in two polarization states was 25% at the center of the capacitor and 15% near the edge.

The local piezoelectric response at different positions on the device was measured by moving the sample so that the electromechanical measurements are obtained for the positions along the path shown by the arrow in Fig. 5.13. The strain was measured with triangular positive and negative 10 V pulses. The piezoelectricity measured at the center and the edge of the device is shown in Fig. 5.14 (a). At the center of the capacitor, the strain at positive 10 V was 0.13% which corresponds to d_{33}=53 pm V^{-1}. Near the edge of the capacitor, the strain was reduced to 0.065% and 0.083% for positive and negative states, respectively. Those values are half of the strain at the center. No lattice distortion was observed outside the device. Figure 5.14 (b) shows the values of d_{33} obtained as a function of position during this scan. At each position, the strains for the positive and negative states were the same.

The zero position in Fig. 5.14 was determined at the boundary in which the intensity did not change at two polarization states. The device position was then determined by comparing the position in the images to the position of mechanical translation stages. We observed that there was a shift of the edge of the device between the two successive. The shift was approximately 1 μm in each of the vertical and horizontal directions. This

distance is not sufficiently large to make a difference in placing the positions of the center and edge of the device on the scans in Fig. 5. 14. The reduced piezoelectric response at the edge of the device could be because the top electrodes created by the shadow mask process are thinner near the edge and the electric field is reduced.

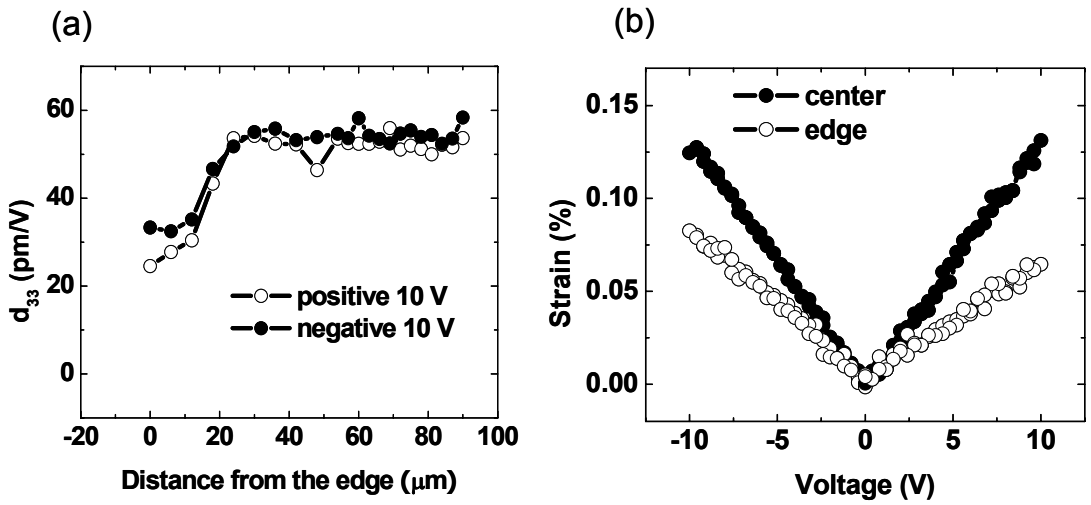

Figure 5.14 (a) Piezoelectric coefficients measured as a function of position using unipolar voltage pulses and (b) strain as a function of applied voltage at the center and the edge of the capacitor.

We changed the mechanical and electrical boundary conditions at the edge by removing a portion of the edge of the sample using focused ion beam (FIB) milling. Using FIB, PZT with two SRO electrodes were etched so that the PZT near the edge can deform freely. The schematic diagram of the structure of the etched device is shown in Fig. 5.15 (a).

The piezoelectric response was measured using triangular positive and negative 18 V pulses. Unlike the shadow masked edge described above, the piezoelectricity measured near the machined edge showed no reduced piezoelectric coefficient (Fig. 5.15 (b)). The piezoelectric coefficient was 45 pm V^{-1} and was abruptly dropped to 0 pm V^{-1} at the edge.

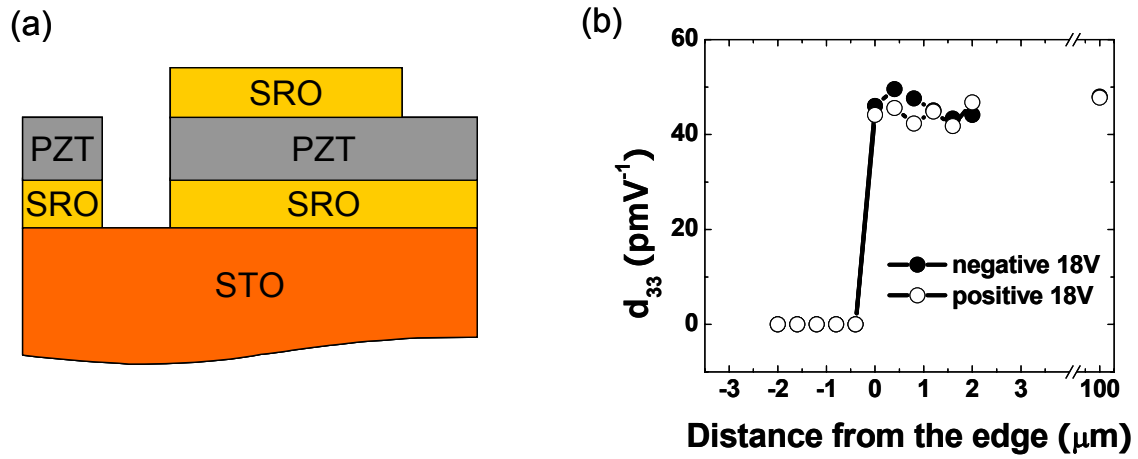

Figure 5.15 (a) Schematic diagram of the machined device and (b) piezoelectric coefficients measured as a function of position.

The investigation of the position-dependent piezoelectric response showed that the piezoelectric response was different between the center and edge of the capacitor. We observed reduced piezoelectric coefficients in the region between the edge of the device and 20 μm away from it towards the center of the device. By removing PZT around the edge, however, we did not observe the reduced piezoelectric coefficients.

In order to interpret the edge effect, the mechanical boundary effect was computed using ANSYS finite element analysis and compared to our experimental data. In the

modeling, we considered that a ferroelectric capacitor was constrained by a rigid substrate. We used Young's modulus of 118 GPa and Poisson's ratio of 0.2 for the ferroelectric material which corresponds to mechanical constants of $Pb(Zr_{0.5}Ti_{0.5})O_3$.[84] The results showed that there was a mechanical boundary effect near the edge of the device (Fig. 5.16). The reduced strain, however, was observed in the region of 500 nm away from the edge towards the center. The results do not agree with our observations. The reduced piezoelectric coefficients in the experiments might be due to the reduced electric field in the region, leading reduced strain in this region.

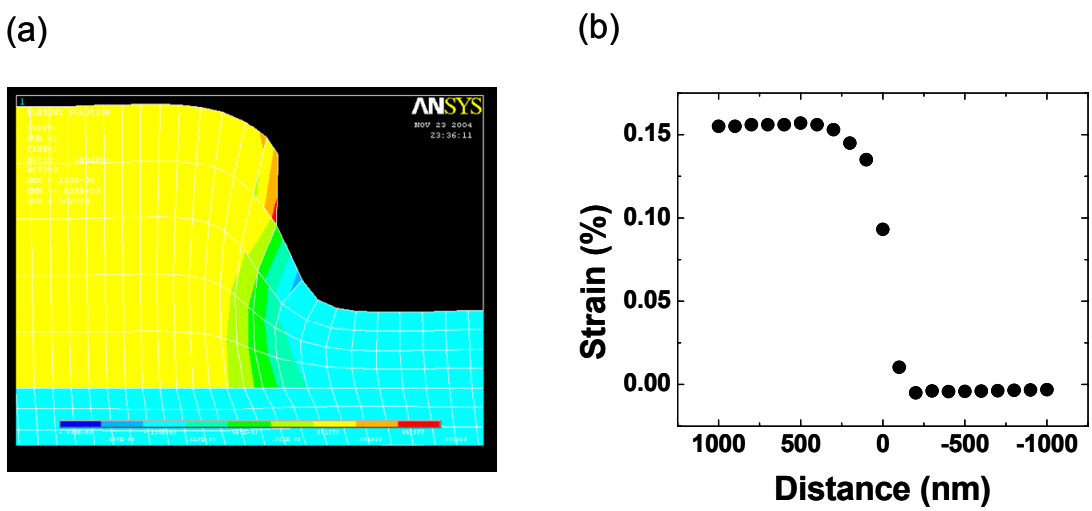

Figure 5.16 (a) The result of finite element analysis of the mechanical boundary effect and (b) strain calculated from the finite element method as a function of position.

5.3.6 Transverse piezoelectric coefficient in clamped PZT thin films

In order to study the clamping effect induced by the substrate, we investigated the transverse piezoelectric response in PZT thin film capacitors. If the PZT film is fully

constrained by the STO substrate, the in-plane strain induced by an electric field along the thickness direction is to be zero. Thus, there is no change in a lateral size of the film when an electric field is applied.

Unipolar triangular positive and negative 10 V pulses with 20 ms duration were applied to 3000 Å thick PZT film capacitors. Before the measurements, the capacitor was poled in the direction of an electric field so that lattice expansion occurs under the electric field. In order to measure both the out-of-plane and in-plane lattice constants of the PZT thin films, we made measurements of the distribution of intensity in reciprocal space near the PZT (103) reflection. From the peak positions in the reciprocal space maps, the out-of-plane and in-plane lattice parameters can be estimated independently. Details were described in Section 5.3.1.

Figure 5.17 shows the strain as a function of applied voltage. The maximum strain of the out of plane was 0.13% at both negative and positive voltages. The in-plane strain was -0.067%, which is approximately half of the out of plane strain. From the slope of the strain curve, the d_{33} was calculated and to be 38 pm V^{-1}. The d_{31} was calculated from the curve and to be -17 and -5 pm V^{-1} for negative and positive pulses, respectively. The sign of d_{31} is opposite to that of d_{33} due to the Poisson's ratio.

In order to verify the transverse piezoelectric response, we investigated the response using bipolar pulses. If the observed transverse piezoelectric coefficients are the real values,

then we expect that an electromechanical hysteresis loop including polarization switching can be obtained.

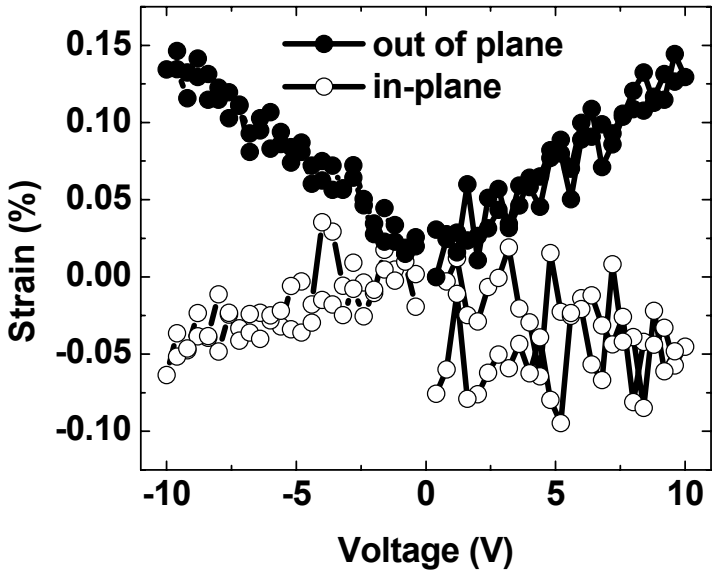

Figure 5.17 In-plane and out-of-plane strain as a function of an applied voltage.

The electromechanical hysteresis loops are plotted in Fig. 5.18. The applied electrical pulses were triangular ± 10 V pulses of a frequency of 50 Hz. The polarization switching was confirmed in the two hysteresis loops. The coercive voltages in the two loops were identical. The positive and negative coercive voltages were 5 and -3.7 V, respectively.

The values of longitudinal and transverse piezoelectric coefficients were calculated from the loops shown in Fig. 5.18. The longitudinal piezoelectric coefficients were 37 and

45 pm V^{-1} for positive and negative states, respectively. The transverse piezoelectric coefficients in two polarities were approximately the same, -15 pm V^{-1}.

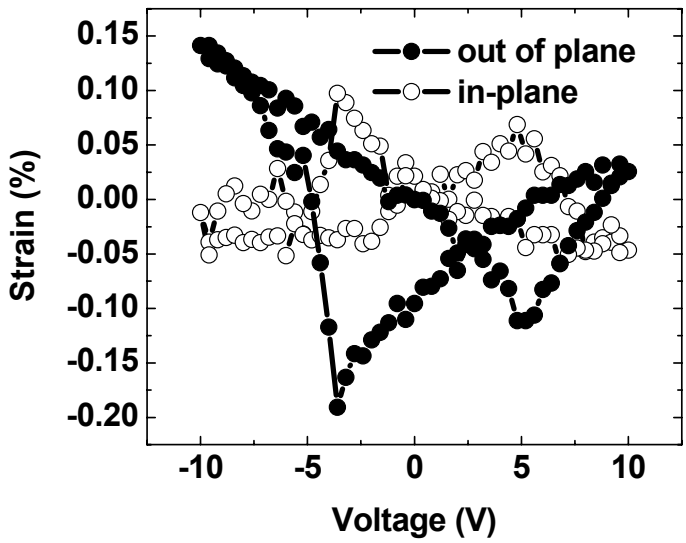

Figure 5.18 In-plane and out-of-plane electromechanical hysteresis loops under bipolar pulses.

Our results indicate that the in-plane strain is not zero although the 3000 Å thick PZT films used for the experiment were epitaxially grown on the thick single crystal STO substrate. This suggests that either there is an elastic deformation or bending of the substrate, or that the PZT layer is not completely constrained by the substrate. If an elastic deformation or bending of the substrate is the origin of the in-plane strain, then this effect can be observed by measuring strain in the bottom electrode or the substrate. However, we could not observe any distortion in the SRO bottom electrode under the application of an electric field (Fig. 5.19). Another possible origin of the non-zero d_{31} may be considered

that there is no clamping effect in our device since our PZT films were almost fully relaxed in as grown state.

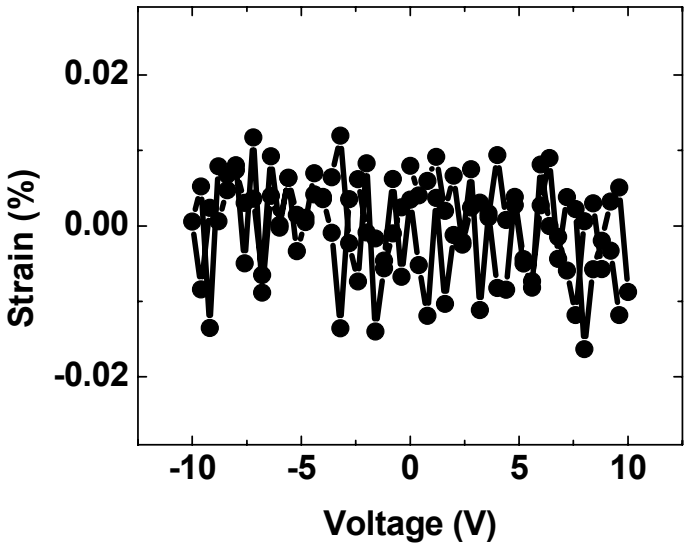

Figure 5.19 Strain in SRO bottom electrode under the application of the electrical pulses. No lattice deformation was observed in the SRO layer.

X-ray microdiffraction can be used to study piezoelectricity in piezoelectric thin films. Using films with thinner and smaller in lateral size, it will be possible to understand complete clamping effect in the films grown on a thick substrate.

5.4 Conclusion

We have investigated the piezoelectricity of PZT thin film capacitors using time-resolved x-ray microdiffraction. The longitudinal piezoelectric coefficient was 53 pm V^{-1}

in the $Pb(Zr_{0.45}Ti_{0.55})O_3$ thin film. The contribution of polarization switching to the piezoelectric response was clarified using structural information achieved by x-ray reflections. The asymmetric electromechanical hysteresis loop was explained a model based on the coexistence of switchable and nonswitchable domains.

The clamping effect in the PZT thin film capacitors was investigated. Piezoelectric coefficient near the capacitor edge was smaller than that at the center. This is due to the PZT surrounding the capacitor. The clamping effect induced by the substrate was studied by observing x-ray reflections that included a component of the scattering wave vector in the plane of the films. The transverse piezoelectric coefficient was not zero. The results suggested that there is no clamping effect in the 3000 Å thick PZT film.

Chapter 6 Conclusions

In this thesis we have studied polarization fatigue by observing the evolution of polarization domains and piezoelectric response by measuring the strain in ferroelectric PZT thin films subjected to an electric field. Since synchrotron x-ray microdiffraction is sensitive to structural changes related to polarization switching and lattice distortion, it allowed us to better understand ferroelectricity and piezoelectricity in ferroelectric thin film capacitors.

First, polarization switching and polarization fatigue in the PZT thin film capacitors with the Pt or the SRO electrode were investigated. The polarization switching and the origin of polarization fatigue were studied in terms of structural understanding. Our results showed that the initial stage of fatigue is related to the formation of nonswitchable domains, which consequently leads to reduction of switchable polarization. At high electric field, the fatigue results in the formation of structurally changed domains. The fatigue is irreversible at high electric field. At low electric field, the fatigue process is reversible and the switchable polarization was restored by applying a higher electric field. On the other hand, the PZT thin film capacitors with the SRO electrodes showed no fatigue effect up to 10^7 switching cycles which supports the role of oxygen vacancies in polarization fatigue.

Second, the piezoelectric response in the PZT thin film capacitors was investigated. The advantage of using the x-ray microdiffraction technique is that we could measure a piezoelectric response in the PZT film layer instead of measuring a total thickness change

through the capacitor structure. This allowed us to measure the piezoelectric coefficients precisely and to probe the clamping effect in ferroelectric thin film capacitors. Our results showed that the value of the longitudinal piezoelectric coefficient in $Pb(Zr_{0.45}Ti_{0.55})O_3$ thin film capacitors was 53 pm V^{-1}. The longitudinal piezoelectric coefficients measured under switching pulses were different between the two opposite polarization states. The difference in piezoelectric response can be explained with a model based on the coexistence of switchable and nonswitchable domains. The position dependence of the piezoelectric response was investigated and showed that the piezoelectric response near the capacitor edge was different than at the center. Finally, we found that the transverse piezoelectric coefficient was 17 pm V^{-1}. This result could not be explained by the clamping effect since the transverse piezoelectric coefficient would be 0 pm V^{-1} if the film were constrained by the substrate. The origin of the reduced strain near the edge and the transverse piezoelectric coefficient are currently unclear and need to be investigated further.

A small, highly intense focused x-ray beam makes it possible to study polarization switching and piezoelectricity in nanostructures as thin as a few unit cells and of arbitrarily small lateral dimensions. The advantage of spatial and time resolutions in synchrotron x-ray will in the future provide structural information for a range of materials at nanometer sizes and picosecond time scales.

REFERENCES

[1] R. E. Newnham, Rep. Prog. Phys. **52**, 123 **(**1989).

[2] J. F. Scott and C. A. Paz de Arajuo, Science **246**, 1400 (1989).

[3] D. L. Polla and L. F. Francis, Annu. Rev. Mater. Sci. **28**, 563 (1998).

[4] D. C. Lupascu, *Fatigue in Ferroelectric Ceramics and Related Issues*, (Springer, New York, 2003).

[5] A. K. Tagantsev, I. Stolichnov, E. L. Colla, and N. Setter, J. Appl. Phys. **90**, 1387 (2001).

[6] L. Chen, J.-H. Li, J. Slutsker, J. Ouyang, and A. L. Roytburd, J. Mater. Res. **19**, 2853 (2004).

[7] R. W. James, *The Optical Principles of the Diffraction of X-rays*, (Cornell University Press, New York, 1965).

[8] K. Matsuura, Y. Cho, and R. Ramesh, Appl. Phys. Lett. **83**, 2650 (2003).

[9] Y. Xu, *Ferroelectric Materials and Their Applications*, (North-Holland, New York, 1991).

[10] G. A. Rossetti, Jr., W. Zhang, and A. G. Khachaturyan, Appl. Phys. Lett. **88**, 072912 (2006).

[11] H. D. Chen, K. R. Udayakumar, C. J. Gaskey, and L. E. Cross, Appl. Phys. Lett. **67**, 3411 (1995).

[12] S. Zhang, X. Dong, and S. Kojima, Jpn. J. Appl. Phys. **36**, 2994 (1997).

[13] D. Sheen and J. Kim, Phys. Rev. B **67**, 144102 (2003).

[14] M. Dawber, K. M. Rabe, and J. F. Scott, Rev. Mod. Phys. **77**, 1083 (2005).

[15] M. Daglish and T. Kemmitt, IPENZ. Transaction **27**, 21 (2000).

[16] W. L. Warren, D. Dimos, G. E. Pike, B. A. Tuttle, M. V. Raymond, R. Ramesh, and J. T. Evans, Jr., Appl. Phys. Lett. **67**, 866 (1995).

[17] B. S. Kang, J.-G. Yoon, D. J. Kim, T. W. Noh, T. K. Song, Y. K. Lee, J. K. Lee, and Y. S. Park, Appl. Phys. Lett. **82**, 2124 (2003).

[18] B. Jaffe, W. R. Cook, and H. Jaffe, *Piezoelectric Ceramics*, (Academic Press, London and New York, 1971).

[19] S. Fushimi and T. Ikeda, J. Am. Ceram. Soc. **50**, 129 (1967).

[20] Cz. Pawlaczyk, A. K. Tagantsev, K. Brooks, I. M. Reaney, R. Klissurska, and N. Setter, Integrated Ferroelectrics **8**, 293 (1995).

[21] H. N. Al-Shareef, B. A. Tuttle, W. L. Warren, T. J. Headley, D. Dimos, J. A. Voigt, and R. D. Nasby, J. Appl. Phys. **79**, 1013 (1996).

[22] P. J. Schorn, D. Bräuhaus, U. Böttger, R. Waser, G. Beitel, N. Nagel, and R. Bruchhaus, J. Appl. Phys. **99**, 114104 (2006).

[23] D. J. Johnson, D. T. Amm, E. Griswold, K. Sreenivas, G. Yi, and M. Sayer, Mater. Res. Soc. Symp. Proc. **200**, 289 (1990).

[24] A. K. Tagantsev, M. Landivar, E. Colla, and N. Setter, J. Appl. Phys. **78**, 2623 (1995).

[25] E. L. Colla, A. K. Tagantsev, D. V. Taylor, and N. Setter, Appl. Phys. Lett. **72**, 2478 (1998).

[26] W. Li, A. Chen, X. Lu, J. Zhu, and Y. Wang, Appl. Phys. Lett. **86**, 192908 (2005).

[27] W. L. Warren, D. Dimos, B. A. Tuttle, G. E. Pike, R. W. Schwartz, P. J. Clew, and D. C. McIntyre, J. Appl. Phys. **77**, 6695 (1995).

[28] E. L. Colla, S. Hong, D. V. Taylor, A. K. Tagantsev, N. Setter, and K. No, Appl. Phys. Lett. **72**, 2763 (1998).

[29] W. L. Warren, D. Dimos, B. A. Tuttle, R. D. Nasby, and G. E. Pike, Appl. Phys. Lett. **65**, 1018 (1994).

[30] J. F. Scott, C. A. Araujo, B. M. Melnick, L. D. McMillan, and R. Zuleeg, J. Appl. Phys. **70**, 382 (1991).

[31] I. K. Yoo and S. B. Desu, Phys. Status Solidi A **133**, 565 (1992).

[32] X. Du and I.-W Chen, J. Appl. Phys. **83**, 7789 (1998).

[33] G. Le. Rhun, G. Poullain, and R. Bouregba, J. Appl. Phys. **96**, 3876 (2004).

[34] A. E. Paladino, J. Am. Ceram. Soc. **48**, 476 (1965).

[35] L. F. Schloss, H. Kim, and P. C. McIntyre, J. Mater. Res. **19**, 1265 (2004).

[36] H. N. Al-Shareef, K. R. Bellur, A. I. Kingon, and O. Auciello, Appl. Phys. Lett. **66**, 239 (1995).

[37] T. Nakamura, Y. Nakao, A. Kamisawa, and H. Takasu, Jpn. J. Appl. Phys. **33**, 5207 (1994).

[38] C. B. Eom, R. B. Van Dover, J. M. Phillips, D. J. Werder, J. H. Marshall, C. H. Chen, R. J. Cava, and R. M. Fleming, and D. K. Fork, Appl. Phys. Lett. **63**, 2570 (1993).

[39] R. Ramesh, W. K. Chan, B. Wilkens, H. Gilchrist, T. Sands, J. M. Tarascon, D. K. Fork, J. Lee, and A. Safari, Appl. Phys. Lett. **61**, 1537 (1992).

[40] K. Lefki and G. J. M. Dormans, J. Appl. Phys. **76**, 1764 (1994).

[41] A. L. Kholkin, E. L. Colla, A. K. Tagantev, D. V. Taylor, and N. Setter, Appl. Phys. Lett. **68**, 2577 (1996).

[42] M. Alexe, C. Harnagea, D. Hesse, and U Gösele, **79**, 242 (2001).

[43] D. Damjanovic, Rep. Prog. Phys. **61**, 1267 (1998).

[44] J.-M. Liu, B. Pan, H. L. W. Chan, S. N. Zhu, Y. Y. Zhu, and Z. G. Liu, Mater. Chem. Phys. **75**, 12 (2002).

[45] D. L. Allensworth, Rev. Sci. Instrum. **51**, 1330 (1980).

[46] P. Gerber, A. Roelofs, O. Lohse, C. Kügeler, S. Tiedke, U. Böttger, and R. Waser, Rev. Sci. Instrum. **74**, 2613 (2003).

[47] G. Zavala, J. H. Fendler, and S. Trolier-McKinstry, J. Appl. Phys. **81**, 7480 (1997).

[48] V. Nagarajan, A. Stanishevsky, L. Chen, T. Zhao, B.-T. Liu, J. Melngailis, A. L. Roytburt, R. Ramesh, J. Finder, Z. Yu, R. Droopad, and K. Eisenbeiser, Appl. Phys. Lett. **81**, 4215 (2002).

[49] S. Hong, H. Shin, J. Woo, and K. No, Appl. Phys. Lett. **80**, 1453 (2002).

[50] S. Annaka, J. Appl. Cryst. **10**, 354 (1977).

[51] E. Zolotoyabko, J. P. Quintana, B. H. Hoerman, and B. W. Wessels, Appl. Phys. Lett. **80**, 3159 (2002).

[52] A. Grigoriev, D. Do, D. M. Kim, C.-B. Eom, P. G. Evans, B. Adams, and E. M. Dufresne, Appl. Phys. Lett. **89**, 021109 (2006).

[53] F. Xu, S. Trolier-McKinstry, W. Ren, B. Xu, Z.-L. Xie, and K. J. Hemker, J. Appl. Phys. **89**, 1336 (2001).

[54] Z. Ma, F. Zavaliche, L. Chen, J. Ouyang, J. Melngailis, A. L. Roytburd, V. Vaithyanathan, D. G. Schlom, T. Zhao, and R. Ramesh, Appl. Phys. Lett. **87**, 072907 (2005).

[55] S.-E. Park and T. R. Shrout, J. Appl. Phys. **82**, 1804 (1997).

[56] T. Tsurumi, Y. Kumano, N. Ohashi, T. Takenaka, and O. Fukunaga, Jpn. J. Appl. Phys. **36**, 5970 (1997).

[57] N. A. Pertsev and A. Y. Emelyanov, Appl. Phys. Lett. **71**, 3646 (1997).

[58] V. Nagarajan, A. Roytburd, A. Stanishevsky, S. Prasertchoung, T. Zhao, L. Chen, J. Melngailis, O. Auciello, and R. Ramesh, Nature Mater. **2**, 43 (2003).

[59] F. Xu, F. Chu, and S. Trolier-McKinstry, J. Appl. Phys. **86**, 588 (1999).

[60] D. K. Bowen and B. K. Tanner, *High Resolution X-ray Diffractometry and Topography*, (Taylor & Francis, London, 2001).

[61] J. Als-Nielsen and D. McMorrow, *Elements of Modern X-ray Physics*, (John Wiley & Sons Ltd, New York, 2001).

[62] D. Attwood, *Soft x-rays and extreme ultraviolet radiation: Principles and applications*, (Cambridge University Press, 1999).

[63] A. Thompson *et al*., *X-ray Data Booklet*, (Lawrence Berkeley National Laboratory, 2001).

[64] www.esrf.fr/computing/scientific/xop

[65] A. Q. R. Baron, S. Kishimoto, J. Morse, and J.-M. Rigal, J. Synchrotron Rad. **13**, 131 (2006).

[66] S. Kishimoto, Rev. Sci. Instrum. **66**, 2314 (2316).

[67] http://xradia.com/Products/zoneplates.html

[68] E. Fatuzzo, Phys. Rev. **127**, 1999 (1962).

[69] S. C. Lee, G. Teowee, R. D. Schrimpf, D. P. Birnie, D. R. Uhlmann, and K. F. Galloway, Integrated Ferroelectrics **4**, 31 (1994).

[70] E. Soergel, Appl. Phys. B **81**, 729 (2005).

[71] S. Prasertchoung, V. Nagarajan, Z. Ma, R. Ramesh, J. S. Cross, and M. Tsukada, Appl. Phys. Lett. **84**, 3130 (2004).

[72] A. Gruverman, O. Auciello, and H. Tokumoto, Annu. Rev. Mater. Sci. **28**, 101 (1998).

[73] K. Lee and S. Baik, Annu. Rev. Mater. Res. **36**, 81 (2006).

[74] D. D. Fong and C. Thompson, Annu. Rev. Mater. Res. **36**, 431 (2006).

[75] V. V Antipov, A. A. Blistanov, E. D. Roshchupkina, R. Tucoulou, L. Ortega, and D. V. Roshchupkin, Appl. Phys. Lett. **85**, 5325 (2004).

[76] D. Do, P. G. Evans, E. D. Isaacs, D. M. Kim, C.-B. Eom, and E. M. Dufresne, Nature Mater. **3**, 365 (2004).

[77] B. Noheda, J. A. Gonzalo, L. E. Cross, R. Gue, S.-E. Park, D. E. Cox, and G. Shirane, Phys. Rev. B **61**, 8687 (2000).

[78] A. Grigoriev, D. Do, D. M. kim, C.-B. Eom, B. Adams, E. M. Dufresne, and P. G. Evans, Phys. Rev. Lett. **96**, 187601 (2006).

[79] S.-T. Zhang, B. Yang, Y.-F. Chen, Z.-G. Liu, X.-B. Yin, Y Wang, M. Wang, and N.-B. Ming, J. Appl. Phys. **91**, 3160 (2002).

[80] G. L. Yuan, J.-M. Liu, Y. P. Wang, D. Wu, S. T. Zhang, Q. Y. Shao, and Z. G. Liu, Appl. Phys. Lett. **84**, 3352 (2004).

[81] M. Ozgul, S. Trolier-McKinstry, and C. A. Randall, J. Appl. Phys. **95**, 4296 (2004).

[82] H. Ishiwara, M. Okuyama, and Y. Arimoto, *Ferroelectric Random Access Memories,* (Springer, New York, 2004).

[83] K. Lee, Y. Kim, S. Baik, J. Kim, and I. Jung, Appl. Phys. Lett. **79**, 2444 (2001).

[84] J.-H. Li, L. Chen, V. Nagarajan, R. Ramesh, and A. L. Roytburd, Appl. Phys. Lett. **84**, 2626 (2004).

[85] A. Barzegar, D. Damjanovic, N. Ledermann, and P. Muralt, J. Appl. Phys. **93**, 4756 (2003).

[86] A. L. Kholkin, C. Wütchrich, D. V. Taylor, and N. Setter, Rev. Sci. Instrum. **67**, 1935 (1996).

[87] H. Maiwa, J. A. Christman, S.-H. Kim, D.-J. Kim, J.-P. Maria, B. Chen, S. K. Streiffer, and A. I. Kingon, Jpn. J. Appl. Phys. **38**, 5402 (1999).

[88] P. F. Fewster, *X-ray Scattering from Semiconductors*, (Imperial College Press, London, 2003).

[89] L. Chen, V. Nagarajan, R. Ramesh, and A. L. Roytburd, J. Appl. Phys. **94**, 5147 (2003).

[90] N. Menou, A.-M. Castagnos, Ch. Muller, D. Goguenheim, L. Goux, D. J. Wouters, J.-L. Hodeau, E. Dooryhee, and R. Barrett, J. Appl. Phys. **97**, 044106 (2005).

[91] D. Dimos, H. N. Al-Shareef, W. L. Warren, and B. A. Tuttle, J. Appl. Phys. **80**, 1682 (1996).